IOWA STATE UNIVERSITY
Digital Repository

Graduate Theses and Dissertations

Iowa State University Capstones, Theses and Dissertations

2018

Structural and bonding characteristics of Ga-containing polar intermetallics

Asa Toombs
Iowa State University

Follow this and additional works at: https://lib.dr.iastate.edu/etd

 Part of the Chemistry Commons

Recommended Citation
Toombs, Asa, "Structural and bonding characteristics of Ga-containing polar intermetallics" (2018). *Graduate Theses and Dissertations*. 17336.
https://lib.dr.iastate.edu/etd/17336

This Dissertation is brought to you for free and open access by the Iowa State University Capstones, Theses and Dissertations at Iowa State University Digital Repository. It has been accepted for inclusion in Graduate Theses and Dissertations by an authorized administrator of Iowa State University Digital Repository. For more information, please contact digirep@iastate.edu.

Structural and bonding characteristics of Ga-containing polar intermetallics

by

Asa C. Toombs

A dissertation submitted to the graduate faculty

in partial fulfillment of the requirements for the degree of

DOCTOR OF PHILOSOPHY

Major: Chemistry

Program of Study Committee:
Gordon J. Miller, Major Professor
Wenyu Huang
Javier Vela
Joseph Burnett
Kirill Kovnir

The student author, whose presentation of the scholarship herein was approved by the program of study committee, is solely responsible for the content of this dissertation. The Graduate College will ensure this dissertation is globally accessible and will not permit alterations after a degree is conferred.

Iowa State University

Ames, Iowa

2018

Copyright © Asa C. Toombs, 2018. All rights reserved.

DEDICATION

In loving memory of John “Tom” Toombs, Robert C. Murrow, and Patricia L. Murrow.

Those we love and lose are always connected by the heartstrings into infinity.

−Terri Guillemets

TABLE OF CONTENTS

Page

ACKNOWLEDGEMENTS vi

ABSTRACT ix

CHAPTER 1. INTRODUCTION 1

1.1 Polar Intermetallics 1
1.2 Laves Phases 3
1.3 Coloring Problem 5
1.4 Elements 7
1.5 Organization of Dissertation 9
1.6 References 10

CHAPTER 2. EXPERIMENTAL AND COMPUTATIONAL DETAILS 11

2.1 Synthesis 11
2.1.1 Starting Materials 11
2.1.2 Sample Containers 11
2.1.3 Tube Furnaces 12
2.1.4 Arc Melting 12
2.2 Characterization 13
2.2.1 Powder X-Ray Diffraction 13
2.2.2 Single Crystal X-Ray Diffraction 13
2.3 Electronic Structure Calculations 14
2.3.1 TB-LMTO-ASA 14
2.3.2 VASP 15
2.4 References 16

CHAPTER 3. RHOMBOHEDRAL DISTORTION OF THE CUBIC $MgCu_2$-TYPE STRUCTURE IN Ca_2Pt_3Ga AND Ca_2Pd_3Ga 18

3.1 Abstract 18
3.2 Introduction 18
3.3 Materials and Methods 20
3.3.1 Electronic Structure Calculations 20
3.3.2 Synthesis 21
3.3.3 Powder X-Ray Diffraction 22
3.3.4 Single Crystal X-Ray Diffraction 22

3.4 Results 23
3.4.1 Phase Analysis 23
3.4.2 Structure Determination 25
3.4.3 Coloring Models and Electronic Structure Calculations 26
3.5 Conclusions 36
3.6 Acknowledgments 37
3.7 Supporting Information 37
3.8 References 38

CHAPTER 4. AN ORTHORHOMBIC VARIANT OF Ca_2Pd_2Ga 41

4.1 Abstract 41
4.2 Introduction 41
4.3 Experimental 42
4.3.1 Synthesis 42
4.3.2 Powder X-Ray Diffraction 43
4.3.3 Single Crystal X-Ray Diffraction 43
4.3.4 Electronic Structure Calculations 44
4.4 Results 45
4.4.1 Phase Analysis 45
4.4.2 Structure Determination 46
4.4.3 Structure Comparison 47
4.4.4 Electronic Structure Calculations 50
4.5 Conclusions 53
4.6 Acknowledgements 54
4.7 Supporting Information 54
4.8 References 54

CHAPTER 5. $Gd(Co_{1-x}Ga_x)_2$: SYNTHESIS, CRYSTAL STRUCTURES, AND INVESTIGATION OF STRUCTURAL TRANSFORMATIONS AND MAGNETIC PROPERTIES 56

5.1 Abstract 56
5.2 Introduction 57
5.3 Experimental 58
5.3.1 Synthesis 58
5.3.2 X-Ray Analysis 59
5.3.3 Magnetometry 62
5.3.4 Electronic Structure Calculations 63
5.4 Results and Discussion 64
5.4.1 Structural Features and Transformation 64
5.4.2 Magnetic Properties 67
5.4.3 Electronic Structure Calculations 68

5.4.3.1 Electronic structure of $MgCu_2$-type $GdCo_2$ 69
5.4.3.2 Orthorhombic SrMgSi-type GdCoGa 73
5.4.3.3 Hexagonal AlB_2-type $GdGa_2$ 76
5.5 Conclusions 78
5.6 Acknowledgements 79
5.7 Supporting Information 79
5.8 References 79

CHAPTER 6. FROM LAVES TO ZINTL: BONDING ISSUES INFLUENCING THE STRUCTURAL VARIATION IN $GdCo_{2-x}Ga_x$ 83

6.1 Abstract 83
6.2 Introduction 83
6.3 Electronic Structure Calculations 85
6.4 Results 86
6.4.1 $GdCo_{1.67}Ga_{0.33}$ 88
6.4.2 $GdCo_{1.33}Ga_{0.67}$ 90
6.4.3 GdCoGa 92
6.4.4 $GdCo_{0.67}Ga_{1.33}$ 93
6.4.5 $GdCo_{0.33}Ga_{1.67}$ 97
6.5 Conclusions 100
6.6 Acknowledgments 101
6.7 References 101

CHAPTER 7. CONCLUSIONS 105

APPENDIX A. SUPPORTING INFORMATION FOR CHAPTER 3 109

APPENDIX B. SUPPORTING INFORMATION FOR CHAPTER 4 119

APPENDIX C. SUPPORTING INFORMATION FOR CHAPTER 5 122

ACKNOWLEDGMENTS

I would like to thank my adviser Gordie Miller, for taking the chance and welcoming a student with no previous research experience into your group and helping shape me into the critical thinking scientist I am today. I thank you for all the guidance and insights throughout my research career and for involving me in your unique style of teaching, it has given me a new perspective as I journey forward with my own teaching career.

I would like to thank Wenyu Huang for serving on my committee and for letting me join your research group during my first summer here at Iowa State University. It was a great transitional experience getting in the lab and having the opportunity to get an introduction to research before the full start of graduate school hit. Thanks also to Javier Vela who has been a part of my committee from the beginning. To Joseph Burnett, thank you for your assistance with both my research and teaching careers and giving me the opportunity to help others, as an orientation leader, transition into being a teaching assistant while at ISU. Kirill Kovnir, I know the last year has probably been quite the whirlwind in moving schools and labs, so I thank you for taking the time and serving on my committee. To Patricia Thiel and Aaron Sadow, I thank you for the feedback and advice you have given me throughout my graduate career.

I would like to thank the current and previous scientists and post-docs of the Miller group for their support and valuable lessons in teaching me synthetic procedures and computational chemistry. Thank you Saroj Samal, Srinivasa Thimmaiah, Yuemei Zhang and Qisheng Lin.

Thank you to Joyce Pham, there really are no words to adequately describe all that I have learned and gained from you during this wild ride called graduate school. You helped

me stay centered and focused while also showing me the joy that is present in life, even during the stressful times such as before prelims, publishing the first paper, and the final defense. Your creative mind continuously gave me a unique perspective on any problem I was working on and you are an invaluable resource for my many questions. Your sincere smile and nod of support during those first few, let's be honest, rather rough group meeting presentations gave me a tremendous amount of encouragement and helped me continue on even with all of the nerves.

Thank you to my fellow students in the Miller group Dr. Xie, Dr. Lutz-Kappelman, Dr. Pham, and Stephanie Eveland. Every one of you has taught me something along the way and it was a great experience being able to walk this road together, whether it be for a short time or for the long haul.

I want to thank all my friends both new and old in Ames for their continued support. You really made the transition to a new school much easier and we have many stories to tell from our time together. Thank you to Lynette Edsall for helping me navigate all the forms and requirements that must be completed for the degree. Also, thank you for always having a welcoming office and for all the discussions about Star Wars, sometimes they were just what was needed after a hard day.

To my family, I give my unending thanks for all the love, support, and encouragement you have shown me through this experience. To Austin: I thank you for the many calls about projects and tractors you were working on as well as your advice on any project I was working on, it was nice to get away from school stuff for a bit. Hopefully, we will be able to tractor again together sometime soon. To Audra and Avery: I thank you for the visits you made to Ames as well as the random updates to your lives, they really helped

me feel connected to family. To Grandma: thanks for always having a welcoming home to come visit, I really enjoyed our visits and hugs whenever I made it home. To the Schall clan here in Runnels, IA: thank you for welcoming me into your family as one of your own and for the delightful home cooked meals on Sunday. Finally, to Mom and Dad: I thank you for all the time and effort you put into raising and shaping me into the person I am today. Thank you for instilling in me the values and beliefs that I have and supporting me even when I wanted to go a bit further away from home. Thank you for all your guidance and assistance during this stressful time, as well as for the care packages you sent. Thank you for taking the time to drive up and visit me here in Ames. Special thanks for all the hour-long phone calls for advice and sometimes just to see how your week was going, they really made being far away from home easier.

ABSTRACT

High temperature solid-state synthesis and electronic structure calculations were used to characterize and analyze Ga containing polar intermetallic compounds, specifically systems with late transition metals (Co, Pt, Pd) and cations of alkaline-earth (Mg, Ca, Sr,) or rare-earth (Gd) metals. Total energy calculations, magnetic moment and structural optimizations were performed with the *Vienna Ab initio Simulation Package* (VASP) and density of states and crystal orbital Hamilton population curves as well as the integration of the COHP were calculated using the Stuttgart Tight-Binding Linear Muffin-Tin Orbital with the Atomic Sphere Approximation (TB-LMTO-ASA). These tools were used to provide insight into the structural and bonding characteristics of these Ga containing polar intermetallics.

Two new fully ordered ternary Laves phases Ca_2Pt_3Ga and Ca_2Pd_3Ga were discovered and analyzed to shed light on the driving force behind the structural distortion of the cubic $MgCu_2$-type $CaPt_2$ and $CaPd_2$ with the substitution of Ga. Nine symmetrically inequivalent coloring models, substituting one Ga on each tetrahedra of the cubic structure, were proposed and studied. Change in energy calculations for three theoretically proposed steps of this substitution show that it is energetically favorable to substitute Ga for Pd however, Ga for Pt is energetically unfavorable, demonstrating the effect of size differences and the differences in Mulliken electronegativities in these systems.

An orthorhombic variant of the previously reported monoclinic Ca_2Pd_2Ga was synthesized and characterized. Structure comparisons show similar coordination environments for the atoms involved however, there is a change in the direction, stacking, and uniformity of the Pd−Pd linear chains in the structures. All electronic structure calculations indicate that the monoclinic structure is energetically more stable.

Electronic structure calculations were performed on a series of $GdCo_{2-x}Ga_x$ compounds to shed light on any driving forces of the structural changes with increased Ga content. Results indicate that the structure changes when the previous structure reaches a threshold of Ga−Ga homoatomic interactions. These structure changes happen with increased Ga content to optimize the Co−Ga heteroatomic interactions within the structures. The series of structures adopted also resembles the series of GdX_2 binary (X = Co, Ni, Cu, Zn, Ga) compounds thus indicating that the valence electron count plays a significant role in the structure changes as well.

CHAPTER 1. INTRODUCTION

1.1 Polar Intermetallics

The periodic table contains more than 80 metallic elements and the combination of these elements, along with group III, IV, and V *p* elements, results in a very large number of intermetallic compounds.[1] Intermetallic compounds are those that contain two or more metallic or semi-metallic elements.[2] Intermetallic compounds can be divided into three very broad groups depending on the degree of charge transfer from the electropositive to electronegative components: (1) Hume-Rothery phases, (2) polar intermetallics, (3) Zintl phases. This is only a single way to classify intermetallic compounds and there are many other systems for example, another system is to classify compounds based on their coordination polyhedra and orientation.[3] Hume-Rothery compounds consist of elements with similar sizes and electronegativities which cause little charge transfer between the elements. Zintl phases consist of elements with very different electronegativities and usually one element that lies along the Zintl border, which is between groups 13 and 14.[4] Polar intermetallic compounds simultaneously possess ionic and covalent interactions as in Zintl phases however, common valence electron counting rules fail to rationalize the structures of polar intermetallic phases, especially those involving transition metals.[5] The significant difference in electronegativity in Zintl phases creates a large formal charge transfer with the electropositive element essentially donating its valence electrons to the electronegative element. This almost complete donation creates a more polar interaction in the Zintl compounds compared to the Hume-Rothery and polar intermetallics. Zintl phases can be described using conventional electron counting rules such as the octet rule. Between the two extremes of Hume-Rothery phases and Zintl phases are the polar intermetallics, in which there are still significant differences between

electronegativities of components, although there is also significant covalent bonding, as seen in Zintl phases, in the anionic sublattice of the structure.[5] Even though there is covalent bonding in Zintl phases and Polar intermetallics, the latter cannot be easily described by any of the conventional valence electron counting methods.[5] The bonding in polar intermetallic compounds often involves multicenter interactions in which electrons are delocalized. In comparison, bonding in Zintl phases can be viewed as two-center two-electron bonds without usual the degree of delocalization that is present in the polar intermetallic compounds.[6]

Structurally these different classifications have distinctive features. Hume-Rothery phases contain condensed structures with covalent bonding and generally high coordination numbers and are poor metals. Polar intermetallic compounds have varied bonding types and often contain complex structures with no universal bonding rationale. Zintl phases contain open frameworks with lower coordination numbers and significant ionic bonding while following the octect/Wade's rules.[5]

Another way to view this categorization of intermetallic compounds is by looking at the valence electrons per atom (*e/a*) ratio. **Figure 1.1.1** shows a spectrum from Hume-Rothery phases to Zintl phases and the corresponding *e/a* values associated with each. Cu_5Zn_8 has a complex cubic structure with an *e/a* ratio of 1.62,[7] which indicates, from **Figure 1.1.1**, that it is a Hume-Rothery phase. NaTl is the prototypical Zintl phase. Each Na donates the valence 3s electron to a Tl atom thus creating a Tl^- anion with 4 valence electrons. In the process of the electron counting only the electronegative metal is considered giving NaTl an e/a of 4. This causes the Tl^- to create 4 bonds with other Tl atoms and thus creates the diamond network with the Na^+ acting as a space filler.[8]

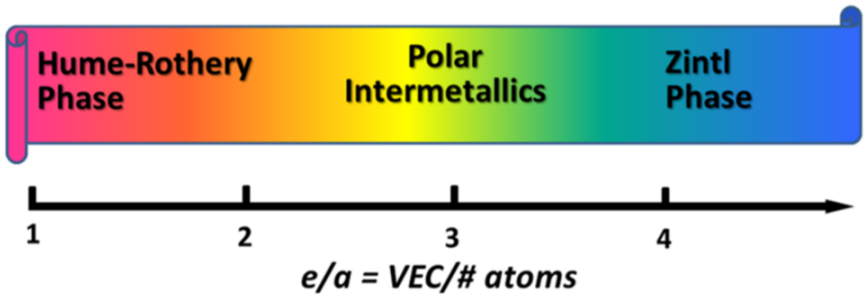

Figure 1.1.1 *e/a* ratios for the three types of intermetallic compounds.[5]

1.2 Laves Phases

Laves phases are an important and vast family of AB_2 compounds, with more than 1400 binary and ternary phases reported.[9] They have been studied for possible applications, due to their strength up to very high temperature; however, they have a major limitation in their brittleness.[9] There are three principle crystal structure types that the Laves phases adopt: the cubic $MgCu_2$ (C15); the hexagonal $MgZn_2$ (C14); and hexagonal $MgNi_2$ (C36) structure types.[10] The majority component atoms create a 3D network which is made up of B_4 tetrahedra. In the $MgCu_2$ and $MgZn_2$ structures, these tetrahedra are arranged in the same manner as the individual atoms in the cubic and hexagonal diamond, respectively. The Mg atoms in these two structures also are arranged in the respective diamond networks so their crystal structures can be described as two inter-penetrating diamond networks. The $MgNi_2$ structure is a 1:1 integration of the $MgCu_2$ and $MgZn_2$ crystal structures.

The lattices in the Laves phases can be described by the layers the majority component form. The B atoms form layers which are referred to as a Kagomé nets, or (3636) nets. Depending on the stacking of these Kagomé nets, the three different basic structures arise:[9] the cubic stacking found in $MgCu_2$ is described as (ABC) stacking; the stacking found in hexagonal $MgZn_2$ is (AB) stacking; and the $MgNi_2$ structure is a combination of these two stacking variations and is described as (ABAC) stacking.[11] These layers of Kagomé nets are

separated by other B atom planes. The stacking sequences can be seen in **Figure 1.2.1.** More complicated stacking sequences with 6-, 8-, 9-, 10-, and 21-layer structures have been found in Mg-based Laves phase systems by Komura et. al.[9]

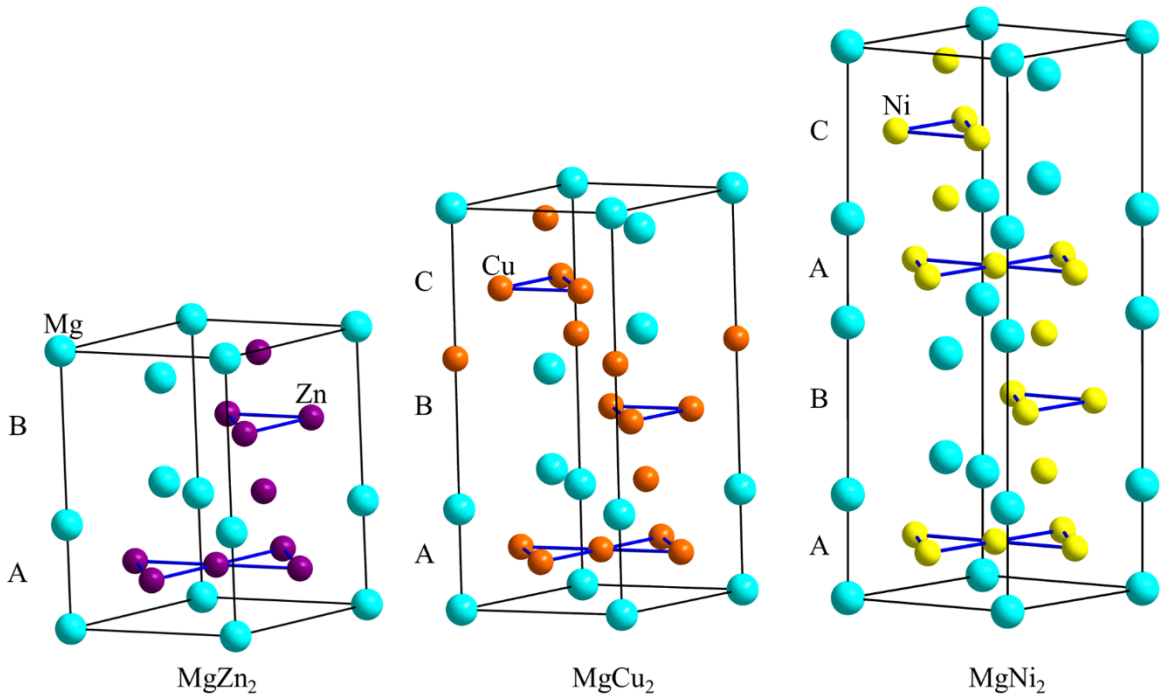

Figure 1.2.1. The stacking sequences as seen in $MgZn_2$ (left) $MgCu_2$ (middle) and $MgNi_2$ (right).

The A atoms reside in the center of a 16-atom Frank-Kasper polyhedron while the B atoms reside at the center of icosahedra. A atoms have a coordination number (CN) of 16 consisting of 4 A atoms and 12 B atoms while each B atom have a CN of 12: 6 A atoms and 6 B atoms.[9] The Laves phases cannot be easily rationalized by electron counting rules like the Zintl phases and Hume-Rothery phases; however, there is a relationship between the valence electron count (VEC) and which structure a system adopts.[12]

To optimize physical properties additional elements have been incorporated into the crystal structures of Laves phases. This can be done in one of two ways: (1) mixed site

occupancy at one of the sites can be achieved; or (2) a fully ordered, ternary Laves phase can be made, which crystallizes as some type of superstructure of the C15, C14, or C36 structures.[11] One of the first examples of a rhombohedrally distorted cubic $MgCu_2$-type unit cell was found in another binary, $TbFe_2$, which distorts the cubic structure due to magnetostriction under high pressure. Fully ordered ternary Laves phases have been found with the general formulas of A_2B_3B' and $AA'B_4$ with many different ordered variants being continuously reported.[13] The addition of a third or even fourth element into the lattice of the Laves phases raises the question where will the element go?

1.3 Coloring Problem

To address this question of where the added elements go the coloring problem can be examined. If a compound has a set stoichiometry and more than one element dispersed throughout the crystal structure the question arises, what is the best way to distribute the atoms throughout the crystal structure? This is the "coloring problem" that can be analyzed in a couple of ways.[14] One method is to take the formula unit and multiply it so all elements have whole integers in the formula unit. This can be the starting point and models with different numbers of homo- and hetero-atomic interactions can be amde.[15] Examples of this type of modeling can be found in **Figure 1.3.1**, which show four different models for the compound $GdCo_{1.33}Ga_{0.67}$. The smallest supercell that contains fully stoichiometric ratios is $Gd_6Co_8Ga_4$ however this unit cell would create unphysical Gd−Gd distances so the cell is expanded more to $Gd_{12}Co_8Ga_4$. The atoms with mixed occupancy are then dispersed in different ways which affects the number of homo- and heteroatomic interactions in the structure. Calculating the total energies of these different models can give information on the electronic significance of homo-atomic and hetero-atomic interactions that influence structural stability. Crystal orbital

Hamilton population (COHP) curves along with the integrated crystal orbital Hamilton population (ICOHP) values, an indication of strength of the pairwise interaction, can also be calculated for the models. The COHP curves and ICOHP values can shed light on how the pairwise interactions are affected by the changes of coordination environment and numbers of homo-atomic/hetero-atomic interactions.

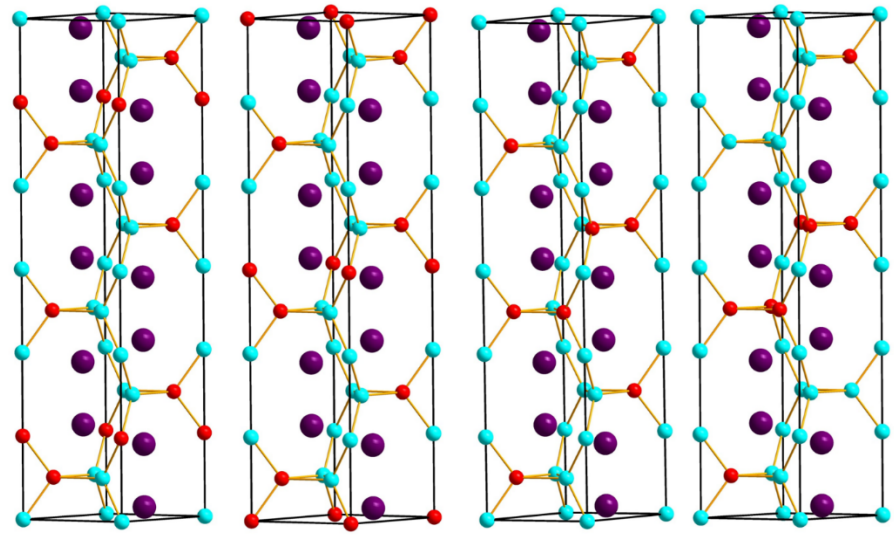

Figure 1.3.1. Four coloring models created for $GdCo_{1.33}Ga_{0.67}$.

Another method to address the coloring problem is doing a Mulliken population or Bader charge analysis of the different sites using an overall isoelectronic homonuclear structure, which will show differences in the number of valence electrons assigned to different atomic sites. Generally, in moving to a respective heteronuclear structure the most electronegative atom will reside in the position with the largest population.[16] The site energy, energy contribution from the valence electrons, and the bond energy are two energetic contributions to the ordering of elements. In purely covalent compounds the site energy would be minimal and the bond energy will dominate while the reverse is true for ionic compounds. The population analysis gives an indication of the lowest energy decoration of the structure.[16]

1.4 Elements

Previous work in the Miller group has focused on using Au as one of the elemental components. This is because Au has a large versatility in the structures it can form. It can exist in structures as condensed clusters, 3D networks, or as complex frameworks which can even lead to quasicrystals and other phases. Au has the highest electronegativity of all the metals and contains the largest contraction of the 6s subshell due to relativistic affects.[17] The work presented in the following chapters focuses on the element Pt. Pt has the second largest contraction of the 6s subshell due to relativistic effects[18] and thus experimental research was performed to determine if the structural versatility that is found with Au can also be seen with Pt.

Ga was chosen due to its room temperature melting point. The low melting point of Ga creates a solution in the experimental vessel that helps dissolve Pt with its high (2041 K) melting point. The Pt-Ga phase diagram shows several binary compounds with varying mole percent (14-75%) of Pt. In general, the trend across the phase diagram is the larger mole percent of Pt the higher the melting point. $PtGa_6$ melts incongruently at 563 K while the more Pt rich compound Pt_2Ga melts incongruently at 1422 K.[19]

The alkaline-earth metals are electropositive and thus would be expected to donate valence electrons to the much more electronegative Pt. The choice of Mg, Ca, and Sr was made to understand how structures might change due to the difference in sizes between the small polarizing Mg compared to the larger and polarizable Sr. The experimental synthesis and analysis work performed for this thesis consisted of AE-M-Ga (AE=Mg, Ca, Sr; M=Pt, Pd) compounds.

Another project, on a series of $GdCo_{2-x}Ga_x$ (X = 0, 0.33, 0.67, 1, 1.33, 1.67, 2) compounds, involving only theoretical electronic structure calculations was performed in collaboration with Fang Yuan and Yurij Mozharivskyj, who synthesized and characterized the compounds. $GdCo_2$ crystallizes in the cubic $MgCu_2$-type Laves phase and has the highest Curie temperature (400 K),[20] the temperature at which the solid undergoes a spontaneous change to ferromagnetism,[21] of all of the $RECo_2$ (RE = Rare Earth) compounds. Compounds with a Curie temperature near to room temperature can be used in commercially viable magnetic refrigeration devices. Magnetic refrigeration works in a comparable way to conventional gaseous refrigeration. However, instead of adiabatically compressing/expanding a fluid, a solid sample is adiabatically magnetized/demagnetized to create the temperature difference.[22] The use of solid compounds with large magnetocaloric effects can be more environmentally friendly than the gases that are currently required in refrigeration techniques.[23]

Electronic structure calculations were used to shed light on the driving forces behind structural changes between X = 0.33−0.67 (cubic → hexagonal), 0.67−1 (hexagonal → orthorhombic), 1-1.33 (Pnma → Imma), and finally 1.33−1.67 (orthorhombic → hexagonal) with increasing Ga content. Electronic structure calculations were also used to investigate the correct arrangement of atoms, in compounds with disordered sites, due to the similar scattering factors of Co and Ga (Z= 27 and 31). These similar scattering factors can make it difficult to distinctly assign Co and Ga to specific sites solely using X-ray crystallography and so computations assisted with experimental characterization. Additionally, results from optimization of the GdCoGa compound prompted added synthetic work and further analysis due to large disagreements between the experimental and theoretical results.

The series of $GdCo_{2-x}Ga_x$ compounds change structure with increasing Ga content. The system with no Ga added crystalizes the polar intermetallic cubic Laves phase consisting of a condensed cluster-based structure. When Ga has replaced 50% of the Co (X = 1, 1.33) the structure changes to a 3D network polar intermetallic and finally when X = 1.67 changes to a 2D network Zintl-like structure. This trend of structure changes follows the trend found in GdX_2 (X = Co, Ni, Cu, Zn, Ga) binary compounds as the valence electron count is increased, except for the $MgZn_2$-type Laves phase structure that $GdCo_{1.33}Ga_{0.67}$ adopts.

1.5 Organization of Dissertation

Chapter 2 describes the general experimental and theoretical methods used in performing the research described in this thesis.

Chapter 3 addresses the coloring problem for the rhombohedral distortion of the cubic $MgCu_2$-type Laves phase of CaM_2 (M=Pt, Pd) by the substitution of 25 % of the M by Ga to create the ternary compound Ca_2M_3Ga (M=Pt, Pd).

Chapter 4 looks at the structure of the compound Ca_2Pd_2Ga and the theoretical study performed to determine the actual structure. It had been previously reported as monoclinic however; synthetic work performed for this thesis shows it is orthorhombic.

Chapter 5 is the result of a collaboration with Fang Yuan and Yurij Mozharivsky from McMaster University in Canada. It is an overview of the experimental results of the $GdCo_{2-x}Ga_x$ system and initial calculations on the stoichiometric endpoints and middle GdCoGa compounds.

Chapter 6 expands on the computational problem laid out in chapter 5 and does more analysis of the mixed site ternary compounds involved in the $GdCo_{2-x}Ga_x$ system.

Chapter 7 describes the general conclusions that have come from the research performed.

1.6 References

1. Pöttgen, R. *Z. Anorg. Allg. Chem.* **2014**, *640(5)*, 869-891.
2. Westbrook, J.H.; Fleischer, R.L. *Intermetallic Compounds: Principles and Practice,* Wiley, 2002.
3. Smetana, V.; Rhodehouse, M.; Meyer, G.; Mudring, A-V. *Acc. Chem. Res.* **2017**, *50*, 2633-2641.
4. Korber, N. *Z. Anorg. Allg. Chem.* **2012**, *638(7-8),* 1057-1060.
5. Lin, Q.; Miller, G.J. *Acc. Chem. Res.* **2018**, *51,* 49-58.
6. Suen, N.T.; Bobev, Svilen. *Inorg. Chem*. **2013**, *52*, 12731-12740.
7. Degtyareva, V.F. *et al*. *Metallurgical and Materials Transactions A*. **2006**, *37A,* 3381-3385.
8. Wang, F.; Miller, G.J. *Inorg. Chem.* **2011**, *50*, 7625-7636.
9. Stein, F.; Palm, M.; Sauthoff, G. *Intermettallics* **2004**, 713-720.
10. Osters, O. et. al. *Inorg. Chem.* **2012**, *51,* 8119-8127.
11. Siggelkow, L.; Hlukhyy, V.; Fässler, T.F. *Z. Anorg. Allg. Chem.* **2017**, *643,*1424-1430.
12. Amerioun, S.; Yokosawa, T.; Lidin, S.; Häussermann, U. *Inorg. Chem.* **2004**, *43*,4751-4760.
13. Seidel, S. et. al. *Z. Naturforsch.* **2017**, *72(4)b*, 289-303.
14. Burdett, J.K.; Canadell, E.; Hughbanks, T. *J. Am. Chem. Soc.* **1986**, *108,* 3971-3976.
15. Gimarc, B.M. *J. Am. Chem. Soc.* **1983**, *105*, 1979.
16. Miller G.J. *Eur. J. Inorg. Chem.* **1998**, 523-536.
17. Miller G.J. et. al. *Mater. Res. Soc. Symp. Proc.* **2013**, *1517*.
18. Jansen, M. *Solid State Sciences* **2005**, *7*,1464-1474.
19. Okamoto, H. *Binary Phase Diagrams, II Ed. T.B. Massalski,* **1990**, *2,* 1840-1842.
20. Khmelevskyi, S.; Mohn, P. *J. Phys. Condens. Matter* **2000**, *12*, 9453-9464.
21. Charles Kittel, *Introduction to Solid State Physics*, John Wiley & Sons Inc., **2005**, New York, 8th.
22. Gschneiddner *et al. Rep. Prog. Phys.* **2005**, *68*, 1479-1539.
23. Pecharsky, V.K.; Gschneidner, K.A. *Phys. Rev. Lett.* **1997**, *78(23),* 4494-4497.

CHAPTER 2. EXPERIMENTAL AND COMPUTATIONAL DETAILS

This chapter describes, in a general way, the synthetic and analytic procedures used for the research presented in this thesis. Further details for each method can be found in subsequent chapters. Each technique is briefly described along with a few uses for and limitations of the technique.

2.1 Synthesis

2.1.1 Starting Materials

High purity elements as listed in **Table 2.1.1** were used for all syntheses. All elements used were stored and weighed in a N_2-filled glovebox, moisture $\leq$ 0.1 ppm, due to the air-sensitivity of the alkaline-earth metals.

Table 2.1.1. Starting Materials used for synthetic preparations.

Element	Source	Melting Point (K)	Purity	Form
Mg	Alfa Aesar	923	99.98%	Turnings
Ca	Sigma-Aldrich	1115	99.99%	Chunks
Sr	Alfa Aesar	1050	99.9%	Chunks
Pt	Ames Laboratory	2041	99.98%	Spheres
Pd	Ames Laboratory	1828	99.999%	Chunks
Ga	Alfa Aesar	303	99.99%	Ingot
In	Alfa Aesar	430	99.99%	Teardrops
Ag	Alfa Aesar	1235	99.9%	Powder

2.1.2 Sample Containers

The vessel used to carry out experiments is an important choice in high-temperature solid state chemistry experiments. The elements need to be protected from air and not react with the container used. For all experiments reported in this thesis, samples were loaded into Ta tubes in a N_2-filled glovebox and these tubes were subsequently sealed by arc-welding

under an argon atmosphere. The sealed Ta containers were then placed in fused silica tubes, which were sealed under vacuum to protect the Ta containers from oxidation at elevated temperatures. The alkaline-earth metals will react with fused silica at reaction temperatures, thereby justifying the use of Ta containers inside of the fused silica jackets.

2.1.3 Tube Furnaces

Tube furnaces are invaluable tools to the solid-state chemist. The furnaces used for the research presented in this thesis have an upper limit of ~1200 ^{0}C, due to the material used to make the coil in the furnace. These furnaces, when controlled with a programmable temperature controller, give a great degree of control over the heating scheme used. The rate of heating and cooling can be controlled very carefully as well as how long the furnace holds at each pre-set temperature. In general, two cooling schemes can be used with the tube furnaces: quenching or slow cooling. Quenching is when the sample is removed from the furnace and placed in water to return to room temperature very quickly. This can be advantageous in isolating metastable compounds; however, crystal quality is generally not as good as slowly cooling due to the crystals not growing over an extended period.

2.1.4 Arc Melting

Arc melting is another technique for synthesis, especially of intermetallic compounds. Starting materials are placed on a water-cooled Cu hearth under an inert Ar atmosphere. An arc is struck between the electrode and the hearth which can reach temperatures over 2500 K very quickly. Samples are arc-melted 6-7 times, flipping the sample over after each arc-melting. This creates the most homogeneous sample possible and prevents the least dense liquid element from “floating” to the top of the button. Samples are generally annealed in a tube furnace after arc-melting to ensure the buttons are homogeneous and at equilibrium.

2.2 Characterization

2.2.1 Powder X-Ray Diffraction

The first characterization of all synthesized samples was by powder X-Ray diffraction. Samples were tested on a Stoe Stadi P diffractometer equipped with a position-sensitive image-plate detector and using Cu $K_{\alpha 1}$ radiation with a wavelength of 1.54060 Å. A portion of the overall sample ~50 mg was ground in an agate mortar and pestle to a fine powder with particle sizes no larger than 150 microns. The powder was placed between two lightly greased mylar discs and placed in the sample holder. WinXPow[1] was used to do initial data analysis and Powdercell[2] was used for phase purity analysis. Experimental powder patterns were overlaid on previously known compounds' patterns to determine if a new compound had been made. Simulated powder patterns from single crystal refinements were also overlaid onto the experimental patterns to determine the purity of a newly discovered phase. An advantage of powder X-Ray diffraction is that since a powder with multiple particles is examined, the results are an average of the bulk. However, it can be more difficult to get accurate structural data from powder X-Ray diffraction compared to single crystal X-Ray diffraction.

2.2.2 Single Crystal X-Ray Diffraction

After powder X-ray analysis showed that a new phase had been made, single crystals were picked out and tested to determine their accurate crystal structure on two instruments: a *STOE-IPDS II* and a *Bruker SMART APEX CCD*. Both instruments used Mo $K_{\alpha 1}$ radiation with a wavelength of 0.71073 Å. The *STOE* instrument was used exclusively in the research presented for testing crystals to then run on the *Bruker* instrument. The single crystals were picked under a microscope and then affixed to a narrow fused-silica fiber using grease.

Data acquisition schemes were either determined by the Apex data collection strategy or a set of pre-determined scans. After the data were collected, analysis was performed using the *SAINT* and *SADABS* programs.[3] Absorption correction was also handled during the analysis using the *SADABS* program. After the initial data work-up, the crystal structures were refined using the *SHELXTL* package.[4,5] Refinements were performed using direct methods and refined by the full-matrix least-squares on F^2.

For each new compound discovered, crystals were tested and refined in this manner until a minimum of three single crystals that agreed within standard deviations of each other were found. After refinements were completed, the crystal structures were drawn using the program *Diamond*.[6] Single crystal diffraction can give very accurate structural data, although it does not necessarily accurately represent the bulk because during this analysis technique only one individual crystal is being examined.

2.3 Electronic Structure Calculations

2.3.1 TB-LMTO-ASA

The tight-binding approach using the linear muffin-tin orbital with the atomic sphere approximation[7,8] (TB-LMTO-ASA) is the first of two computational methods used for the research presented. This program was developed in Stuttgart. TB-LMTO-ASA uses Wigner-Seitz (WS) spheres that surround each atom. This causes spherical basis functions, i.e. atomic orbital-like wavefunctions to completely fill space in the unit cell. Overlap of these spheres is generally restricted to ~16%. If all of space cannot be filled with this overlap restriction, empty spheres, set to have zero nuclear charge, can be added. For all calculations presented in this thesis no empty spheres were needed to achieve 100% space filling.

TB-LMTO-ASA was used in this research to calculate density of states (DOS) curves, crystal orbital Hamilton population (COHP) curves, and band structures. The COHP curves, along with the integrated crystal orbital Hamilton population (ICOHP), can give useful information about the nature and relative strengths of pairwise interactions within the crystal structure.

An advantage of TB-LMTO-ASA is that it is very efficient and quick at calculating band structures, or large unit cells, using a large number of *k*-points. However, a disadvantage is the overlap requirement of the WS spheres used in the *ASA* approximation. It is difficult to maintain constant WS sphere sizes when performing calculations on multiple compounds with different sizes and symmetries. For a valid comparison to be made between compounds, the WS sphere size for corresponding elements must be the same thus providing the limitation of comparing total energies calculated using TB-LMTO-ASA of multiple compounds or models where these sizes cannot be identical. TB-LMTO-ASA also treats the valence and core electrons separately and this can cause a few issues if valence *f* electrons are added into the calculation, such as when trying to perform calculations on Gd compounds.

2.3.2 VASP

The second computational method employed in this research is that of the Vienna Ab initio Simulation Package (VASP). VASP uses pseudopotentials or the projector-augmented wave method with a plane-wave basis set.[9-11] A main advantage of this method is that the electron densities are independent of the atomic positions. This gives relatively easy convergence for structural optimizations and total energy calculations on many compounds and theoretical models. A disadvantage of using VASP is that the chemistry is lost during the calculation. There is no way solely using the VASP program to get bonding information from

the calculation. Dronskowski and his group have developed a program that can be used with VASP calculations to retain some of the chemistry of the calculations. The Local Orbital Basis Suite Towards Electronic-Structure Reconstruction (LOBSTER) can use the output files from VASP and create DOS, COHP, and pCOHP curves.[12,13] For this research VASP was used to calculate total energies, magnetic moments, structural optimizations, and energy vs. volume curves. VASP can be used with the local-density approximation (LDA)[14] or with the local spin-density functional (LSDA)[15] depending if a magnetic moment is desired or not.

Strongly correlated electrons, like the 4*f* electrons in Gd, sometimes need an additional parameter to be handled more appropriately. This parameter is called a Hubbard U term and calculations were then run with the exchange correlation of LSDA+U.[16,17] This is a term that can be optimized but for the research presented here, a value of U = 6.70 and J = 0.70 was used for all calculations.[18] A Hubbard U term is needed for accurate calculations when there is a strong on-site Coulomb interaction of localized electrons, such as localized *d* or *f* electrons. This strong interaction is not appropriately described by either LDA or GGA. The U and J term are independent terms that indicated the strength of the onsite Coulomb and on-site exchange, respectively.[19] The total energy of the system changes with the addition of and varying of the U term and thus only those models calculated with identical U terms can be energetically compared with any relevance.

2.4 References

1. *STOE WinXPOW,* Stoe & Cie GmbH, Darmstadt, Germany, **2011**.
2. *PowderCell*, version 2.3, Federal Institute for Materials Research and Testing: Unter den Eichen, Berlin, Germany, **2000**.
3. Sheldrick, G.M.; University of Göttingen: Göttingen, Germany, **2001**.
4. Sheldrick, G.M.; *Acta Crystallogr. A* **2008**, *64*, 112.

5. *SHELXTL,* version 6.10, Bruker AXS Inc.: Madison, WI, **2000**.
6. *Diamond,* version 3.2; Crystal Impact: Bonn, Germany, **2010**.
7. Anderson, O.K. *Phys. Rev. B* **1975**, *12*, 3060.
8. Anderson, O.K.; Jepsen, O. *Phys. Rev. Lett.* **1984**, *53*, 2571.
9. Kresse, G.; Furthmüller, J. *Comput. Mater. Sci.* **1996**, *6*, 15.
10. Kresse, G.; Furthmüller, J. *Phys. Rev. B.* **1996**, *54*, 11169.
11. Kresse, G.; Hafner, J. *Phys. Rev. B* **1993**, *47*, 558.
12. Dronskoski, R.; Blöchl, P.E. *J. Phys. Chem.* **1993**, *97,* 817-8624.
13. Deringer, V.L.; Tchougréeff, R.; Dronskowski, R. *J. Phys. Chem. A* **2011**, *115*, 5461-5466.
14. Kohn, W.; Sham, L.J. *Phys. Rev.* **1965**.
15. Langreth, D.C.; Perdew, J.P. *Solid State Communications*. **1975**, 1425-1429.
16. Liechtenstein, A.I.; Anisimov, V.I.; Zaanen, J. *Phys. Rev. B.* **1995**, *52,* 5467-5470.
17. Dudarev, S.L.; Savrasov, S.Y.; Humphreys, C.J.; Sutton, A.P. *Phys. Rev. B.* **1998**, *57*, 1505-1509.
18. Yao, J.; Zhang, Y.; Wang, P.L.; Lutz, L.; Miller, G.J. Mozharivskyj, Y. *Phys. Rev. Lett.* **2013**, *110*, 1-5.
19. Liectenstein, A.I.; Anisimov, V.I.; Zaane, J. *Phys Rev. B*, **1995**, *52*, R5467.

CHAPTER 3. RHOMBOHEDRAL DISTORTION OF THE CUBIC $MgCu_2$-TYPE STRUCTURE IN Ca_2Pt_3Ga AND Ca_2Pd_3Ga

Modified from a publication in the journal *Crystals*
(*Crystals* **2018**, *8(5),* 186)

Asa Toombs [1,2] and Gordon J. Miller [1,2,*]

[1] Department of Chemistry, Iowa State University, Ames, IA 50011-3111, USA;
[2] Ames Laboratory, U.S. Department of Energy, Ames, IA 50011-3111, USA

3.1 Abstract

Two new fully ordered ternary Laves phase compounds, Ca_2Pt_3Ga and Ca_2Pd_3Ga, have been synthesized and characterized by powder and single-crystal X-ray diffraction along with electronic structure calculations. Ca_2Pd_3Ga was synthesized as a pure phase whereas Ca_2Pt_3Ga was found as a diphasic product with Ca_2Pt_2Ga. Electronic structure calculations were performed to try and understand why $CaPt_2$ and $CaPd_2$, which crystalize in the cubic $MgCu_2$-type Laves phase structure, distort to the ordered rhombohedral variant, first observed in the magneto-restricted $TbFe_2$ compound, with the substitution of twenty-five percent of the Pt/Pd with Ga. Electronic stability was investigated by changing the valence electron count from $22e^-$/f.u. in $CaPd_2$ and $CaPt_2$ (2x) to $37e^-$/f.u. in Ca_2Pd_3Ga and Ca_2Pt_3Ga, which causes the Fermi level to shift to a more energetically favorable location in the DOS. The coloring problem was studied by placing a single Ga atom in each of four tetrahedra of the cubic unit cell of the $MgCu_2$-type structure, with nine symmetrically inequivalent models being investigated. Non-optimized and optimized total energy analyses of structural characteristics, along with electronic properties, will be discussed.

3.2 Introduction

Platinum exhibits the second largest relativistic contraction of the 6s orbitals, second only to Au [1], and has interesting catalytic properties, thus making it an interesting metal to

study, especially in reduced environments. Exploration of the Ca-Pt-X (X = Ga, In) system revealed a new ternary compound, Ca_2Pt_3Ga, which turned out to be an ordered rhombohedral distortion of the $MgCu_2$-type Laves phase $CaPt_2$. After Ca_2Pt_3Ga was synthesized, the Pd analog was targeted and successfully prepared as an isostructural compound.

Laves phases are the largest class of intermetallic compounds with the general formula AB_2. Binary Laves phases primarily crystalize in one of three crystal structures: $MgCu_2$, $MgZn_2$, or $MgNi_2$ [2]. These structure types, which appear in a vast number of intermetallic systems, contain topologically closed-packed Frank–Kasper polyhedra and have been intensely studied for magnetic and magnetocaloric properties, hydrogen storage, and catalytic behavior [3–9]. The stability of Laves phases has been described by using geometrical and electronic structure factors. Geometrical factors include packing densities and atomic size ratios of A/B whereas electronic factors include valence electron count (*vec*) and difference in electronegativities between A and B [10,11].

To tune the properties and structures of Laves phases, an addition via substitution of a third element into the structure can be explored. The resulting ternary compounds can have mixing on the A and B sites but retain the parent Laves phase structure or the structures can change into a fully ordered ternary Laves phase that is a variant of the parent structure. The first ordered ternary Laves phase with the direct rhombohedral distortion of the $MgCu_2$-type, first evidenced in the binary $TbFe_2$ phase, which distorts via magnetostriction, was reported to be Mg_2Ni_3Si [11,12]. Recently, many examples of this rhombohedral distortion, with varying *vec*, have been reported: RE_2Rh_3Si (RE = Pr, Er), U_2Ru_3Si, $Ce_2Rh_{3+x}Si_{1-x}$, RE_2Rh_3Ge, Ca_2Pd_3Ge, Sm_2Rh_3Ge, U_2Ru_3Ge, Mg_2Ni_3Ge [2], Mg_2Ni_3P, and the heretofore only known gallides RE_2Rh_3Ga (RE = Y, La-Nd, Sm, Gd-Er).

The maximal *translationengleiche* subgroup of the Fd-3m space group that allows for the ordered 3:1 ratio of M:Ga atoms is R-3m [2,3,11]. Reported herein is the first extensive computational study of the "coloring problem" [13] for this rhombohedral distortion of the cubic cell. Formation energies and electronic structure calculations were performed on the binary and ternary Laves phases CaM_2 and Ca_2M_3Ga (M = Pt, Pd) along with total energy calculations of various "coloring models" with the same composition but different atomic arrangements or "colorings".

3.3 Materials and Methods

3.3.1 Electronic Structure Calculations

Electronic structure calculations to obtain DOS and COHP curves for bonding analysis were performed on CaM_2 and Ca_2M_3Ga (M = Pd, Pt) using the Stuttgart Tight-Binding, Linear-Muffin-Tin Orbital program with the Atomic Sphere Approximation (TB-LMTO-ASA) [14]. This approximation uses overlapping Wigner-Seitz (WS) spheres surrounding each atom so that spherical basis functions, i.e., atomic orbital (AO)-like wavefunctions, are used to fill space. The WS sphere radii used for the various atoms are: Ca 3.403–3.509 Å, Pt 2.800–2.844 Å, Pd 2.864–2.865 Å, and Ga 2.800–2.951 Å. The total overlap volume was 6.44% for the cubic Laves phase structures and 7.25% and 7.11%, respectively, for Ca_2Pt_3Ga and Ca_2Pd_3Ga. No empty spheres were required to attain 100% space filling of the unit cells. The exchange-correlation potential was treated with the von Barth-Hedin formulation within the local density approximation (LDA) [15]. All relativistic effects except spin-orbit coupling were taken into account using a scalar relativistic approximation [16]. The basis sets included 4s/(4p)/3d for Ca, 6s/6p/5d/(5f) for Pt, 5s/5p/4d/(4f) for Pd, and 4s/4p/(4d) for Ga (down-folded orbitals are shown in parentheses). Reciprocal space integrations were performed using *k*-point meshes of

1313 points for rhombohedral Ca_2Pt_3Ga and Ca_2Pd_3Ga and 145 points for cubic $CaPt_2$ and $CaPd_2$ in the corresponding irreducible wedges of the first Brillouin zones.

Structure optimization and total energy calculations were performed using the Vienna ab Initio Simulation Package (VASP) [17,18], which uses projector augmented-wave (PAW) [19] pseudopotentials that were treated with the Perdew–Burke–Ernzerhof generalized gradient approximation (PBE-GGA) [20]. Reciprocal space integrations were accomplished over a 13 × 13 × 13 Monkhorst–Pack *k*-point mesh [21] by the linear tetrahedron method [22] with the energy cutoff for the plane wave calculations set at 500.00 eV.

3.3.2 Synthesis

All ternary compounds were obtained by melting mixtures of Ca pieces (99.99%, Sigma-Aldrich, St. Louis, MO, USA), Pt spheres (99.98%, Ames Laboratory, Ames, IA, USA) or Pd pieces (99.999%, Ames Laboratory), Ga ingots (99.99%, Alfa Aesar, Haverhill, MA, USA), and, in some cases, including Ag powder (99.9% Alfa Aesar). Samples of total weight ca. 300 mg were weighed out in a N_2-filled glovebox with <0.1 ppm moisture and sealed in tantalum tubes by arc-melting under an argon atmosphere. To prevent the tantalum tubes from oxidizing during the heating process, they were enclosed in evacuated silica jackets. The silica ampoules were placed in programmable furnaces and heated at a rate of 150 °C per hour to 1050 °C, held there for 3 h, then cooled at 50 °C per hour to 850 °C and annealed for 5 days. The samples were then cooled at 50 °C per hour to room temperature. Ca_2Pt_3Ga crystals were obtained from a loading of "$Ca_2Pt_3Ga_{0.85}Ag_{0.15}$", whereas Ca_2Pd_3Ga crystals were obtained from stoichiometric mixtures of these elements.

3.3.3 Powder X-Ray Diffraction

All samples were characterized by powder X-ray diffraction on a STOE WinXPOW powder diffractometer using Cu *K*α radiation (λ = 1.540598 Å). Each sample was ground using an agate mortar and pestle and then sifted through a US standard sieve with hole sizes of 150 microns. All powder specimens were fixed on a transparent acetate film using a thin layer of vacuum grease, covered by a second acetate film, placed in a holder and mounted in the X-ray diffractometer. Scattered intensities were recorded using a scintillation detector with a step size of 0.03° in 2Θ using a step scan mode ranging from 0° to 130°. Phase analysis was performed using the program PowderCell [23] by overlaying theoretical powder patterns determined from single crystal X-ray diffraction over the powder patterns determined experimentally.

3.3.4 Single Crystal X-Ray Diffraction

Single crystals were extracted from samples and mounted on the tips of thin glass fibers. Intensity data were collected at room temperature on a Bruker SMART APEX II diffractometer with a CCD area detector, distance set at 6.0 cm, using graphite monochromated Mo *K*α radiation (λ= 0.71073 Å). The data collection strategies were obtained both by a pre-saved set of runs as well as from an algorithm in the program COSMO in the APEX II software package [24]. Indexing and integration of data were performed with the program SAINT in the APEX II package [24,25]. SADABS was used to apply empirical absorption corrections [24]. Crystal structures were solved by direct methods and refined by full-matrix least squares on F^2 using SHELXL [26]. The final refinements were performed using anisotropic displacement parameters on all atoms. All crystal structure figures were produced using the program Diamond [27].

3.4 Results

3.4.1 Phase Analysis

Ca_2Pt_3Ga has been synthesized, but not as a pure phase. Using high temperature reactions, this compound can only be synthesized with the addition of a small quantity of silver in the loaded reaction mixture. Without adding silver the binary cubic Laves phase $CaPt_2$ forms as the major product as well as a small amount of some unidentified phase(s) according to X-ray powder diffraction. At reaction and annealing temperatures, Ga, Ca, and Ag are molten and their respective binary phase diagrams indicate miscibility. As Pt dissolves into the liquid, we hypothesize that the presence of Ag slows the reaction rate between Ca and Pt to form $CaPt_2$ and allows Pt and Ga to achieve sufficient mixing in the liquid before crystallizing into Ca_2Pt_3Ga. However, even when synthesized with the addition of silver and at 1050 °C, Ca_2Pt_3Ga does coexists with Ca_2Pt_2Ga and the binary $CaPt_2$. **Figure 3.4.1** shows the powder pattern for the sample loaded as $Ca_2Pt_3Ga_{0.85}Ag_{0.15}$" along with the theoretical patterns for the Ca_2Pt_3Ga and Ca_2Pt_2Ga. Peak fitting analysis performed with Jana [28] can be found in Figure S1 along with relative contributions of the three phases.

Three samples with varying silver content, viz., 2.50, 8.33, and 14.29 mole percent Ag, were examined. According to the XPD patterns (see Figure S3 in Supporting Information), as the silver content increased, the yield of Ca_2Pt_2Ga increased. The outcome was also successfully reproducible for the loading "$Ca_2Pt_3Ga_{0.85}Ag_{0.15}$" (see Figure S4).

On the other hand, Ca_2Pd_3Ga can be prepared without the addition of silver. Since Ag and Pd have similar X-ray scattering factors, using Ag for the synthesis of Ca_2Pd_3Ga would present distinct challenges for subsequent characterization. Fortunately, a stoichiometric loading yielded Ca_2Pd_3Ga essentially as a pure phase product, with two non-indexed peaks at

2θ values of 20.0° and 32.8° most likely coming from a slight impurity of $Ca_3Pd_2Ga_2$ (see **Figure 3.4.2**). Figure S2 shows the Rietveld refinement of Ca_2Pt_3Ga. Both compounds Ca_2Pt_3Ga and Ca_2Pd_3Ga degrade in air after approximately two weeks.

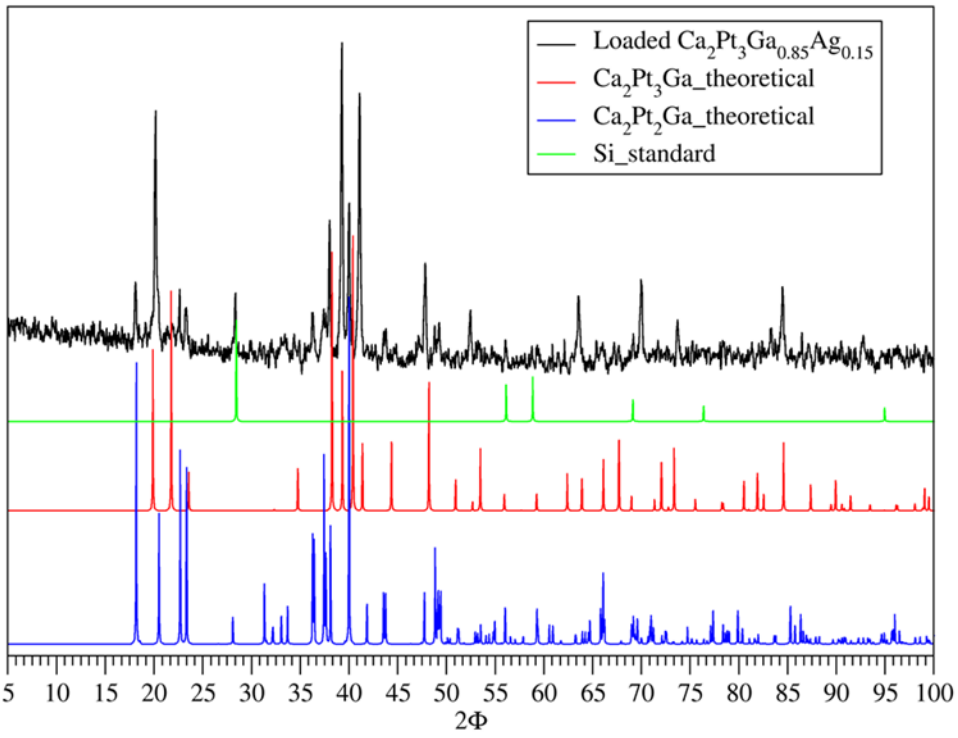

Figure 3.4.1 Powder Patterns for Ca_2Pt_3Ga showing the existence of Ca_2Pt_2Ga in the system.

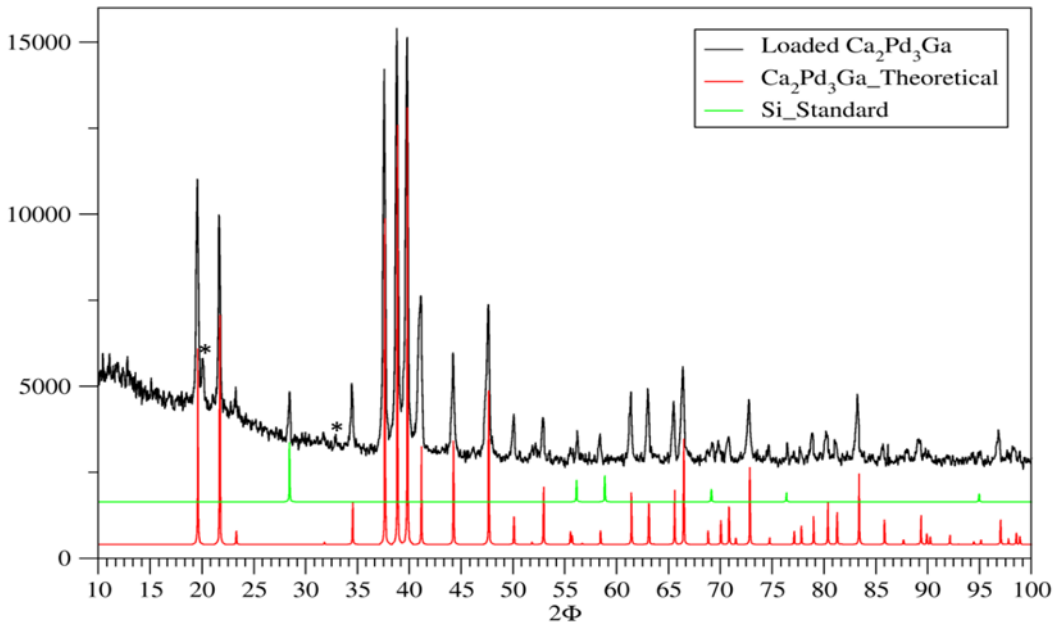

Figure 3.4.2. Powder pattern of sample loaded as Ca_2Pd_3Ga. * = non-indexed peaks coming from slight $Ca_3Pd_2Ga_2$ impurity.

3.4.2 Structure Determination

Several single crystals were selected from the loaded samples and tested on a Bruker SMART APEX II single crystal diffractometer for quality. Among those, the best 3 samples for Ca_2Pt_3Ga and Ca_2Pd_3Ga were examined. The results of single crystal X-ray diffraction on these crystals are found in **Tables 3.4.1** and S3. Ca_2M_3Ga (M = Pt, Pd) crystallize in the Y_2Rh_3Ge structure type [29], which is a rhombohedral distortion of the cubic Laves phase $MgCu_2$-type structure, as discussed by Doverbratt et al. [3] and Siggelkow et al. [2]. The M atoms occupy 9*e* Wyckoff positions which buildup 3.6.3.6 Kagomé nets orthogonal to the *c*-axis [2]. The Ga atoms cap alternate triangular faces of the Kagomé net and themselves form hexagonal nets. The Ga and M atoms are each coordinated by 6 Ga or M atoms. Nine M and three Ga atoms surround each Ca atom in a slightly distorted Frank-Kasper polyhedral environment. The rhombohedral structure of Ca_2M_3Ga has no Ga-Ga nearest neighbor interactions, with distances (6×/6×) of 5.2361(9)/5.576(1) Å and 5.2331(6)/5.6326(8) Å for the

Pt and Pd cases, respectively [3]. For the binary compounds CaM_2, each type of nearest neighbor interaction, i.e., Ca-Ca, Ca-M, and M-M, has a single length. When the structure distorts rhombohedrally to incorporate Ga atoms, the Ca-Ca and Ca-M contacts each split into two different distances: there are three shorter and one longer Ca-Ca interactions; whereas six Ca-M interactions that are longer and three shorter. Atomic positions and anisotropic displacement parameters for both compounds can be found in Tables S1 and S2.

Table 3.4.1. Crystallographic information for Ca_2Pt_3Ga and Ca_2Pd_3Ga.

Sample	Ca_2Pt_3Ga	Ca_2Pd_3Ga
Space Group	*R*-3*m*	*R*-3*m*
Unit Cell Dim.	*a* = 5.576(1) Å *c* = 12.388(3) Å	*a* = 5.6326(8) Å *c* = 12.300(2) Å
Volume	333.6(2) Å^3	337.9(1) Å^3
Z	3	3
Theta range for data collection	4.530 to 28.922°	4.495 to 49.319°
Index ranges	−7<=*h*<=7, −7<=*k*<=7, −16<=*l*<=16	−11<=*h*<=11, −11<=*k*<=11, −26<=*l*<=26
Reflections Collected	1321	4878
Independent Reflections	126 [R(int) = 0.0485	460 [R(int) = 0.0585]
Data/restraints/parameters	126/0/11	460/0/11
Goodness-of-fit	1.078	1.091
Final R indices [I>2sigma(l)]	R1 = 0.0179, wR2 = 0.0403	R1 = 0.0208, wR2 = 0.0403
R indices (all data)	R1 = 0.0179, wR2 = 0.0403	R1 = 0.0251, wR2 = 0.0414
Extinction Coefficient	0.0008(1)	0.0036(3)
Largest diff. peak and hole	3.366 and −2.052 e·Å^{-3}	1.697 and −2.657 e·Å^{-3}

3.4.3 Coloring Models and Electronic Structure Calculations

To elucidate the driving force that leads to the rhombohedral arrangement of Pt/Pd and Ga atoms in the majority atom positions of the cubic Laves phase, Burnside's lemma [30] was used to construct nine distinct structural models for the unit cells formulated as $Ca_8[M_3Ga]_4$ [31]. These models are illustrated in Figure S5 along with their respective space groups. The total energy of each model, listed in **Table 3.4.2**, was calculated using VASP without optimization. These results show that the rhombohedral model (α) is the lowest in energy. There are three models that have no nearest neighbor Ga-Ga interactions, these include the rhombohedral coloring, a cubic coloring (μ), and an orthorhombic coloring (γ). The

rhombohedral and cubic models are the two lowest in energy before optimization, whereas the orthorhombic coloring is the second highest in energy.

All models were then optimized using VASP by allowing all structural parameters, including volume, cell shape, and atomic coordinates, to relax. The energies of the optimized structures can also be found in **Table 3.4.2**. Details of the optimized structures can be found in Tables S5–S13. After optimization, the rhombohedral model remains the lowest energy with the orthorhombic and cubic models coming in second and third lowest energy. The orthorhombic (γ) model optimized to a unit cell with $a \neq b \neq c$ and only $\beta = 90°$, while the other two models retained their symmetry through the optimization. As the energies increase for the various optimized structures, the number of nearest neighbor Ga-Ga interactions increases and the corresponding Ga-Ga distances decrease. **Table 3.4.2** lists the energies after optimization as well as the resulting nearest Ga-Ga distance showing the correlation between total energy and Ga-Ga interactions.

Table 3.4.2. Total energy of non-optimized and optimized coloring models showing optimized Ga-Ga distances.

	Ca_2Pt_3Ga				Ca_2Pd_3Ga		
Model	**Ga-Ga Distance (Å)**	**meV Non-Optimized**	**meV Optimized**	**# Ga-Ga Interactions**	**meV Optimized**	**meV Non-Optimized**	**Ga-Ga Distance (Å)**
Alpha	5.276	0	0	0	0	0	5.282
Beta	2.755	+38.5	+78.8	1	+68.1	+30.5	2.732
Delta	2.811	+62.1	+121.8	2	+121.8	+59.3	2.775
Epsilon	2.808	+50.8	+95.7	1	+73.0	+36.0	2.800
Gamma	4.738	+140.7	+56.0	0	+26.0	+92.0	4.791
Iota	2.931	+70.5	+113.4	2	+104.7	+61.2	2.922
Mu	4.709	+37.6	+71.0	0	+66.5	+13.3	4.653
Theta	2.950	+203.0	+289.4	6	+256.6	+155.5	2.909
Zeta	2.824	+97.6	+168.6	3	+150.0	+81.1	2.798

Calculations have shown that the rhombohedral model is the lowest energy both before and after optimization. This leads to the question of how does the rhombohedral structure arise from the "cubic" arranged starting point? The "cubic" starting point, for Ca_2Pt_3Ga, has a lattice

parameter of 7.598 Å and a body diagonal distance of 13.160 Å. The primitive rhombohedral unit cell, within the face-centered cubic cell, has angles equal to 60° before optimization. After optimization these angles are 57.825° and 57.515° for Ca_2Pt_3Ga and Ca_2Pd_3Ga respectively. This collapsing of the angles, comprising the primitive unit cell, causes the expansion of the body diagonal. Optimization expands the lattice parameter by 1.43% to 7.708 Å. However, during optimization, the body diagonals do not expand congruently. Three body diagonals are congruent with a length of 13.627 Å while the fourth body diagonal shrinks to 12.482 Å. In the Pd case the three equivalent body diagonals are 13.754 Å while the fourth body diagonal shrinks to 12.412 Å. The shorter body diagonal is parallel to the direction that the Ga atoms are located in each of the four tetrahedra in the unit cell (see **Figure 3.4.3**). Calculated ICOHP values for the "cubic" starting point indicate that the Pt-Ga bonds (ICOHP = −1.857 eV) would become shorter as compared with the Pt-Pt bonds (ICOHP = −0.775 eV). These ICOHP values shed light on the driving force behind the corresponding distortion of the cubic unit cell to the rhombohedral structure by substituting Ga for Pd/Pt: shorter Pt-Ga contacts will contract one body-diagonal of the cubic cell.

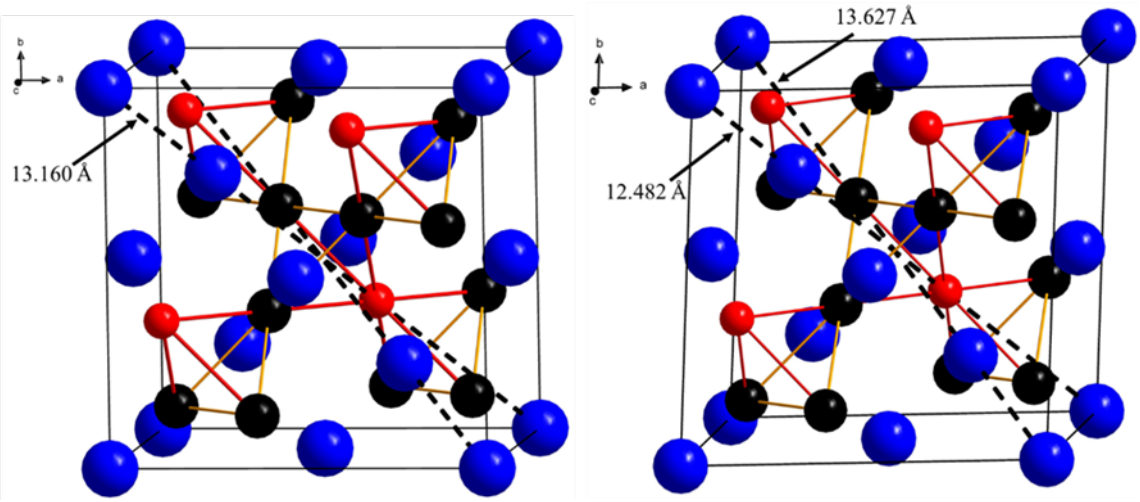

Figure 3.4.3. "Cubic" arranged starting point with 4 congruent body diagonals (**left**) optimized rhombohedral unit cell (**right**) with 3 body diagonals of 13. 627 Å and 1 body diagonal of 12.482 Å. Red colored bonds shrink during optimization causing the reduction in body diagonal length from 011 to 100. Blue, black, and red atoms are Ca, Pt, and Ga respectively.

All "coloring" calculations performed above were evaluated for the case of *vec* = 37e^-/f.u. Models were also created for the Ca_2Pd_3Ge to determine if there were any differences by changing the *vec* to 38 e^-/f.u. The energies of the non-optimized and optimized colorings can be found in Table S4, and the results show the same trends as those for Ca_2M_3Ga (M = Pd, Pt): the lowest energy model shows rhombohedral coloring and the largest Ge-Ge nearest neighbor distance.

To shed light on the nature of the distortion of the cubic Laves phase structure of CaM_2 (M = Pd, Pt) upon the substitution of Ga for M and their stability, various total energies as well as the density of states (DOS) and crystal orbital Hamilton population (COHP) curves were determined for the binaries CaM_2 and ternaries Ca_2M_3Ga (M = Pd,Pt). With respect to the elemental solids, the binaries CaM_2 and ternaries Ca_2M_3Ga are favored. For the experimental structures, $CaPt_2$ has an especially high formation energy compared to $CaPd_2$; the experimental volume of $CaPt_2$ is ca. 10 $Å^3$/formula unit smaller than that of $CaPd_2$, although Pt is slightly

larger than Pd (the 12-coordinate metallic radii are 1.39 (Pt) and 1.37 (Pd) [32]. This outcome may be an indication of relativistic effects on the valence orbitals of Pt, effects which can enhance empty *d*-filled *d* Ca-Pt 3*d*-5*d* interactions as compared to Ca-Pd 3*d*-4*d* interactions.

Total energy calculations for the "reactions" $2CaPt_2 + Ga \rightarrow Ca_2Pt_3Ga + Pt$ and $2CaPd_2 + Ga \rightarrow Ca_2Pd_3Ga + Pd$ illuminate significant aspects of the relative stability and formation of the ternaries. Both "reactions" yield favorable ΔE values, respectively, of −0.297 and −0.599 eV, and they can be separated into the sum of three hypothetical but revealing steps: (1) elemental substitution of Ga for M with no metric changes (volume, unit cell shape) in the cubic Laves phase structure; (2) volume change for the ternary without change in unit cell shape; and (3) distortion of the unit cell shape of the ternary at constant cell volume. **Table 3.4.3** summarizes these results. The difference in overall total energies essentially arises from the energetic difference for step (1) between Pt and Pd cases: replacing Pt with Ga is energetically unfavorable whereas Pd for Ga is favorable. Since Ga (metallic radius of 1.50 Å [32]) is larger than either Pt or Pd, these energy differences reflect, in part, volume effects, but also are influenced by the relative Mulliken electronegativities [33], which increase Ga (3.2 eV) to Pd (4.45 eV) to Pt (5.6 eV). In the second step, both structures favorably expand by over 3% (based on unit cell volume) with slight energetic lowering. In the third step, both lattice distortions provide similar energetic stabilizations.

Table 3.4.3. Relative total energies (eV) for conversion of binary cubic Laves phases CaM_2 into ternary rhombohedral derivatives Ca_2M_3Ga (M = Pd, Pt). * = cubic unit cell metric with volume matching the corresponding binary compound; ** = cubic unit cell metric with volume matching the corresponding rhombohedral ternary compound. Specific total energies (eV/formula unit) for each component are listed in Supporting Information.

	2 $CaPd_2$	**+ Ga**	**→**	**Ca_2Pd_3Ga**	**+ Pd**	**$\Delta E = -0.599$ eV**
(1)	2 $CaPd_2$	+ Ga	→	Ca_2Pd_3Ga *	+ Pd	$\Delta E = -0.258$ eV
(2)	Ca_2Pd_3Ga*		→	Ca_2Pd_3Ga **		$\Delta E = -0.042$ eV
(3)	Ca_2Pd_3Ga**		→	Ca_2Pd_3Ga		$\Delta E = -0.299$ eV
	2 $CaPt_2$	**+ Ga**	**→**	**Ca_2Pt_3Ga**	**+ Pt**	**$\Delta E = -0.297$ eV**
(1)	2 $CaPt_2$	+ Ga	→	Ca_2Pt_3Ga *	+ Pt	$\Delta E = +0.115$ eV
(2)	Ca_2Pt_3Ga*		→	Ca_2Pt_3Ga **		$\Delta E = -0.088$ eV
(3)	Ca_2Pt_3Ga**		→	Ca_2Pt_3Ga		$\Delta E = -0.324$ eV

We now consider some specific aspects of the electronic structures of the binary CaM_2 and ternary Ca_2M_3Ga. The DOS and COHP for $CaPt_2$ are shown in **Figure 3.4.4**; the DOS shows a significant sharp peak at the Fermi level which suggests a potential electronic instability.

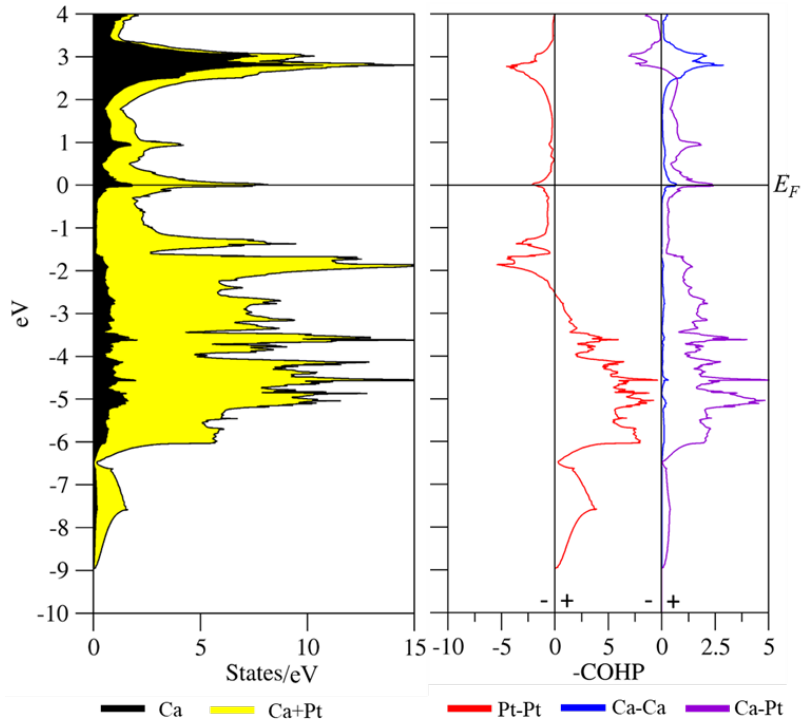

Figure 3.4.4. DOS (left) and -COHP (right) for $CaPt_2$ with +/− indicating bonding/antibonding values of COHP curves. Ca-Ca and Ca-Pt interactions are magnified for comparison.

The precise reason for this peak and the possible instability has not been forthcoming to date and an electronic structure investigation was performed. Analysis of the band structure at the Fermi level, specifically at the W point, because there are bands with nearly zero slope near this point, shows that the Pt 5*d* atomic orbitals are major contributors to this peak. For each Pt atom the orbital contribution is split approximately as 80 percent 5*d* and 20 percent 6*p*, and the primary interatomic orbital interactions are 5*d*-5*d* π* interactions. Spin-orbit coupling was added to the Hamiltonian operator of $CaPt_2$ to see if the peak at the Fermi level would be affected. Figure S6 shows the DOS curve and band structure for these calculations. The degeneracies in the band structure at the high symmetry ***k***-points are removed by the spin-orbit coupling; however, the peak at E_F is not affected. Furthermore, the application of spin-orbit coupling would only converge with a unit cell expanded by ~1.1 Å. A second hypothesis was to consider that vacancies might be playing a role to stabilize the structure. DOS calculations were subsequently performed using VASP on "Ca_8Pt_{15}" and "Ca_8Pt_{12}" models to see the effect of vacancies on the peak at E_F; these results can be seen in Figure S7. The peak is no longer present in the "Ca_8Pt_{12}" model only when all 4 vacancies are adjacent to each other so that the resulting defect Laves phase structure is missing an entire tetrahedron per unit cell. Lastly, DOS curves calculated for AEM_2 (AE = Ca, Sr, Ba; M = Ni, Pd, Pt), shown in Figure S8, indicate that as the size of the alkaline earth metal increases, the peak in the DOS moves away from E_F. These calculations have not identified the reason behind the potential electronic instability in CaM_2 and now the possibility of superconductivity is being investigated.

The Pt 5*d* band dominates the overall occupied DOS of $CaPt_2$ and the majority contribution to the overall polar covalent bonding via ICOHP values arises from Pt-Pt interactions, which switch from bonding to antibonding at an energy value corresponding

to 12.42 e^-/formula unit. At the Fermi level, the Pt-Pt COHP curve shows a small antibonding peak, whereas the Ca-Pt and Ca-Ca COHPs show a small bonding peak. On transitioning to Ca_2Pt_3Ga, the peak at the Fermi level in the DOS of $CaPt_2$ has all but disappeared in the DOS curve of Ca_2Pt_3Ga (see **Figure 3.4.5**). There is a large range from ca. −1.5 to +1 eV over which the DOS of Ca_2Pt_3Ga remains flat. The COHP curves have also changed in that the Pt-Pt interactions still transition to antibonding at −2.60 eV, although around the Fermi level they are mostly nonbonding rather than antibonding. Overall, at the Fermi level there are now no small peaks but mostly constant intensities of nonbonding or slightly bonding interactions with the Ca-Pt interactions still contributing the most to overall bonding.

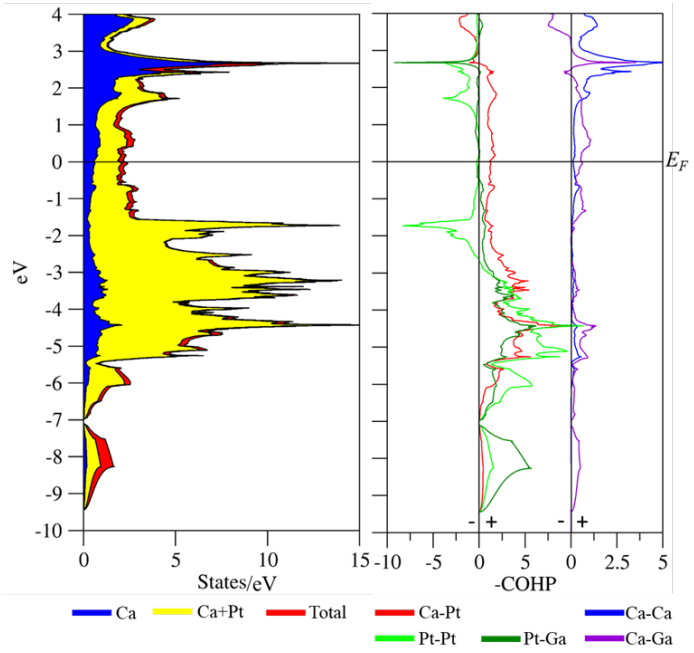

Figure 3.4.5. DOS (**left**) and COHP (**right**) for Ca_2Pt_3Ga with +/- indicating bonding/antibonding values of COHP curves. Ca-Ca and Ca-Ga interactions magnified for comparison.

The DOS and COHP curves for $CaPd_2$ (see **Figure 3.4.6**) and Ca_2Pd_3Ga (see **Figure 3.4.7**) look similar overall to those described above for the Pt counterparts, although there are a few distinct differences. The peak at the Fermi level in the DOS for $CaPd_2$ as well as the

antibonding Pd-Pd peak in the COHP are not as intense nor as sharp as those observed for $CaPt_2$. The Pd-Pd interactions transition from bonding to antibonding at an energy which corresponds to 15.36 eV/formula unit. There is a similar minimum in the Pd 4*d* states at −1.40 eV which corresponds to 7.5 4*d* electrons/Pd. The DOS and COHP for Ca_2Pd_3Ga are similar to those for Ca_2Pt_3Ga. There is again a large energy range from ca. −1.8–1.8 eV over which the DOS remains flat.

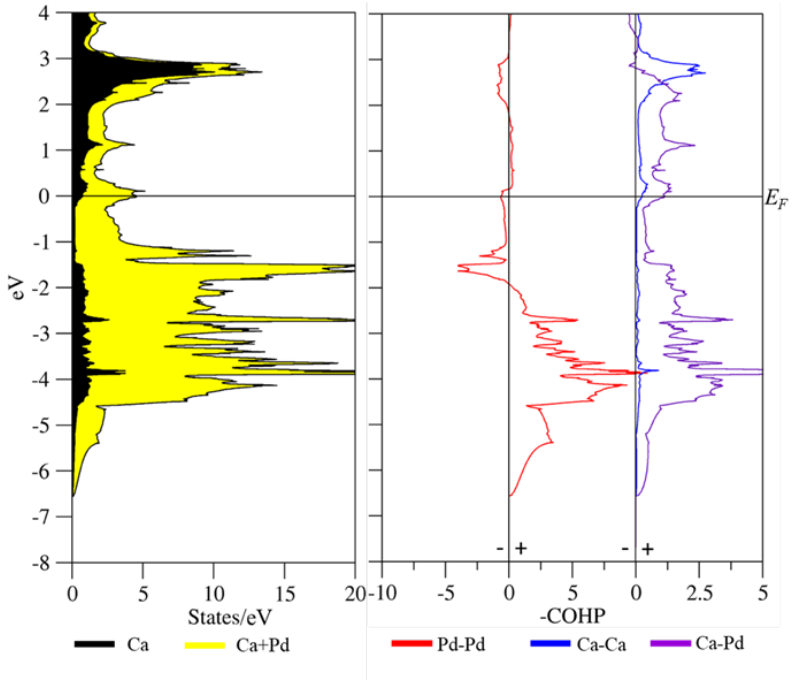

Figure 3.4.6. DOS (**left**) and COHP (**right**) calculated for $CaPd_2$ with +/− indicating bonding/antibonding values of COHP curves. Ca-Pd and Ca-Ca interactions magnified for comparison.

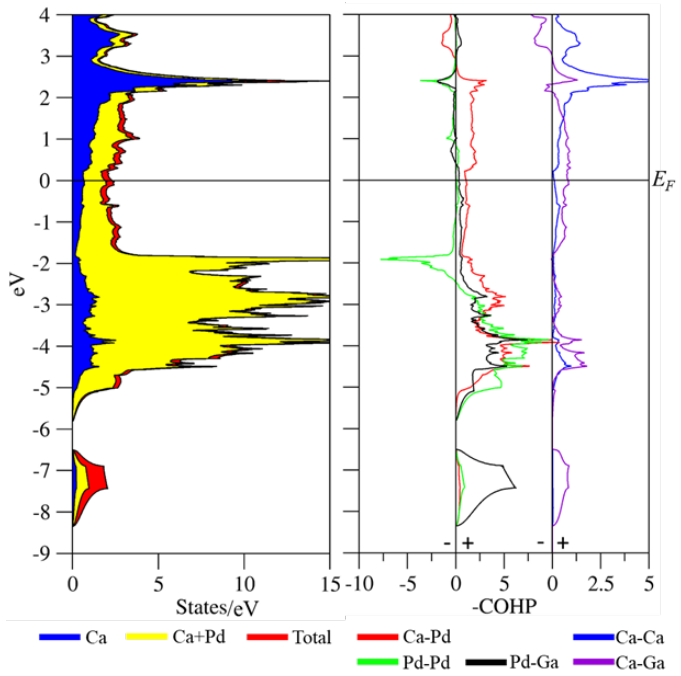

Figure 3.4.7. DOS (**left**) and COHP (**right**) calculated for Ca_2Pd_3Ga with +/− indicating bonding/antibonding values of COHP curves. Ca-Ca and Ca-Ga interactions magnified for comparison.

Tables S14–S17 contain the percent contributions of each type of interaction to the overall integrated COHP (ICOHP) values. These can be used as an indication to determine the bond energy contribution to the stability of a structure. The cubic binary Laves phases are dominated by the M-M (M = Pd, Pt) interactions at 62.95 and 58.41% for $CaPt_2$ and $CaPd_2$, respectively, whereas the Ca-Ca interactions lend little to the overall ICOHP at only 1.47% and 2.12% for $CaPt_2$ and $CaPd_2$, respectively. The rest is made up by the Ca-M interactions. For the ternary compounds, there is a significant drop in the contributions from M-M interactions to the total polar-covalency because the majority of the total ICOHP comes from Ca-M and M-Ga interactions. In Ca_2Pt_3Ga, the Pt-Pt contribution is just 29.95%, and in Ca_2Pd_3Ga, the Pd-Pd contribution is 24.40%. The Ca-M and M-Ga interactions contribute ~30% each in both ternary compounds. Furthermore, in the ternary compounds, there are now

Ca-Ga interactions that account for 5.81% and 7.89%, respectively, in Ca_2Pt_3Ga and Ca_2Pd_3Ga. The Ca-Ca bond populations continue to contribute less than 2.5% in all cases.

The analysis of the integrated Hamilton population curves to study the interatomic interactions is useful for mainly two-center interactions, and the use of crystal orbital overlap population (COOP) analysis has been applied to examine cubic vs. hexagonal Laves phases [34]. However, multi-center chemical bonding in Laves phases has also been described using an electron localizability indicator [35]. Laves phases AB_2 with a small electronegativity difference between the two components exhibit enhanced multi-center bonding because the effective charge transfer between A and B is small. However, if the electronegativity difference between A and B is large, the correspondingly greater effective charge transfer can lead to polyanions [35]. $CaPt_2$ and $CaPd_2$ are cases with a large electronegativity difference between the A and B atoms (3.2 eV for $CaPt_2$ and 2.25 eV for $CaPd_2$ [33]), but there most likely exists some multi-center bonding in these compounds, especially between the faces of the transition metal tetrahedra and the Ca atoms, bonding which would be affected by the substitution of one of the Pt or Pd atoms by Ga. The electronegativity difference between Ga and Ca is not as large (1.0 eV [33]), which creates less charge transfer between Ca and Ga and thereby shifts the valence electron density as compared to the binary structures. Electron localizability indicators were not evaluated during this study, but they would provide useful information regarding specifics of multi-center interactions in the ternary derivatives.

3.5 Conclusions

Two new fully ordered ternary gallium-containing Laves phase compounds, Ca_2Pt_3Ga and Ca_2Pd_3Ga, were synthesized and characterized by X-ray diffraction and electronic structure calculations. The compounds crystallize in a rhombohedrally distorted cubic $MgCu_2$-

type structure. Ca_2Pd_3Ga was synthesized as a pure phase whereas Ca_2Pt_3Ga was only found co-existing with Ca_2Pt_2Ga and $CaPt_2$ and required the addition of small amounts of Ag to form. Total energy calculations performed on nine symmetrically inequivalent "coloring models" indicated that the rhombohedral coloring gave the lowest energy by 78.8 meV and 68.1 meV in the Pt and Pd cases respectively. ICOHP values from the "cubic" starting arrangement indicate that the M-Ga bonds tend to become shorter vs. M-M contacts. These shorter bonds cause a shrinking of the body diagonal from the corner of 011 to 100 which gives rise to the rhombohedrally distorted unit cell.

This computational study supports the group–subgroup relationship that R-3m is the highest maximal subgroup of Fd-3m and allows a fully ordered structure with the 3:1 ratio of M:Ga atoms. The rhombohedral coloring is the lowest energy way to color the "B" network in the Laves phase so that the Ga atoms avoid all homoatomic interactions and have the furthest nearest neighbor distance.

3.6 Acknowledgments

A. Toombs acknowledges J. Pham and L. Lutz-Kappelman for answering many questions involving crystallography and computational guidance along with S. Thimmaiah for helping with the Rietveld refinements. This research was supported by the Office of the Basic Energy Sciences, Materials Sciences Division, U.S. Department of Energy (DOE). The Ames Laboratory is operated by Iowa State University under Contract No. DE-AC02-07C. Computations were performed on the CRUNCH cluster supported by Iowa State University Computation Advisory Committee under Project No. 202-17-10-08-0005.

3.7 Supporting Information

Supporting information for this chapter can be found in APPENDIX A.

3.8 References

1. Jansen, M. Effects of relativistic motion of electrons on the chemistry of gold and platinum. *Solid State Sci*. **2005**, *7*, 1464–1474. doi:10.1016/j.solidstatesciences.2005.06.015.

2. Siggelkow, L.; Hlukhyy, V.; Faessler, T.F. The Influence of the Valence Electron Concentration on the Structural Variation of the Laves Phases $MgNi_{2-x}Ge_x$. *Z. Anorg. Allg. Chem.* **2017**, *643*, 1424–1430. doi:10.1002/zaac.201700180.

3. Doverbratt, I.; Ponou, S.; Lidin, S. Ca_2Pd_3Ge, a new fully ordered ternary Laves phases structure. *J. Solid State Chem.* **2013**, *197*, 312–316. doi:10.1016/j.jssc.2012.09.003.

4. Stein, F.; Palm, M.; Sauthoff, G. Structure and stability of Laves phases. Part I—Critcal assessment of factors controlling Laves phase stability. *Intermetallics* **2004**, *12*, 713–720. doi:10.1016/j.intermet.2004.02.010.

5. Osters, O.; Nilges, T.; Schöneich, M.; Schmidt, P.; Rothballer, J.; Pielnhofer, F.; Weihrich, R. Cd_4Cu_7As, The First Representative of a Fully Ordered, Orthorhombically Distorted $MgCu_2$ Laves Phases. *Inorg. Chem*. **2012**, *51*, 8119–8127. doi:10.1021/ic3005213.

6. Murtaza, A.; Yang, S.; Zhou, C.; Song, X. Influence of Tb on easy magnetization direction and magnetostriction of ferromagnetic Laves phase GdFe compounds. *Chin. Phys. B* **2016**, *25*, 096107. doi:10.1088/1674-1056/25/9/096107.

7. Manickam, K.; Grant, D.M.; Walker, G.S. Optimization of AB2 type alloy composition with superior hydrogen storage properties for stationary applications. *Int. J. Hydrogen Energy* **2015**, *40*, 16288–16293. doi:10.1016/j.ijhydene.2015.09.157.

8. Nash, C.P.; Boyden, F.M.; Whittig, L.D. Intermetallic compounds of alkali metals with platinum. A novel preparation of a colloidal platinum hydrogenation catalyst. *J. Am. Chem. Soc.* **1960**, *82*, 6203–6204. doi:10.1021/ja01508a062.

9. Xiao, C.; Wang, L.; Maligal-Ganesh, R.V.; Smetana, V.; Walen, H.; Thiel, P.A.; Miller, G.J.; Johnson, D.D.; Huang, W. Intermetallic $NaAu_2$ as a Heterogeneous Catalyst for Low-Temperature CO Oxidation. *J. Am. Chem. Soc.* **2013**, *135*, 9592–9595. doi:10.1021/ja403175c.

10. Thimmaiah, S.; Miller, G.J. Influence of Valence Electron Concentration on Laves Phases: Structures and Phase Stability of Pseudo-Binary $MgZn_{2-x}Pd_x$. *Z. Anorg. Allg. Chem.* **2015**, *641*, 1486–1494. doi:10.1002/zaac.201500197.

11. Seidel, S.; Janka, O.; Benndorf, C.; Mausolf, B.; Haarmann, F.; Eckert, H.; Heletta, L.; Pöttgen, R. Ternary rhombohedral Laves phases RE_2Rh_3Ga (RE = Y, La-Nd, Sm, Gd-Er). *Z. Naturforsch.* **2017**, *72*, 289–303. doi:10.1515/znb-2016-0265.

12. Dwight, A.E.; Kimball, C.W. A rhombohedral Laves phase. Terbium-ron ($TbFe_2$) *Acta Cryst. Sect. B* **1974**, *30*, 2791–2793. doi:10.1107/S0567740874008156.

13. Burdett, J.K.; Canadell, E.; Hughbanks, T. Symmetry control of the coloring problem: The electronic structure of MB2C2 (M = calcium, lanthanum,…). *J. Am. Chem. Soc.* **1986**, *108*, 3971–3976. doi:10.1021/ja00274a019.

14. Jepsen, O.; Andersen, O.K. *TB-LMTO*, version 47; Max-Planck-Institut für Festkörperforshcung: Stuttgart, Germany, 2000.

15. Von Barth, U.; Hedin, L. Local exchange-correlation potential for the spin-polarized case. *J. Phys. C* **1972**, *5*, 1629.

16. Koelling, D.D.; Harmon, B.N. A technique for relative spin-polarized calculations. *J. Phys. C* **1977**, *10*, 3107–3114. doi:10.1088/0022-3719/10/16/019.

17. Kresse, G.; Hafner, J. Ab initio molecular dynamics for liquid metals. *Phys. Rev. B* **1993**, *47*, 558. doi:10.1103/PhysRevB.47.558.

18. Kreese, G.; Furthmüller, J. Efficient iterative schemes for ab initio total-energy calculations using a plane-wave basis set. *Phys. Rev. B* **1996**, *54*, 11169–11186. doi:10.1103/PhysRevB.54.11169.

19. Blöchl, P.E. Projector augmented-wave method. *Phys. Rev. B* **1994**, *50*, 17953–17979.

20. Perdew, J.P.; Burke, K.; Wang, Y. Gerneralized gradient approximation for the exchange-correlation hole of a many-electron system. *Phys. Rev. B* **1996**, *54*, 16533–16539.

21. Monkhorst, H.J.; Pack, J.D. Special points for Brillouin-zone integrations. *Phys. Rev. B* **1976**, *13*, 5188. doi:10.1103/PhysRevB.13.5188.

22. Blöchl, P.E.; Jepsen, O.; Andersen, O.K. Improved tetrahedron method for Brillouin-zone integrations. *Phys. Rev. B* **1994**, *49*, 16223–16233.

23. *PowderCell*, version 2.3; Federal Institute for Materials Research and Testing: Berlin, Germany, 2000.

24. *APEX-II*; Bruker AXS Inc.: Madison, WI, USA, 2013.

25. *SAINT-V8.27*; Bruker AXS Inc.: Madison, WI, USA, 2013.

26. *SHELXTL-v2008/4*; Bruker AXS Inc.: Madison, WI, USA, 2013.

27. Brandenburg, K. *Diamond*, version 3.2; Crystal Impact GbR: Bonn, Germany, 2011.

28. Petricek, V.; Dusek, M.; Palatinus, L. *Structure Determination Software Programs*; Institute of Physics: Praha, Czech Republic, 2006.

29. Cenzual, K.; Chabot, B.; Parthe, E. Yttrium rhodium germanide (Y_2Rh_3Ge), a rhombohedral substitution variant of the $MgCu_2$ type. *J. Solid State Chem.* **1987**, *70*, 229–234. doi:10.1016/0022-4596(87)90061-2.

30. Burdett, J.K.; McLarnan, T.J. Geometrical and electronic links among the structures of MX2 solids: Structural enumeration and electronic stability of pyritelike systems. *Inorg. Chem.* **1982**, *21*, 1119–1128. doi:10.1021/ic00133a048.

31. Xie, W.; Miller, G.J. β-Mn-Type $Co_{8+x}Zn_{12-x}$ as a Defect Cubic Laves Phase: Site Preferences, Magnetism, and Electronic Structure. *Inorg. Chem.* **2013**, *52*, 9399–9408. doi:10.1021/ic4009653.

32. Wells, A.F. *Structural Inorganic Chemistry*, 5th ed.; Clarendon Press: Oxford, UK, 1984.

33. Pearson, R.G. Absolute Electronegativity and Hardness: Application to Inorganic Chemistry. *Inorg. Chem.* **1988**, *27*, 734–740.

34. Johnston, R.; Hoffmann, R. Structure-Bonding Relationships in the Laves Phases. *Z. Anorg. Allg. Chem.* **1992**, *616*, 105–120. doi:10.1002/zaac.19926161017.

35. Ormeci, A.; Simon, A.; Grin, Y. Structural Topology and Chemical Bonding in Laves Phases. *Angew. Chem.* **2010**, *49*, 8997–9001. doi:10.1002/anie.201001534.

CHAPTER 4. AN ORTHORHOMBIC VARIANT OF Ca_2Pd_2Ga

Asa Toombs[1,2] and Gordon J. Miller[1,2,*]

[1] *Department of Chemistry, Iowa State University, Ames, IA 50011-3111, USA.*
[2] *Ames Laboratory, U.S. Department of Energy, Ames, IA 50011-3111, USA.*

4.1 Abstract

The compound Ca_2Pd_2Ga was synthesized and characterized from a stoichiometric loading to crystallize in the orthorhombic space group *Cmca*. The previously reported structure type for this compound was the monoclinic Pr_2Co_2Al-type structure, space group *C2*/*c*. Structural and electronic analysis were performed on these competing structure types to determine that the monoclinic structure is energetically favorable at room temperature. Integrated COHP values, normalized to the overall % contribution, show no significant difference between the two structure types. However, the DOS for the monoclinic structure shows the Fermi level lies in a pseudogap but that for the orthorhombic form does not.

4.2 Introduction

Polar intermetallic compounds with the general formula $A_2T_2X_1$ (A= electropositive metal, T= transition metal, X= post transition metal) have been studied due to their varying structure types and bonding characteristics which can lead to different physical properties.[1] There are several common structures types for compounds with this general formula including the orthorhombic W_2CoB_2-type, with more than 60 representatives,[2-3] and the (crystal class) Mo_2B_2Fe-type structure, which has over 200 representatives.[4] A structure type that does not contain as many representatives is the HT-Pr_2Co_2Al-type structure, evidenced initially by the dimorphic Pr_2Co_2Al.[5]

Throughout these structure types the polyanionic networks behave differently. In Ca_2Pt_2Cd the Pt and Cd atoms create infinite planar networks of $[Pt_2Cd]^{4-}$, with the Ca atoms between the planes, whereas in the Ca_2Pt_2In the Pt and In atoms create a complex three-dimensional network.[6] Certain examples of $A_2T_2X_1$ compounds, for example Ca_2T_2Ge (T=Pt, Pd), have shown differences in structure from Pd to Pt, although the structures are closely related. Ca_2Pd_2Ge crystallizes in an ordered (crystal class) Zr_2Al_3-type, whereas Ca_2Pt_2Ge crystallizes in the Pr_2Co_2Al-type.[1] A significant difference in these structures is that there is no pairwise distortion of the linear chains of Pd atoms in Ca_2Pd_2Ge, but the corresponding chains are pairwise distorted in Ca_2Pt_2Ge.[2]

Ca_2T_2X (T = Pd, Pt; X = Ag, Mg, Ga) were studied in an effort to analyze the impact of the electronegativity and valence electron count on the structure and bonding of $A_2T_2X_1$ phases. In this study the compounds Ca_2T_2Ag and Ca_2T_2Mg (T= Pd, Pt) crystalized in the orthorhombic W_2B_2Co-type structure. The Ga containing phases could not be synthesized as a pure product, but occurred alongside $Ca_3Pd_2Ga_2$, whereas Ca_2Pt_2Ga crystals were only obtained from a 6:3:1 loading of Ca:Pt:Ga.[2] In the current report Ca_2Pd_2Ga was first identified as a byproduct in the synthesis of Ca_2Pd_3Ga, and then a stoichiometric sample was prepared and crystallized in the orthorhombic space group *Cmca*. Electronic structure calculations were performed to determine the electronic stabilities of these two competing structure types.

4.3 Experimental

4.3.1 Synthesis

Orthorhombic Ca_2Pd_2Ga was obtained by combining mixtures of Ca pieces (99.99%, Sigma-Alrich), Pd pieces (99.999%, Ames Laboratory), and Ga ingots (99.99%, Alfa Aesar). Samples of total weight ca. 300 mg were weighed in a N_2-filled glovebox with < 0.1 ppm

moisture and sealed in tantalum tubes by arc-melting under an argon atmosphere. The tantalum tubes were placed in evacuated silica jackets to prevent oxidation during the heating process. The silica jackets were then placed in a programmable tube furnace and heated to 1050 ^{0}C at a rate of 150 ^{0}C/hour. The samples were held at this temperature for three hours and then cooled to 850 ^{0}C at a rate of 50 ^{0}C/hour. Samples were then annealed for 5 days and then cooled to room temperature at 50 ^{0}C/hour. The orthorhombic structure crystals were obtained from stoichiometric loadings of Ca_2Pd_2Ga. A previous study, with the synthetic method of heating to 1000 ^{0}C for two hours and then cooling to 870 ^{0}C at a rate of 6 ^{0}C/hr and annealing at this temperature for 48 to 72 hours following which the furnace was turned off, yielded a biphasic product of monoclinic Ca_2Pd_2Ga and Ca_3Pd_2Ga.[2]

4.3.2 Powder X-Ray Diffraction

Synthesized samples were characterized by powder X-Ray diffraction to determine the phase purity. The samples were measured on a STOE WinXPOW instrument using Cu K_α radiation (λ=1.540598 Å). Samples were ground using an agate mortar and pestle and sifted through a US standard sieve with hole sizes of 150 microns. The ground powders were placed between two acetate films using a thin layer of vacuum grease and then placed in the holder. Scattered intensities, ranging from 3^0 to 130^0 in 2Θ, were measured using a scintillation detector with a step size in 2Θ of 0.03^0 in step scan mode. Analysis of powder patterns was performed using *Powdercell*[7] by overlaying the theoretical powder patterns on the experimental patterns to determine phase identity and purity.

4.3.3 Single Crystal X-Ray Diffraction

Single crystals were picked out of the bulk sample and mounted on the tips of thin glass fibers. Intensity data were collected at room temperature on a Bruker SMART APEX II

diffractometer using graphite monochromated Mo K_α radiation (λ=0.71073 Å). Data collection strategies were determined by an algorithm in the program COSMO in the APEX II software package.[8] Additional crystals were measured with a pre-set of scans varying the phi angle from 0^0-300^0 in 60^0 increments with a sweep of 180^0 in 0.5^0 steps and an exposure time of 20 seconds/frame. Indexing and integration of data was performed with the program SAINT in the APEX II package.[8-9] Empirical absorption corrections were applied using the SADABS program.[8] Crystal structures were solved using *SHELXL* direct methods and refined by full-matrix least squares on F^2.[10] Final structure solutions were refined using anisotropic displacement parameters on all atoms. Crystal structure figures were produced using the program Diamond.[11]

4.3.4 Electronic Structure Calculations

The Stuttgart *Tight-Binding, Linear-Muffin-Tin Orbital* program with the *Atomic Sphere Approximation* (TB-LMTO-ASA)[12] was utilized to calculate density of states (DOS) and crystal orbital Hamilton population (COHP) curves to analyze bonding and electronic stability of the competing Ca_2Pd_2Ga structure types. This approximation uses overlapping Wigner-Seitz (WS) spheres surrounding each atom so that spherical basis functions, i.e., atomic orbital (AO)-like wavefunctions, are used to fill space. The radii of the WS spheres for each atom, in the orthorhombic and monoclinic structures respectively, are: Ca 3.8418 Å; 3.8457 Å, Pd 2.7189 Å; 2.6833 Å, and Ga 2.7757 Å; 2.7393. The total amount of overlap was 7.69% and 7.57% respectively, for the orthorhombic and monoclinic structures. Empty spheres were not required for either structure to attain 100% space filling of the unit cells. The von Barth-Hedin formulation within the local density approximation (LDA) was used to treat the exchange-correlation.[13] A scalar relativistic approximation was used to take into account all

relativistic effects except spin-orbit coupling.[14] The basis sets included 4*s*/(4*p*)/3*d* for Ca, 5*s*/5*p*/4*d*/(4*f*) for Pd, and 4*s*/4*p*/(4*d*) for Ga (parentheses indicate down-folded orbitals). Reciprocal space integrations were performed using *k*-point meshes of 657 for orthorhombic Ca_2Pd_2Ga and 1098 for monoclinic Ca_2Pd_2Ga in the corresponding irreducible wedges of the first Brillouin zones.

4.4 Results

4.4.1 Phase Analysis

The X-ray powder diffraction pattern measured for the product containing Ca_2Pd_2Ga (see **Figure 4.4.1**) shows that the orthorhombic ternary compound is indeed a major phase. However, there are two peaks at $2\Theta = 19.2^0$ and 41.3^0 that are not indexed, in the *Cmca* structure and these peaks do not correlate with any diffraction peaks expected for any of the known binary or ternary compounds in this system. The synthetic procedure yielding the orthorhombic structure is reproducible, and a powder X-Ray pattern of another sample can be seen in Figure S1.

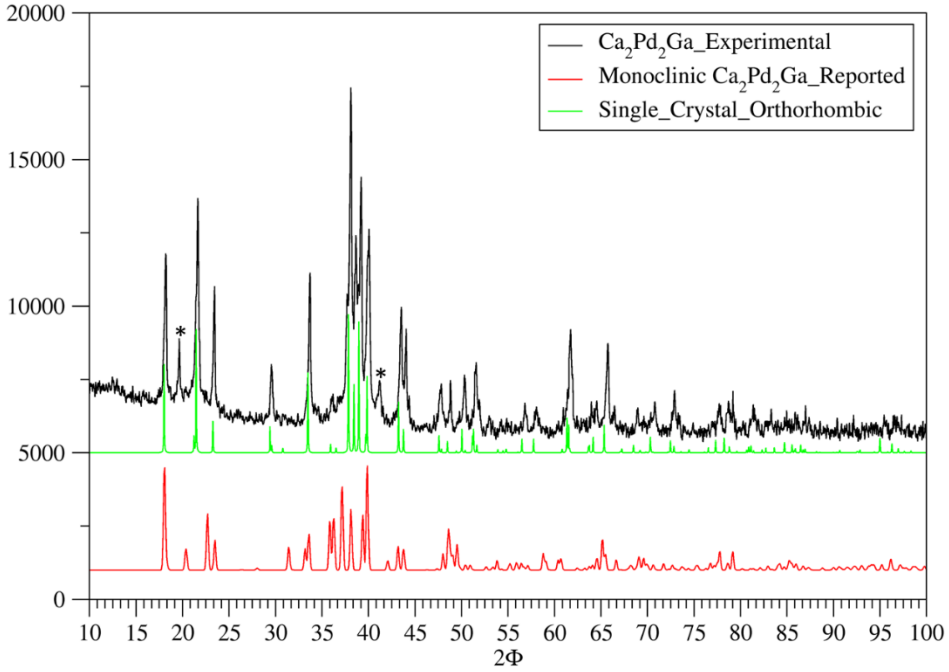

Figure 4.4.1. Powder X-Ray pattern of loaded Ca_2Pd_2Ga. * = non-indexed peaks. Red line is the powder pattern for previously reported monoclinic structure indicating very little if any is present in experimental sample.

4.4.2 Structure Determination

Several crystals were picked from the bulk sample and tested on a Bruker SMART APEX-II instrument. The best four crystals were run for a full data collection and the results can be seen in **Table 4.4.1** and Table S1 along with atomic coordinates and anisotropic displacement parameters found in Tale S2. The structure has linear chains of Pd atoms along the *a*-direction. Each Pd atom has a coordination number (CN) of 10 with 2 Pd, 2Ga, and 6 Ca nearest neighbors. The Ga atoms sit in an environment of CN 12 with 8 Ca and 4 Pd and no Ga–Ga interactions, the shortest of which is is 4.791 Å. Each Ga atom is bonded to 4 Pd atoms and form Pd–Ga–Pd interactions that connect the linear chains of Pd. Ca atoms have a CN 15 with interactions with 4 Ga, 6 Pd, and 5 Ca atoms.

Table 4.4.1. Crystallographic information for Ca_2Pd_2Ga. Peak residual electron density is 1.75 Å from Ga and the hole is 0.48 Å from Pd.

Sample	Ca_2Pd_2Ga
Space Group	*Cmca*
Unit Cell	$a = 5.7893(4)$
	$b = 9.8162(8)$
	$c = 7.6183(7)$
Volume	432.94(6)
Z	4
Absorption Coefficient	16.538 mm^{-1}
Index Ranges	$-13 \leq h \leq 13, -22 \leq k \leq 23, -18 \leq l \leq 18$
Reflections Collected	10381
Independent Reflections	1651 [R(int) = 0.0446]
Theta range for data collection	4.152 to 50.680°
Refinement method	Full-matrix least-squares on F^2
Data/restraints/parameters	1651/0/16
Goodness-of-fit on F^2	0.969
Final R indices [$I > 2\sigma(I)$]	$R1 = 0.0282$, $wR2 = 0.0581$
R indices (all data)	$R1 = 0.0455$, $wR2 = 0.0638$
Largest diff. peak and hole	1.581 and –2.259 eÅ^{-3}

4.4.3 Structure Comparison

The space group C/2c is a maximal non-isomorphic subgroup of Cmca, retaining eight of the sixteen symmetry operations found in Cmca. The symmetry operations that are lost in moving from Cmca to C2/c for the $(0,0,0)^+$ set are: the two-fold screw-axes, the *b* glide plane x,y,¼, and the mirror plane (0,y,z). The symmetry operations lost for the $(½, ½, 0)^+$ set are: the two-fold rotation about ¼,y,¼, two-fold screw axis about x,¼,0, the *a* glide plane x,y,¼, and the *b* glide plane ¼,y,z.

Previously reported Ca_2Pd_2Ga crystallizes in the monoclinic space group $C2/c$ in the $AlCoPr_2$ structure type.[2] This monoclinic structure also contains Pd chains, although they are stacked in staggered layers compared to the Cmca structure, where all Pd chains are parallel to a single direction (see **Figure 4.4.2**). The orthorhombic structure contains puckered Pd_2Ga "sheets" that are separated by layers of 4 Ca atoms and stacked along the *b* direction (see Figure

S2). The monoclinic structure does not contain this stacking however, looking down the *c* axis shows Pd−Pd dimers, connected by Ga atoms, creating Pd_2Ga chains surrounded by 8 Ca atoms along the *c* direction (see Figure S3). The coordination environments around each atom are similar in the two structures, although the Pd–Pd and Pd–Ga interactions are split into two inequivalent distances in the monoclinic structure. The Pd–Pd distances along the chains in the monoclinic structure are split into alternating shorter (2.790 Å) and longer (2.939 Å) distances compared to the orthorhombic structure which contains only one Pd−Pd distance (2.895 Å) in the linear chains. On the other hand, both the Pd–Ga distances are longer in the monoclinic phase (2.534 Å, 2.572 Å) than in the orthorhombic phase (2.525 Å).

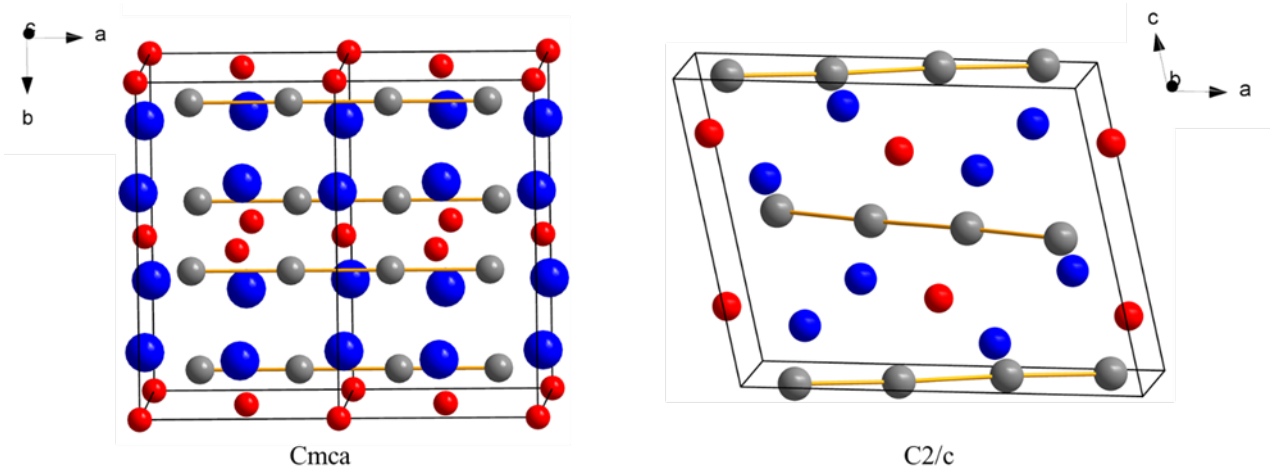

Figure 4.4.2. Unit cell drawings emphasizing the direction of the Pd–Pd chains in the Cmca, doubled unit cell drawn (left) and C2/c (right) structures. Blue, grey, and red atoms are Ca, Pd, and Ga respectively.

There are several different structures that many 221 compounds have been found to crystalize in. These structure types include: a ternary ordered variant of the binary Zr_2Al_3, the orthorhombic W_2CoB_2-type, the Mo_2FeB_2-type, the monoclinic Pr_2Co_2Al-type, and the Mn_2AlB_2-type. The synthesized Ca_2Pd_2Ga, as presented in this work, crystalizes in the La_2Ni_3 structure type.[1-6,15-16] A comparison of these structures shows that the most electronegative element forms linear chains in some and dumbells in others. The Mo_2FeB_2-type structure has

dumbells of B atoms that stack along the *c* direction. There are chains in the cases of the Zr_2Al_3, Pr_2Co_2Al, and W_2CoB_2-type structures however, these chains vary from structure to structure. Ca_2Pd_2Ge, which crystallizes in the ternary ordered variant of Zr_2Al_3, contains chains of Pd atoms that stack in alternating directions and have the same bond distance in between all Pd atoms, however, they are not truly linear with a bond angle of 178.33^0 instead of 180^0. Monoclinic Ca_2Pd_2Ga also contains stackings of alternating linear Pd chains but unlike the Zr_2Al_3 structure type the bond angles are all 180^0 but there are two different bond distances between the Pd atoms. The chains that are present in Ca_2Pt_2Cd, which crystalizes in the W_2CoB_2-type structure, are linear and all aligned parallel to the *b* axis but the chains have two different bond lengths between the Pt atoms (3.183 Å and 2.659 Å).[6] The chains of Pd atoms in the orthorhombic Ca_2Pd_2Ga are all parallel to the same direction and all have equal Pd−Pd bond distances. **Figure 4.4.3** shows these different features. The layering in the W_2CoB_2 structure type can also be seen in **Figure 4.4.3**. The Pt−Cd interactions form 2 dimensional sheets of Pd_2Cd separated by a puckered layer of Ca atoms. This sheet is distorted in the La_2Ni_3 structure type that the Cmca Ca_2Pd_2Ga adopts.

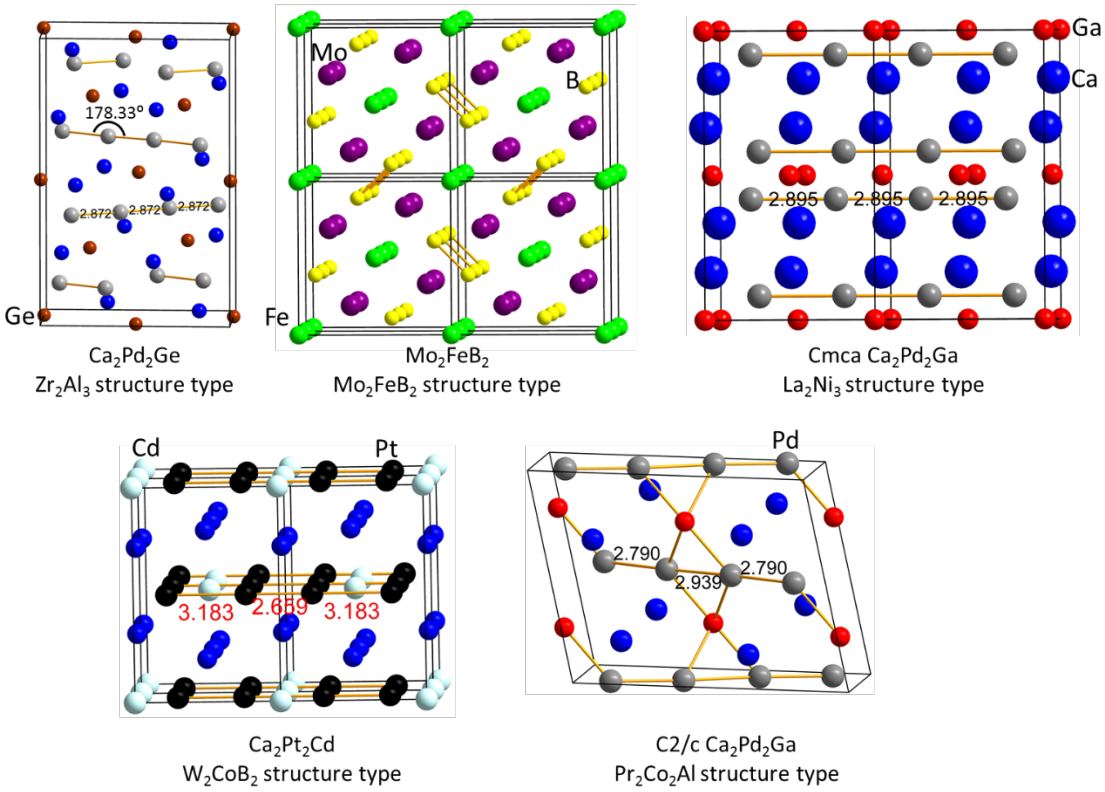

Figure 4.4.3. Unit cells displaying features of various 221 structure types.

4.4.4 Electronic Structure Calculations

To shed light on the bonding characteristics in both structure types, DOS and COHP curves were calculated and analyzed. The DOS of the *Cmca* structure shows that the Ga 4s electrons are dominant from ~ −8 to −6.75 eV. The Pd *d* states are the main contributors from ~ −4 to −2 eV. The *d* band is split into two main regions at ~ −3 eV. The Ca virtual *d* states dominate the DOS above the Fermi level. The calculated DOS (see **Figure 4.4.4**) shows a significant number of states at the Fermi level, which, according to the COHP curves, show nonbonding characteristics for the Pd−Pd, Pd−Ga, and Ca−Ca interactions and significant bonding characteristics for the Pd−Ca and Ca−Ga contacts. These results are rather typical for many polar intermetallics. In comparison, the DOS calculated for the monoclinic Ca_2Pd_2Ga (see **Figure 4.4.5**) shows a pseudogap at the Fermi level. All pairwise interactions are nonbonding at the Fermi level in the COHP curves. The two DOS curves also show that the

Pd 4*d* band is wider in the monoclinic structure than in the orthorhombic structure. Moreover, at ~ 6.5 and ~ 5 eV below the Fermi level, the states for the orthorhombic structure abruptly disappear and then appear again compared to the more gradual disappearance and appearance of states in the monoclinic structure. This sudden appearance and disappearance is due to the distinct two-dimensional layering that is found in the orthorhombic compound and not present in the monoclinic structure.

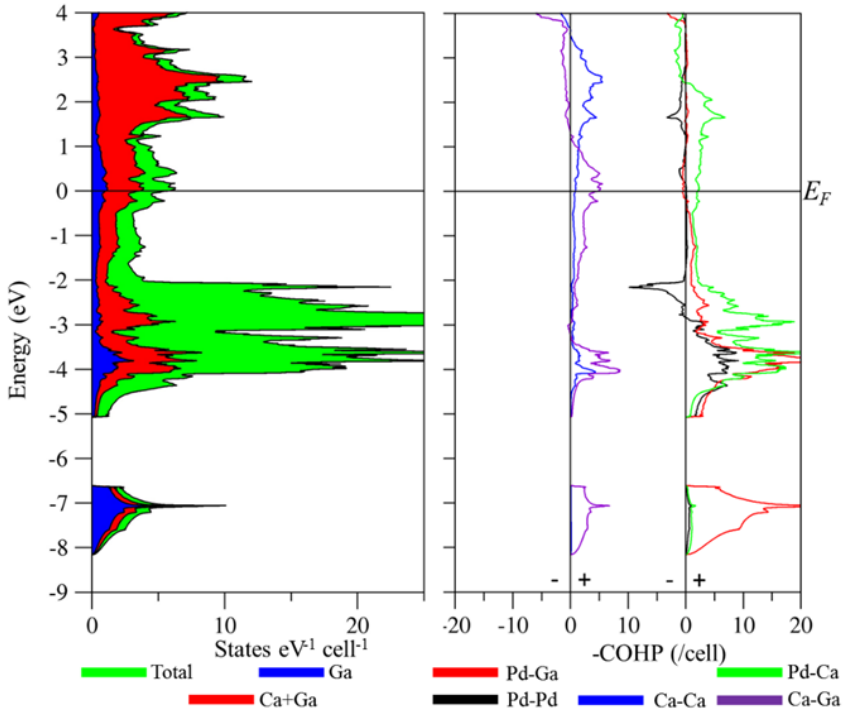

Figure 4.4.4. DOS (left) and −COHP (right) for Cmca Ca_2Pd_2Ga. −/+ indicate anti-bonding/bonding values of −COHP curves.

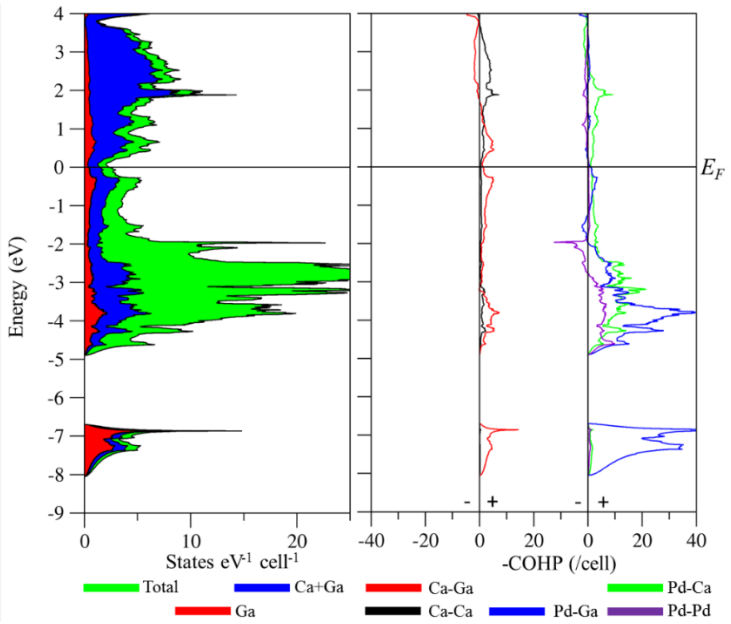

Figure 4.4.5. DOS (left) and −COHP (right) for C2/c Ca_2Pd_2Ga. −/+ indicate anti-bonding/bonding values of −COHP curves.

The COHP curve can be integrated (ICOHP) to get a sense of the overall contribution of each pairwise interactions in the competing structures. The percent contributions to the total ICOHP can been seen in **Table 4.2.2**. Each pairwise interaction contributes roughly the same in both structure types. In the monoclinic structure, the Pd chains have alternating long (2.939 Å) and short (2.790 Å) bonds with the shorter contact having an ICOHP value twice as large as the longer one, indicating much stronger interactions compared to the longer distance. Even with the alternating distances the Pd–Pd interactions in the monoclinic structure contribute comparably to the Pd–Pd interactions in the orthorhombic structure.

Table 4.4.2. Comparison of Cmca and C2/c COHP interactions in Ca_2Pd_2Ga.

		Cmca			C2/c		
Bonds	#/f.u.	Distance	–ICOHP (eV)	% ICOHP	Distance	–ICOHP (eV)	% ICOHP
Pd–Pd	2	2.899	1.039	9.44	2.790, 2.939	1.531, 0.745	10.25
Pd–Ga	4	2.531	2.053	37.34	2.534, 2.572	2.017, 1.885	35.14
Pd–Ca	12	3.061-3.114	0.555-0.613	33.77	3.051-3.127	0.589-0.649	34.35
Ca–Ga	8	3.382-3.477	0.488-0.386	15.62	3.384-3.403	0.354-0.439	16.49
Ca–Ca	5	3.539-3.731	0.001-0.013	3.83	3.617-3.675	0.166-0.171	3.78

The band structures presented in **Figure 4.4.6** also show some distinct differences between the two structure types. The band structure of the orthorhombic structure shows that the bands crossing E_F have a steep slope. However, near the M point in the band structure of the monoclinic structure, there is a doubly degenerate band that is very flat. Further analysis of this doubly degenerate band indicates that the main contributions to these two bands are 30% Ca 3*d* followed by 25% Pd 4*d*. The remaining contributions are distributed evenly between Pd 5*s*, 5*p*, Ca 4*s*, 4*p*, and Ga 4*p*. Ga 4*s* and 4*d* contribute less than 4% each to the overall bands.

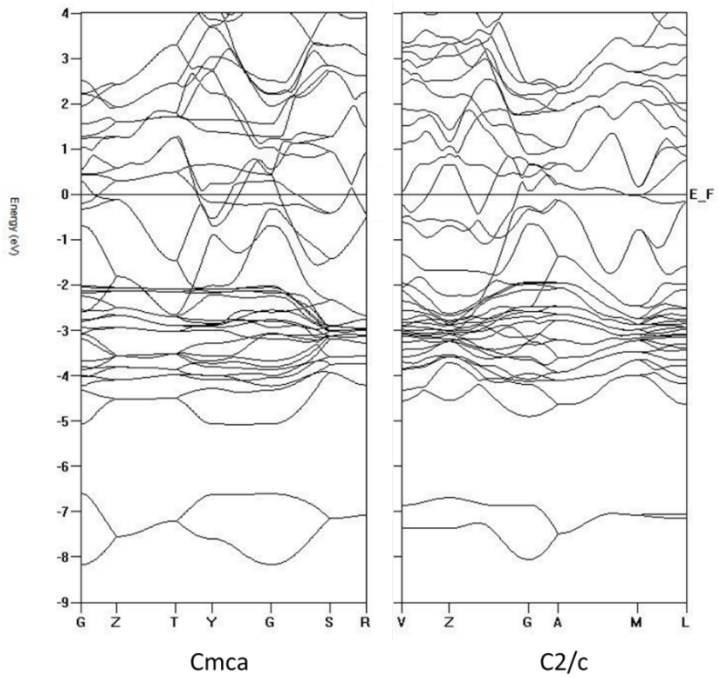

Figure 4.4.6. Band structures for Cmca (left) and C2/c (right) structures of Ca_2Pd_2Ga.

4.5 Conclusions

The compound Ca_2Pd_2Ga was reproducibly synthesized and analyzed by single crystal and powder X-Ray diffraction in an orthorhombic crystal structure, but it had been reported previously to crystallize as part of a diphasic mixture with $Ca_3Pd_2Ga_2$ in a monoclinic, $AlCoPr_2$-type crystal structure. The $Ca_3Pd_2Ga_2$ byproduct crystalizes in the orthorhombic

$Y_3Rh_2Si_2$-structure type which contains similar linear chains of staggered Pd−Pd dumbells connected by Ga atoms as the C2/c Ca_2Pd_2Ga structure. Electronic structure calculations including DOS and COHP curves were performed to gain an understanding of the energetics and bonding characteristics of the competing structure types. The electronic structure calculations show a pseudogap at the DOS of the monoclinic structure as well as optimized bonding at the Fermi level in the COHP.

4.6 Acknowledgements

A. Toombs acknowledges S. Thimmaiah for many discussions on the crystallography and refinements for this work along with J. Pham for support and answering several questions on crystal chemistry. This research was supported by the Office of the Basic Energy Sciences, Materials Sciences Division, U.S. Department of Energy (DOE). The Ames Laboratory is operated by Iowa State University under Contract No. DE-AC02-07C. Computations were performed on the CRUNCH cluster supported by Iowa State University Computation Advisory Committee under Project No. 202-17-10-08-0005. The authors declare no conflict of interest.

4.7 Supporting Information

Supporting information for this chapter can be found in APPENDIX B.

4.8 References

1. Doverbatt, I.; Ponou, S.; Zhang, Y.; Lidin, S.; Miller, G.J. Linear Metal Chains in Ca_2M_2X (M=Pd, Pt; X = Al, Ge): Origin of the Pairwise Distortion and Its Role in the Structure Stability. *Chem. Mater.* **2015**, *27,* 304-315.

2. Ponou, S.; Miller, G.J. Synergistic geometrical and electronic features in the intermetallic phases Ca2 Ag M2, Ca2 Mg M2, and Ca2 Ga M2 (M = Pd, Pt). *Zeitschrift fuer Anorganische und Allegeine Chemie*, **2015**, *641*, 1069-1079.

3. Morozki, A.V.; Isnard, O.; Nirmala, R.; Malik, S.K. Mo_2NiB_2-type {Gd, Tb, $Dy)_2Ni_{2.35}Si_{0.65}$ and La_2Ni_3-type {Dy, Ho}$_2Ni_{2.5}Si_{0.5}$ compounds: Crystal Structure and magnetic properties. *Journal of Solid State Chemistry*, **2015**, *225,* 368-377.

4. Johnscher, M.; Pöttgen, R. Ca_2Pd_2Cd with W_2B_2Co-type Structure, *Z. Naturforsch.* **2013**, *68b,* 95-98.

5. Muts, I.R.; Zaremba, V.I.; Rodewald, U.C.; Hermes, W.; Pöttgen, R. Ca_2Pd_2In and Ca_2Pt_2In with Monoclinic HT-Pr_2Co_2Al Type Structure. *Z. Anorg. Allg. Chem.* **2007**, *633,* 2725-2729.

6. Samal, S.L.; Corbett, J.D. Synthesis, Structure, and Bonding Analysis of the Polar Intermetallic Phase Ca_2Pt_2Cd, *Z. Anorg. Allg. Chem.* **2012**, *638(12-13),* 1963-1969.

7. PowderCell, version 2.3; Federal Institute for Materials Research and Testing: Berlin, Germany, 2000.

8. *APEX-II,* Bruker AXS Inc., Madison, WI, USA, **2013**.

9. *SAINT-V8.27,* Bruker AXS Inc., Madison, WI, USA, **2013**.

10. *SHELXTL-v2008/4,* Bruker AXS Inc., Madiosn WI, USA, **2013**.

11. K. Brandenburn, *Diamond*, version 3.2, *Crystal Impact GbR,* Bonn, Germany, **2001**.

*12. Jepsen, O.; Andersen, O.K. TB-LMTO, version 47; Max-Planck-Institut für Festkörperforshcung: Stuttgart, Germany, **2000**.*

*13. Von Barth, U.; Hedin, L. Local exchange-correlation potential for the spin-polarized case. J. Phys. C **1972**, 5, 1629.*

*14. Koelling, D.D.; Harmon, B.N. A technique for relative spin-polarized calculations. J. Phys. C **1977**, 10, 3107–3114.*

15. Stegemann, F.; Benndorf, C.; Touzani, R.S.; Fokwa, B.; Janka, O. Experimental and theoretical investigations of the polar ntermetallics $SrPt_3Al_2$ and Sr_2Pd_2Al. *Journal of Solid State Chemistry*, **2016**, *242*¸143-150.

16. Marushina, E.V.; Kaczorowski, D.; Murashova, E.V.; Kurenbaeva, Zh.M.; Gribanov, A.V. Crystal structure and ustable valence in a novel intermetallic phase Ce_2Ru_2Al, *Journal of Alloys and Compounds*, **2015**, *650*, 654-657.

CHAPTER 5. $Gd(Co_{1-x}Ga_x)_2$: SYNTHESIS, CYSTAL STRUCTURES, AND INVESTIGATION OF STRUCTURAL TRANSFORMATION AND MAGNETIC PROPERTIES

Modified from a publication in the *Journal of Solid State Chemsitry*
(Journal of Solid State Chemsitry, **2018**, *264,* 68-76)
DOI: 10.1016/j.jssc.2018.05.009

Fang Yuan[1], Asa Toombs,[2] Gordon J. Miller[2], and Yurij Mozharivskyj[1*]

[1]Department of Chemistry and Chemical Biology, Brockhouse Institute of Materials Research, McMaster University, 1280 Main Street West, Hamilton, Ontario L8S 4M1, Canada

[2]Department of Chemistry, Iowa State University, Ames, Iowa 50011-3111 and Ames Laboratory, U.S. Department of Energy, Ames IA 50011-3111, United States.

5.1 Abstract

$Gd(Co_{1-x}Ga_x)_2$ (x = 0, 1/6, 1/3, 1/2, 2/3, 5/6, and 1) phases were synthesized by arc melting the constituent elements and subsequent annealing. The samples were characterized by powder and single crystal X-ray diffraction, magnetic measurements, and electronic structure calculations. An interesting structural sequence was obtained: cubic $MgCu_2$-type structure for x = 0 and 1/6; $MgZn_2$-type structure for x = 1/3; orthorhombic SrMgSi-type structure for x = ½; orthorhombic $CeCu_2$-type structure for x = 2/3; hexagonal AlB_2-type structure for x = 5/6 and 1. Tight-binding linear-muffin-tin orbital (TB-LMTO) calculations were performed on $GdCo_2$, GdCoGa, and $GdGa_2$ to trace the origin of their structural transformations, which appear to be driven by the changes in the valence electron count (VEC). In addition, some conclusions of these fully stoichiometric compounds were obtained from the rigid band model. $GdGa_2$ (x = 1) is antiferromagnetic, while the other ones are either ferrimagnetic or ferromagnetic. T_C of $Gd(Co_{1-x}Ga_x)_2$ decreases monotonically with the increasing Ga content, suggesting that promising room temperature (RT) magnetocaloric materials could be obtained between x = 1/6 and x = 1/3.

5.2 Introduction

The environmental awareness, which matured in the past few decades, increased our efforts towards development of energy-efficient and environment-friendly refrigeration techniques. Discovery of giant magnetocaloric effect (GMCE) in $Gd_5Si_2Ge_2$ showed that magnetic refrigeration can be a potential alternative for the conventional vapor-cycle refrigeration.[1] In the case of GMCE, there is a first-order magnetic transition; the total entropy change, which is discontinuous at the transition points, contains both the structural and magnetic entropy contributions, and thus is significantly enhanced when compared to a conventional MCE. In this light, good candidates for magnetic refrigeration are materials with a GMCE. Such compounds should contain magnetically active rare earth or transition metals or both. For example, Laves phases with a general formula $RECo_2$ (*RE* = rare earth) adopt a cubic $MgCu_2$-type structure,[2] but exhibit different magnetic properties depending on *RE* due to the inherent instability of Co sublattice magnetism. For *RE* = Dy, Ho, and Er, a nonmagnetic Co sublattice is turned into ferromagnetic by the *RE* molecular field upon cooling, i.e. a metamagnetic transition is induced by the itinerant electrons.[3] The itinerant electron metamagnetism (IEM) causes not only a first-order magnetic transition but also GMCE in $RECo_2$ (*RE* = Dy, Ho, and Er).[4,5] On the other hand, a conventional MCE with a second-order magnetic transition is observed in other $RECo_2$ compounds.

For practical applications, magnetocaloric materials with transitions around room temperature are the most promising candidates in terms of wide-spread applications and economic benefits. However, most of $RECo_2$ compounds have transitions at lower temperatures. Curie temperature (T_C) of $GdCo_2$ peaks at 400 K for *RE* = Gd and drops rapidly when *RE* moves away from Gd on both sides of periodic table of elements.[3] Replacing Co

with some nonmagnetic elements in $GdCo_2$ may allow adjusting T_C to room temperature. In this work, nonmagnetic Ga was chosen to substitute for Co. Previously, a few structures have been reported in $Gd(Co_{1-x}Ga_x)_2$ system: 1) cubic $MgCu_2$-type $GdCo_2$ ($Fd\bar{3}m$)[6]; 2) hexagonal $MgZn_2$-type structure for $GdCo_{1.333}Ga_{0.667}$ ($P6_3/mmc$);[7] 3) orthorhombic SrMgSi-type GdCoGa (*Pnma*)[8]; 4) orthorhombic $CeCu_2$-type $GdCo_{0.67}Ga_{1.33}$ (*Imma*)[9]; and 5) hexagonal AlB_2-type $GdGa_2$ ($P6/mmm$)[10], suggesting that the structural types change regularly with an x interval of 1/6 or 1/3 for $Gd(Co_{1-x}Ga_x)_2$. To explore this system in greater details, $Gd(Co_{1-x}Ga_x)_2$ (x = 0, 1/6, 1/3, 1/2, 2/3, 5/6, and 1) alloys were prepared in this work.

Structural transitions can be driven by changes in the valence electron count (VEC) and/or geometric parameters. In the case of the $Gd(Co_{1-x}Ga_x)_2$ system, Ga has an atomic size similar to that of Co (r_{Co} = 1.25 Å, r_{Ga} = 1.26 Å),[11] which minimizes the geometric effects. Therefore, the VEC could be a key factor in controlling the structures of $Gd(Co_{1-x}Ga_x)_2$ system. In it worth mentioning that the structural transformation in the $GdCo_2$-$GdAl_2$ system were rationalized in terms of the VEC and Fermi surface features.[12] Since Ga and Al are isovalent and have similar atomic sizes (r_{Al} = 1.25 Å, r_{Ga} = 1.26 Å),[11] some of the general rules developed for $GdCo_2$-$GdAl_2$ may be applicable to $GdCo_2$-$GdGa_2$.

5.3 Experimental

5.3.1 Synthesis

The starting materials are Gd (99.99 wt.%, distilled grade, Metal Rare-earth Limited, China), Co (99.98 wt.%, Alfa Aesar) and Ga (99.999 wt.%, Alfa Aesar) pieces. Alloys with the $Gd(Co_{1-x}Ga_{x)2}$ (x = 0, 1/6, 1/3, 1/2, 2/3, 5/6, and 1) stoichiometries and a total mass of ~1 g were arc-melted 3 times to ensure homogeneity. During remelting process, the samples were turned over as fast as possible to prevent sample cracking during cooling. The cast alloy buttons

were split, and then one-half of each button was wrapped in Ta foil, sealed in evacuated silica tubes, heated to 850°C at 100°C/hour, annealed at this temperature for 7 days and subsequently quenched in cold water.

5.3.2 X-Ray Analysis

Room-temperature phase analyses of the cast and annealed $Gd(Co_{1-x}Ga_x)_2$ (x = 0, 1/6, 1/3, 1/2, 2/3, 5/6, and 1) samples were performed on a PANalytical X'Pert Pro diffractometer with a linear X'Celerator detector. The X-ray diffraction patterns were collected with Co$K\alpha$ radiation to eliminate the Gd fluorescene associated with Cu$K\alpha$ radiation. More than one crystalline phase was observed in most of the cast $Gd(Co_{1-x}Ga_x)_2$ (x = 0, 1/6, 1/3, 1/2, 2/3, 5/6, and 1) alloys. However, samples with high purity could be obtained by annealing at 850°C for 7 days. The annealed alloys with x = 0 and 1/6 yielded a cubic $MgCu_2$-type phase. X-ray powder diffraction of the sample with x = 1/3 suggested a hexagonal $MgZn_2$-type phase ($P6_3/mmc$). The GdCoGa alloy contains an orthorhombic SrMgSi-type phase and some $MgZn_2$-type impurities. The annealed alloy with x = 2/3 adopted an orthorhombic $CeCu_2$-type structure. A hexagonal AlB_2-type phase ($P6/mmm$) was formed in the annealed alloys with x = 5/6 and 1. The unit cell dimensions derived from the Rietveld refinement (*Rietic*a program)[13] for the annealed samples are summarized in **Table 5.3.1**. Standard deviation (SD) for x = 1/2 and 2/3 are larger than others phases, which could be related to the impurities. Impurities for x = 1/2 was confirmed to be $MgZn_2$-type phases, while no detectable impurities were observed for x = 2/3 via powder X-ray diffraction.

Table 5.3.1. Phase analyses from the Rietveld refinement of X-ray powder diffraction for annealed $Gd(Co_{1-x}Ga_{x)2}$ (x = 0, 1/6, 1/3, 1/2, 2/3, 5/6, and 1)

Sample	Str. type	Sp. group	a, Å	b, Å	c, Å	V, Å^3
$GdCo_2$	$MgCu_2$-type	$Fd\bar{3}m$	7.25618(2)	7.25618(2)	7.25618(2)	382.054(2)
$GdCo_{1.67}Ga_{0.33}$	$MgCu_2$-type	$Fd\bar{3}m$	7.33059(3)	7.33059(3)	7.33059(3)	393.928(3)
$GdCo_{1.33}Ga_{0.67}$	$MgZn_2$-type	$P6_3/mmc$	5.26670(3)	5.26670(3)	8.50070(8)	204.203(3)
GdCoGa	SrMgSi-type	*Pnma*	7.1522(2)	4.4339(2)	7.0003(2)	222.00(1)
$GdCo_{0.67}Ga_{1.33}$	$CeCu_2$-type	*Imma*	4.3684(1)	7.0967(2)	7.4914(2)	232.24(1)
$GdCo_{0.33}Ga_{1.67}$	AlB_2-type	*P6/mmm*	4.37694(7)	4.37694(7)	3.65559(9)	60.650(2)
$GdGa_2$	AlB_2-type	*P6/mmm*	4.22011(6)	4.22011(6)	4.13423(9)	63.764(2)

Suitable single crystals were extracted from the annealed $Gd(Co_{1-x}Ga_{x)2}$ (x = 0, 1/6, 1/3, 1/2, 2/3, 5/6, and 1) alloys. Single crystal X-ray diffraction data were collected on a STOE IPDS II diffractometer with Mo$K\alpha$ radiation at room temperature. Numerical absorption corrections were based on the crystal shapes that were originally derived from optical face indexing but later optimized against equivalent reflections using the STOE X-shape software. Crystal structures were refined using the SHELXL program.[14] Crystallographic data and refinement results are summarized in **Table 5.3.2 and 5.3.3.** The structures obtained from single crystal solutions agree well with the powder X-ray diffraction results.

Table 5.3.2. Crystallographic data and refinement results for Gd $(Co_{1-x}Ga_x)_2$ (x =0, 1/6, 1/3, 1/2, 2/3, 5/6, and 1) (MoK_α radiation, 293 K).

$Gd(Co_{1-x}Ga_x)_2$	x = 0	x = 1/6	x = 1/3	x = 1/2	x = 2/3	x = 5/6	x = 1
Scan mode				**Omega**			
Structure type	$MgCu_2$-type	$MgCu_2$-type	$MgZn_2$-type	SrMgSi -type	$CeCu_2$-type	AlB_2-type	AlB_2-type
Space group	$Fd\bar{3}m$	$Fd\bar{3}m$	$P6_3/mmc$	*Pnma*	*Imma*	*P6/mmm*	*P6/mmm*
***a* (Å)**	7.2518(8)	7.3174(8)	5.2593(7)	7.114(1)	4.3649(9)	4.3719(6)	4.2143(6)
b (Å)	–	–	–	4.4017(9)	7.090(1)	–	–
***c* (Å)**	–	–	8.490(2)	7.025(1)	7.482(2)	3.6441(7)	4.1319(8)
Volume ($Å^3$)	381.36(7)	391.81(7)	203.37(6)	219.98(8)	231.54(8)	60.32(2)	63.55(2)
ρ_{calc} (g/cm^3)	9.583	9.449	9.221	8.632	8.304	8.070	7.752
Z	8	8	4	4	4	1	1
Index ranges	$-9 \le h \le 9$ $-9 \le k \le 8$ $-9 \le l \le 9$	$-9 \le h \le 9$ $-8 \le k \le 9$ $-9 \le l \le 9$	$-7 \le h \le 7$ $-7 \le k \le 7$ $-11 \le l \le 11$	$-8 \le h \le 11$ $-6 \le k \le 6$ $-11 \le l \le 11$	$-5 \le h \le 5$ $-8 \le k \le 9$ $-10 \le l \le 10$	$-5 \le h \le 5$ $-5 \le k \le 5$ $-4 \le l \le 4$	$-6 \le h \le 5$ $-6 \le k \le 6$ $-6 \le l \le 6$
2θ range (°)	9.74 to 57.38	9.66 to 59.80	8.94 to 58.18	8.16 to 72.48	7.92 to 58.08	10.78 to 57.52	9.88 to 57.62
Meas. Refl.	963	1007	2053	3661	1255	629	1127
Ind. Refl.	36 (R_{int} = 0.0819	39 (R_{int} = 0.1160)	129 (R_{int} = 0.0824)	536 (R_{int} = 0.1156)	189 (R_{int} = 0.0669)	49 (R_{int} = 0.0722)	77 (R_{int} = 0.0485)
Extinction coefficient	0.0003(2)	0.014(2)	0.015(1)	0.0023(7)	0.0050(7)	0.05(2)	0.062(2)
# of param.	5	6	12	20	13	7	6
Largest peak / hole ($e/Å^3$)	0.452/-1.259	0.800/-0.432	1.824/-1.370	8.038 /-10.606	1.479/-1.888	1.327 /-1.403	0.738/-0.785
Goodness-of-fit on $\|F^2\|$	1.384	1.252	1.263	1.165	1.191	1.529	1.591
***R* indices** [$I > 2\sigma(I)$]	R_1 = 0.0238 wR_2 = 0.0237	R_1 = 0.0110 wR_2=0.0264	R_1 = 0.0280 wR_2=0.0326	R_1 = 0.0749 wR_2 = 0.1321	R_1 = 0.0244 wR_2 = 0.0482	R_1 = 0.0293 wR_2 = 0.0727	R_1 = 0.0111 wR_2 = 0.0581
***R* indices** [all data]	R_1 = 0.0238 wR_2 = 0.0237	R_1 = 0.0135 wR_2=0.0274	R_1 = 0.0430 wR_2=0.0343	R_1 = 0.1195 wR_2 = 0.1530	R_1 = 0.0316 wR_2 = 0.0511	R_1 = 0.0293 wR_2 = 0.0727	R_1 = 0.0120 wR_2 = 0.0603

Table 5.3.3. Atomic coordinates and isotropic temperature parameters (U_{eq}) for Gd $(Co_{1-x}Ga_x)_2$ (x = 0, 1/6, 1/3, 1/2, 2/3, 5/6, and 1).

Atom	Site (point	Occupancy	x/a	y/b	z/c	U_{eq} (Å^2)
		$GdCo_2$ ($MgCu_2$-type)				
Gd1	8*a*	1	1/8	1/8	1/8	0.012(1)
Co1	16*d*($\bar{3}m$)	1	1/2	1/2	1/2	0.012(1)
		$GdCo_{1.67}Ga_{0.33}$ ($MgCu_2$-type)				
Gd1	8*a*($\bar{4}3m$)	1	1/8	1/8	1/8	0.010(1)
Co1/Ga11	16*d*($\bar{3}m$)	0.83/0.17	1/2	1/2	1/2	0.009(1)
		$GdCo_{1.33}Ga_{0.67}$ ($MgZn_2$-type)				
Gd1	4*f*(3*m*)	1	2/3	1/3	0.0617(1)	0.009(1)
Co1/Ga11	2*a*($\bar{3}m$)	0.67/0.33*	0	0	0	0.003(1)
Co2/Ga22	6*h*(*mm*)	0.67/0.33*	0.1674(2)	0.3348(5)	1/4	0.009(1)
		GdCoGa (SrMgSi-type)				
Gd1	4*c* (*m*)	1	0.0110(2)	1/4	0.7025(2)	0.013(1)
Co1	4*c* (*m*)	1	0.1978(4)	1/4	0.0924(5)	0.013(1)
Ga1	4*c* (*m*)	1	0.3232(7)	1/4	0.4233(6)	0.020(1)
		$GdCo_{0.67}Ga_{1.33}$ ($CeCu_2$-type)				
Gd1	4*e*(*mm*)	1	0	3/4	0.4541(1)	0.015(1)
Co1/Ga11	8*h*(*m*)	0.33/0.67	0	0.4443(2)	0.1648(1)	0.019(1)
		$GdCo_{0.33}Ga_{1.67}$ (AlB_2-type)				
Gd1	1*a*(6/*mmm*)	1	0	0	0	0.017(2)
Co1/Ga11	2*d*($\bar{6}m2$)	0.17/0.83	1/3	2/3	1/2	0.037(3)
		$GdGa_2$ (AlB_2-type)				
Gd1	1*a*(6/*mmm*)	1	0	0	0	0.008(1)
Ga1	2*d*($\bar{6}m2$)	1	1/3	2/3	1/2	0.012(1)

*Co/Ga occupancy was not refined

5.3.3 Magnetometry

Temperature-dependent magnetization was measured in a 100 Oe field from 300 (or 350) to 5 K, or 550 to 300 K, in a field-cooled (FC) mode using a Superconducting Quantum Interference Device (SQUID) on the Magnetic Property Measurement System (MPMS). The

maxima in the derivatives of the magnetization with respect to temperature were taken as Curie (T_C) temperatures. Temperatures of the cusps on the temperature-dependent magnetizations were treated as Neel temperatures (T_N).

5.3.4 Electronic Structure Calculations

Electronic structure calculations were performed using the Stuttgart *Tight-Binding*, *Linear-Muffin-Tin Orbital* program with *Atomic Sphere Approximation* (TB-LMTO-ASA).[15] The atomic sphere approximation uses overlapping Wigner-Seitz (WS) spheres to fill space. The WS sphere for Gd ranges from 3.3273 a.u. for $GdCo_2$ to 4.1208 a.u. for $GdGa_2$, Co ranges from 2.7167 a.u. in $GdCo_2$ to 2.7561 a.u. in GdCoGa, and Ga ranges from 2.7783 a.u. in GdCoGa to 2.5393 a.u. in $GdGa_2$. The symmetry of the potential is considered spherical in each WS sphere and a combined correction is used to account for the overlapped spheres. The overall overlapped volume for $GdCo_2$ was 6.444%, GdCoGa was 9.531%, and $GdGa_2$ was 6.315% and no empty spheres were necessary for any of the calculations. The exchange and correlation were treated both with the von Barth-Hedin local-density approximation (LDA)[16] and the local spin-density approximation (LSDA).[17] All relativistic effects except spin-orbit coupling were taken into account using a scalar relativistic approximation.[18] The basis sets included Gd (6*s*, 6*p*, 5*d*), Co (4*s*, 4*p*, 3*d*), and Ga (4*s*, 4*p*). The Gd 4*f* wavefunctions were considered as pseudo-core orbitals with 7 electrons, and were not included into the electronic density of states (DOS) and crystal orbital Hamilton population (COHP) analyses.[19] Reciprocal space integrations were performed with k-point meshes of 145 for the cubic $GdCo_2$, 1053 for the orthorhombic GdCoGa, and 793 for the hexagonal $GdGa_2$.

Optimization of atomic structures were performed using the Vienna Ab initio Simulation package (VASP),[20,21] which uses projector augmented-wave (PAW)[22] pseudopotentials that were adopted with the Perdew-Burke-Ernzerhof generalized gradient approximation (PBE-GGA), where scalar relativistic effects are included.[23] The conjugate gradient algorithm was used with an energy cut-off of 500 eV and 13 x 13 x 13 Monkhorst-Pack[24] k-points meshes. The linear tetrahedron method[25] was used for integrations involving the irreducible wedge of the Brillouin Zone. Total energies, magnetic moments (calculated as the difference of majority and minority spins), and electronic structure plots were evaluated. See the Supporting Information for further details of the results obtained from VASP calculations.

5.4 Results and Discussion

5.4.1 Structural Features and Transformation

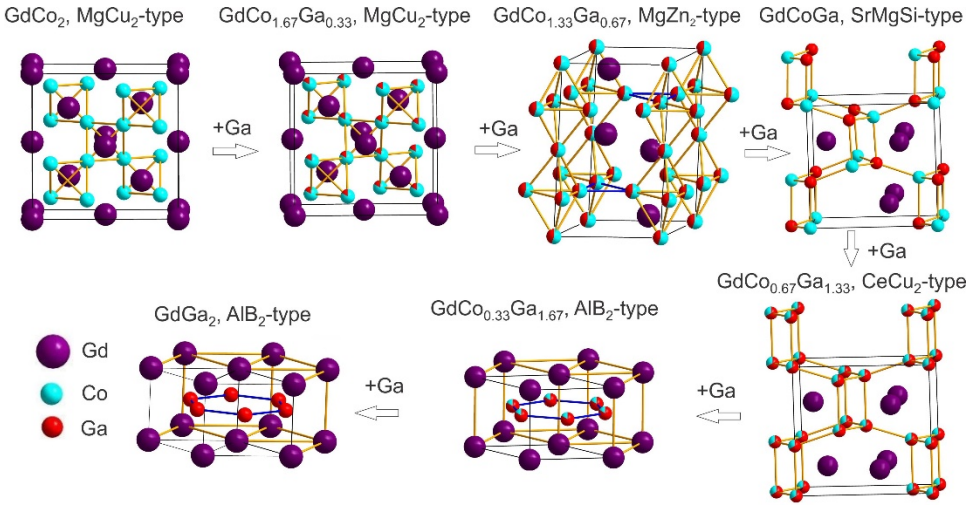

Fig. 5.4.1. Crystal structures of $Gd(Co_{1-x}Ga_x)_2$ (x = 0, 1/6, 1/3, 1/2, 2/3, 5/6, and 1).

X-ray diffraction results can be summarized as follows: i) five structures are present in the $Gd(Co_{1-x}Ga_x)_2$ (x = 0, 1/6, 1/3, 1/2, 2/3, 5/6, and 1) system, suggesting a close relationship between Co/Ga ratio and crystal structures (**Fig. 5.4.1**) ; ii) impurities in the cast samples decrease with Ga content increasing, which indicates that $Gd(Co_{1-x}Ga_x)_2$ phases are more easily

formed at a higher Ga content; iii) samples become pure after annealing except for GdCoGa, which contains significant $MgZn_2$-type impurities (13 wt. %).

Both annealed $GdCo_2$ ($x = 0$) and $GdCo_{1.67}Ga_{0.33}$ ($x = 1/6$) adopt the cubic $MgCu_2$-type structure. Diffraction peaks on the powder XRD pattern of $GdCo_{1.67}Ga_{0.33}$ shifted to lower scattering angles compared with that of $GdCo_2$, suggesting an increase in the unit cell parameters of $GdCo_{1.67}Ga_{0.33}$. (**Table 5.3.1**) This is expected because the atomic size of Ga is slightly larger than that of Co. Indexing of the Bragg peaks for $GdCo_2$ indicated a cubic lattice, isostructural with the Laves $MgCu_2$-type one. There are two independent crystallographic sites in the unit cell: Gd atoms occupy the 8*a* site while Co atoms are on the 16*d* site. For $GdCo_{1.67}Ga_{0.33}$, Gd atoms are still on the 8*a* site, while Ga atoms share the 16*d* site with Co.

Annealed $GdCo_{1.33}Ga_{0.67}$ ($x = 1/3$) adopts a hexagonal $MgZn_2$-type structure, which has three crystallographic sites: 2*a*, 4*f* and 6*h*. Gd atoms fully occupy the 4*f* site, while Co and Ga are on the 2*a* and/or 6*h* site. However, the Co/Ga occupancy could not be refined due to their similar scattering factors. A statistical Co/Ga distribution with the 0.67/0.33 ratio was assumed both on the 2*a* and 6*h* sites.

GdCoGa ($x = 1/2$) and $GdCo_{0.67}Ga_{1.33}$ ($x = 2/3$) adopt orthorhombic structures with the *Pnma* and *Imma* space groups, respectively. As seen in **Fig. 5.4.1**, the orthorhombic structures are very similar; in fact the GdCoGa structure is an ordered variant of the $GdCo_{0.67}Ga_{1.33}$ one. There are three 4*c* sites, occupied separately by Gd, Co, and Ga, in the orthorhombic GdCoGa phase. On the other hand, there are two crystallographic sites in the orthorhombic $GdCo_{0.67}Ga_{1.33}$ phase: Gd atoms occupy the 4*e* site, and Co and Ga atoms share the 8*h* site. It is worth mentioning that it was more difficult to obtain a pure GdCoGa phase then a pure

$GdCo_{0.67}Ga_{1.33}$ phase. An impurity in GdCoGa could not be eliminated even after annealing at 850°C for 1 week or longer time.

$GdCo_{0.33}Ga_{1.67}$ (x = 5/6) and $GdGa_2$ (x = 1) adopt the hexagonal AlB_2-type structure. There are two crystallographic sites in the structure: Gd atoms fully occupy the 1*a* site whereas Co and Ga atoms are on the 2*d* site. Gd atoms form two triangular prisms in one unit cell, and Co or Ga atoms are located in the center of these triangular prisms. Increased *c* lattice parameter and volume were observed for $GdGa_2$, which is due to the larger atomic size of Ga. On the other hand, the *a* lattice parameter decreased slightly. Therefore, the *a*/*c* ratio for $GdCo_{0.33}Ga_{1.67}$ and $GdGa_2$ is 1.20 and 1.02, respectively. The abnormal lattice parameter change in $GdCo_{0.33}Ga_{1.67}$ and $GdGa_2$ is probably related to the structural changes.

As the Ga content increases, the structures change from a "condensed cluster-based" → "3D Network" → "2D Network". The cubic Laves phase has the Co atoms in vertex-sharing tetrahedral clusters. In the hexagonal Laves phase, the Co tetrahedra are still present, but now they are stacked along the *c* axis via alternating vertex- and face-sharing motifs. On moving to GdCoGa and $GdCo_{0.67}Ga_{1.33}$, the tetrahedral clusters are lost, but the Co and Ga atoms sit in distorted tetrahedral coordination environments. These structures have extended networks of 6- and 8-membered rings along with ladders of 4-membered rings. By increasing the Ga content even more, the 3D network is converted into the 2D network of the graphene-like sheets of Ga. Coordination numbers (CN) of Co/Ga also change for the different types of networks. In the cubic Laves phases, Co/Ga has a CN of 6, then changes to the CN of 4 in the 3D network, and finally to a CN of 3 in the 2D network. Electronic structure calculations were employed to gain some insights about the chemical bonding features and structural variation of the $Gd(Co_{1-x}Ga_x)_2$ system.

5.4.2 Magnetic Properties

Temperature-dependent magnetization of $Gd(Co_{1-x}Ga_x)_2$ (x = 0, 1/6, 1/3, 1/2, 2/3, 5/6, and 1) were measured (**Fig. 5.4.2**). For the Co-free phase, i.e. $GdGa_2$, the magnetic transition becomes antiferromagnetic, with a Neel temperature of 20 K, in accordance with the previous reported results.[26] For other samples, T_C decreases with the increasing Ga content, which indicates that Ga substitution weakens the magnetic interactions controlled via the RKKY[27–29] mechanism. GdCoGa and $GdCo_{0.67}Ga_{1.33}$ resemble each other with respect to magnetic trnasition: both of them has a sharp magnetic transition at ~55 K, but the former has a second transition at 148 K, while the latter at 204 K. The apperance of two magnetic transitions indicates the presence of impurities in the two samples, which is in accordance with the powder X-ray diffraction results. Magnetic transitions of $Gd(Co_{1-x}Ga_x)_2$ (x = 0, 1/6, 1/3, 1/2, and 2/3) are very sharp at T_C, suggesting that these samples may have interesting magnetocaloric properties.

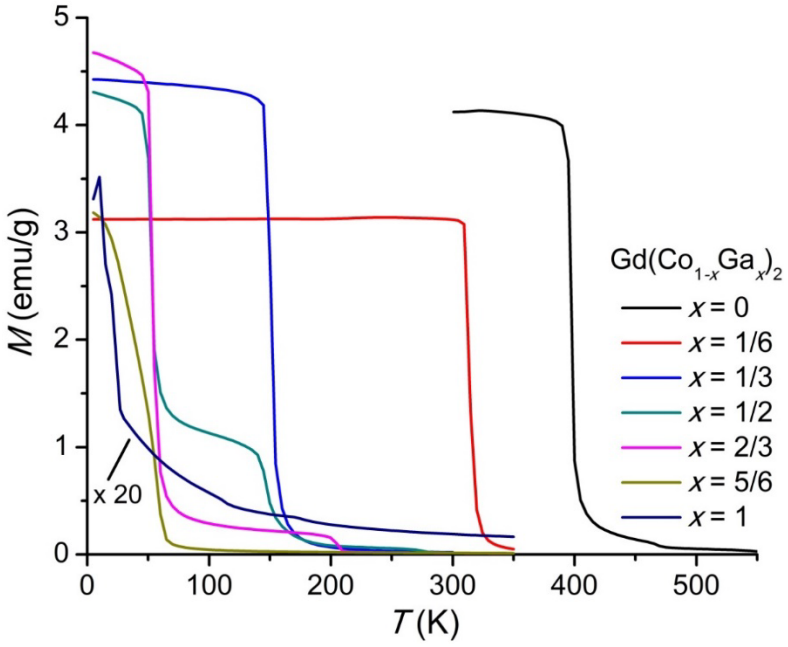

Fig. 5.4.2. Temperature dependence of magnetization for $Gd(Co_{1-x}Ga_x)_2$ (x = 0, 1/6, 1/3, 1/2, 2/3, 5/6, and 1) under a magnetic field of 100 Oe. Magnetization for x = 1 is magnified by 20.

5.4.3 Electronic Structure Calculations

The structures described above change significantly from densely packed to network-type as the Ga content increases in this system. Given the variation in the valence electron count, a computational approach was undertaken to shed light on chemical bonding features that could be underpinning these changes. At first, just the stoichiometric compounds $GdCo_2$, GdCoGa, and $GdGa_2$ were studied, with a more in-depth analysis of various nonstoichiometric cases coming in a subsequent report. For these three compounds, the properties studied include DOS, pairwise orbital interactions via COHP curves, formation energies, and magnetic moments. An initial comparison was made by calculating the total energies per formula unit (eV/f.u.) for each binary compound in each of the three observed structure types, with the results listed in **Table 5.4.1**, and in agreement with the observed structures.

Table 5.4.1. Total energies per Gd, calculated using VASP, of $GdCo_2$ and $GdGa_2$ in different structure types observed for $GdCo_2$, GdCoGa, and $GdGa_2$.

Alloys	$MgCu_2$-type (meV/Gd)	SrMgSi-type (meV/Gd)	AlB_2-type (meV/Gd)
$GdCo_2$	0	+652.4	+902.1
$GdGa_2$	+720.4	+145.1	0

In general, the total energies of these models increase as the number of nearest-neighbor Co-Co interactions decreases or as the number of nearest-neighbor Ga-Ga interactions increases. The largest total energy difference occurs between the cubic Laves phase and the orthorhombic SrMgSi-type for $GdCo_2$ because this structural change is accompanied by a coordination change around each Co atom from coordination number (CN) of 6 to 4, with inequivalent Co-Co bond lengths. Moreover, $GdCo_2$ in the AlB_2-structure type

gives the highest total energy, most likely due to the Co atoms being just three-coordinate with other Co atoms.

To determine the relative stabilities of the binary and ternary compounds, estimated formation energies from the elements or the binary endpoints were calculated for $GdCo_2$, GdCoGa, and $GdGa_2$. According to total energies calculated using VASP, $GdCo_2$ is favored over the individual elements by 0.3782 eV/Gd. and $GdGa_2$ is favored over its constituents by 1.9401 eV/Gd. With respect to Gd, Co, and Ga, GdCoGa is energetically favored by 1.4132 eV/Gd, and is also favored over the binary endpoints $GdCo_2$ and $GdGa_2$ by 0.2540 eV/Gd.

To gain an understanding of the chemical bonding features and structural variation in $Gd(Co_{1-x}Ga_x)_2$, the electronic density of states (DOS) and crystal orbital Hamilton population curves (COHP) were calculated using both the local-density approximation (LDA) and the local spin-density approximation (LSDA). DOS and COHP curves were calculated with both TB-LMTO-ASA and the Local Orbital Basis Suite Towards Electronic-Structure Reconstruction (LOBSTER)[19,30], the latter using the output files of VASP. The TB-LMTO-ASA code was used to treat the Gd 4*f* orbitals as core orbitals occupied by 7 electrons,so that the overlap population analysis considers just the valence *s, p,* and *d* wavefunctions of the constituent elements. Overall, the DOS and COHP curves near the Fermi levels calculated with both methods are qualitatively similar, but the integrated COHP (ICOHP) values differ, and are most significant for $GdCo_2$. The results calculated using VASP/LOBSTER are included in the Supporting Information.

5.4.3.1 Electronic structure of $MgCu_2$-type $GdCo_2$

Including spin-polarization into the calculation of the total energy of $MgCu_2$-type $GdCo_2$ is important because, without it, optimization produces a unit cell that is significantly

smaller than the experimentally determined unit cell. With spin-polarization the corresponding optimization yields lattice parameters and bond lengths that are close to the experimental ones (see Table S1 in Supporting Information).

Previous experimental and theoretical studies of $MgCu_2$-type GdX_2 (X = Fe, Co, Ni) compounds have shown that the individual Gd magnetic moments are ferromagnetically coupled, so Gd was treated in the same way in these calculations.[31–33] The magnetic moment on each Gd in $GdCo_2$ is calculated by LSDA+U (for Gd: U = 6.70 eV and J = 0.70 eV[34]) as 7.405μ_B compared to 7.433μ_B, which was calculated by B. Zegaou et al. using all-electron full-potential linear muffin-tin orbital method with GGA+U.[31] The magnetic moment for Co is calculated as 1.286μ_B, compared with the value of 1.175μ_B reported by B. Zegaou et al.,[31] and oriented oppositely to that of Gd. Therefore, $GdCo_2$ is calculated to be ferrimagnetic with a net saturated magnetic moment of 4.861μ_B.

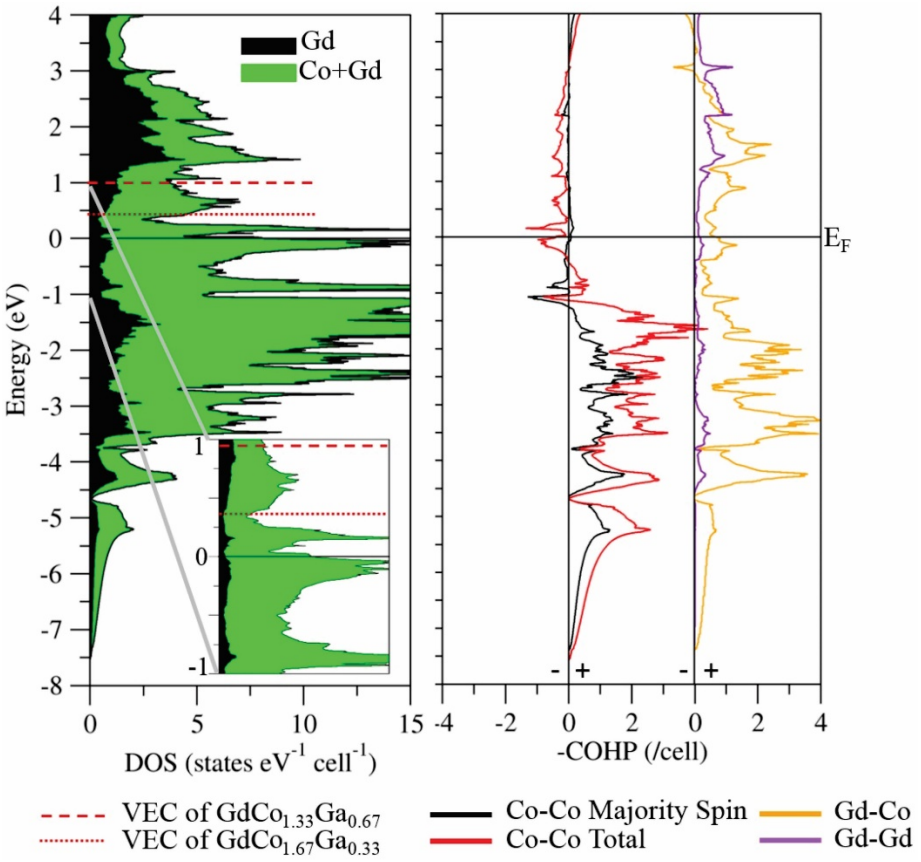

Fig. 5.4.3. (left) DOS and (right) COHP curves calculated with LSDA for $GdCo_2$.

The DOS and COHP curves for $GdCo_2$ are juxtaposed in **Fig.5.4.3**. In the DOS, Co orbitals dominate the lower energy regions up to ca. 1.5 eV above E_F, and Gd states contribute significantly above these energies. In addition, although there are a lot of states around the Fermi level, the Co–Co and Gd–Co COHP curve shows overall weak orbital interactions from ~0.8 eV below to ~0.8 eV above E_F for $GdCo_2$. This result suggests that the valence electron count can be either increased or decreased without a large structural effect, so that $MgCu_2$-type $GdCo_2$ can be readily doped, a chemical effect frequently observed for densely packed intermetallics.

Analysis of the COHP curves, presented in **Table 5.4.2**, shows that the Co–Co and Gd–Co interactions contribute essentially equally to cohesion when the coordination numbers are included. Co–Co interactions are approximately twice as strong as Gd–Co interactions.

The Co–Co COHP curve shows optimized bonding, i.e., only bonding orbitals filled, at ~0.5 eV below E_F for $GdCo_2$, an energy value corresponding to 19.09 valence electrons per formula unit (e^-/f.u.), which is close to $GdFe_2$. $GdFe_2$ (19 e^-/f.u.), $GdCo_2$ (21 e^-/f.u.), and $GdNi_2$ (23 e^-/f.u.) all crystallize in the cubic Laves phase structure type. In the Co–Co COHP curve for $GdCo_2$, 21 and 23 e^-/f.u. reside, respectively, in nonbonding and slightly antibonding regions. Thus, for *RE*(*TM*)$_2$ Laves phases, as the valence electron count increases the overall *TM*-*TM* bonding is sacrificed for *RE*-*TM* bonding. (*TM* = transition metal).

Table 5.4.2. COHP analysis of $GdCo_2$.

Compound	Bonds	Distance (Å)	#/f.u.	–ICOHP (eV)	% ICOHP
$GdCo_2$	Co-Co	2.551	6	1.514	49.39
	Gd-Co	2.992	12	0.702	45.78
	Gd-Gd	3.125	2	0.444	4.83

Since $GdCo_2$ and $GdCo_{1.67}Ga_{0.33}$ have the same cubic crystal structure, a rigid band model applied to the DOS of $GdCo_2$ may give some insights of the electronic structure of the mixed-site, ternary compound. For $GdCo_{1.67}Ga_{0.33}$, the VEC = 22.32 e^-/f.u. would place the Fermi level in a pseudogap in the DOS curve, suggesting a great electronic stability and the reasonability of rigid band model. In the COHP curves, this E_F resides at a local point of nonbonding states in the antibonding region of Co–Co states and weakly bonding Gd–Co states. Therefore, according to the rigid band model, $GdCo_{1.67}Ga_{0.33}$ is electronically stable in the cubic $MgCu_2$-Laves phase structure.

Also, these calculations suggest that 23 e^-/f.u. is probably the highest VEC that the cubic Laves phase structure can sustain in this system before structural transitions occur. This argument is supported experimentally as the first transition is observed for the VEC = 23.68 e^-/f.u. ($GdCo_{1.33}Ga_{0.67}$). The experimental data show that $GdCo_{1.33}Ga_{0.67}$ adopts the hexagonal $MgZn_2$-type Laves phase. The Fermi level corresponding to 23.67 e^-/f.u. is just below the

region in the DOS where Gd states start to dominate, and the COHP curves show no significant antibonding states. Therefore, $GdCo_{1.33}Ga_{0.67}$ remains densely packed, but there are other factors contributing to its structure that will be addressed in a subsequent paper.

5.4.3.2 Orthorhombic SrMgSi-type GdCoGa

The SrMgSi-type structure adopted by GdCoGa is quite prevalent with numerous ternary compounds, such as MgPtGa, CaPtGa, GdPtGa, CaPtGe, and GdPtGe. **Fig. 5.4.4** shows the DOS and the COHP curves, calculated for the experimentally refined structure. One major structural difference between GdCoGa and $GdCo_2$ is there are no nearest-neighbor Co–Co contacts so that the Co 3*d* band is significantly narrower in the DOS of GdCoGa than in the $GdCo_2$ DOS. The Fermi level for GdCoGa lies on the upper shoulder of predominantly Co 3*d* states. Within the various COHP curves, all near-neighbor interactions have weakly bonding interactions at E_F; in particular, the Co–Ga interaction is nearly nonbonding. From the COHP analysis summarized in **Table 5.4.3**, Co–Ga interactions dominate the contribution to the total integrated COHP, followed by nearly equal contributions from Gd–Co and Gd–Ga interactions. Gd–Gd interactions contribute only ~4% to the total ICOHP, as seen also for $GdCo_2$.

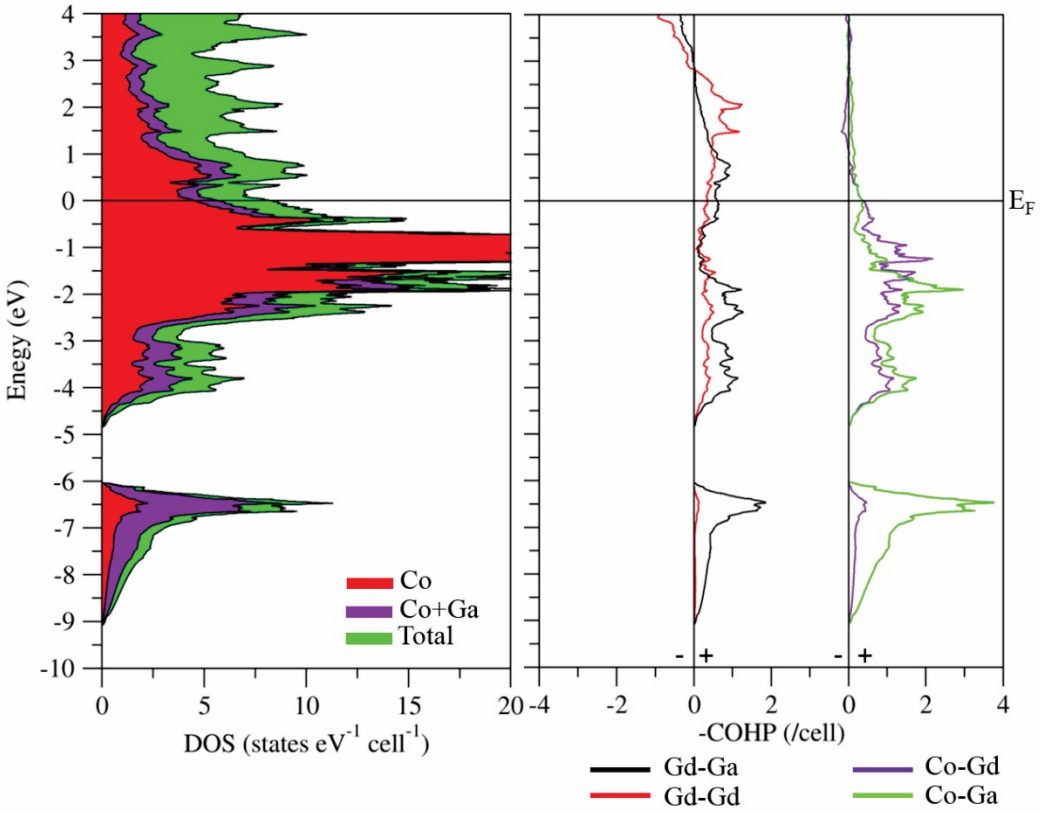

Fig. 5.4.4. DOS (left) and COHP (right) calculated with LSDA for GdCoGa.

Table 5.4.3. COHP analysis of experimental determined and VASP optimized GdCoGa.

Compound	Bonds	Distance (Å)	#/Gd	–ICOHP (eV)	% ICOHP
Experimental GdCoGa	Gd-Gd	3.600-3.619	2	0.401-0.294	3.91
	Gd-Co	2.94-3.358	6	0.901-0.587	27.39
	Gd-Ga	3.021-3.120	6	0.767-0.728	26.54
	Co-Ga	2.490-2.667	4	2.145-1.387	42.16
VASP optimized GdCoGa	Gd-Gd	3.470-3.671	2	0.463-0.272	4.26
	Gd-Co	2.813-3.643	6	1.076-0.325	25.47
	Gd-Ga	3.047-3.184	6	0.770-0.648	25.00
	Co-Ga	2.463-2.551	4	2.177-1.724	43.11
	Co-Co	3.198	1	0.372	2.16

A complete structural optimization using VASP converged at a structure that is distorted, compared to the experimentally determined one, for which the optimized *a* and *b* parameters are 0.32% and 0.89% larger respectively and the *c* parameter is 2.81% smaller than experimental values. (**Fig.5.4.5**) Various starting models were constructed (see Table S2 of Supporting Information), including one using data from Sichevich et al.[8], all of these

converged to the same GdCoGa structure. Other compounds that crystallize in the SrMgSi-type structure, e.g., isoelectronic DyCoGa[35] and CaPtGa[36] were analyzed to see if this outcome is specific to GdCoGa. Optimization of DyCoGa also created a unit cell with a significantly smaller *c* parameter, whereas CaPtGa converged to a slight shrinkage in the *a* direction along with a small expansion in *c* (from 7.595 Å to 7.685 Å).

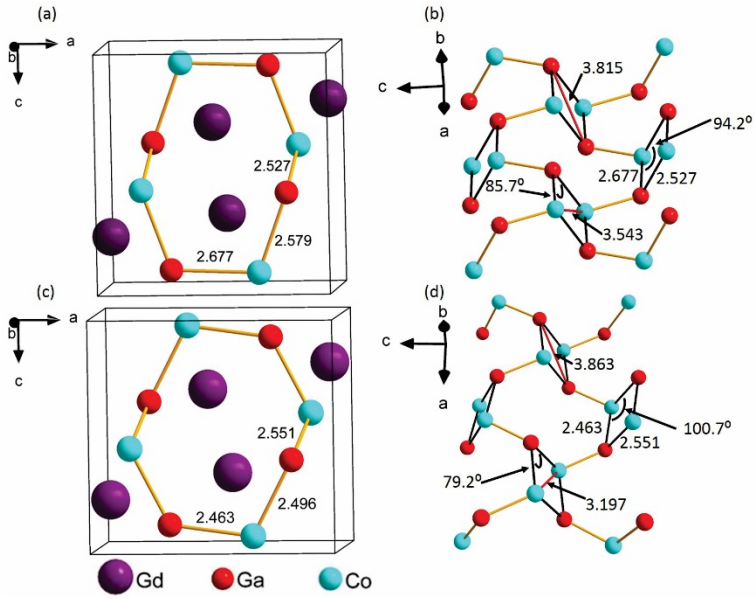

Fig. 5.4.5. Unit cell and zig-zag chains of "4 member rings" for experimental determined **((a)** and **(b))** and VASP optimized ((**c)** and **(d))** GdCoGa structures.

Total energy calculations were also performed to examine the site preference of Co and Ga for their respective Wyckoff 4*c* sites in GdCoGa. The most energetically favorable configuration yields zig-zag ribbons of distorted 4-membered rings with Co and Ga atoms on opposite corners of the rings, with Ga atoms on the opposite corners that are farther apart ~3.9 Å than the other corners (~3.2 Å). In the experimental structure, these "squares" have two bond angles of ~86° and two bond angles of ~94°. The VASP optimized structure has two bond angles of ~79° and two bond angles of ~101°. This canting of the "squares" has caused the Co atoms on opposite corners to come closer so that some weak Co-Co interactions developed.

(**Fig. 5.4.5**) Therefore, when calculating the COHP for the optimized structure, faint Co-Co interactions are observed in the structure, which may have some contributions to the decrease of the *c* lattice parameter in the VASP optimized structure. (**Table 5.4.3**)

However, the weak Co-Co interaction must not be the only reason for such significant decrease of the *c* lattice parameter. The many structural optimizations on both experimental and theoretical models lead us to one of two conclusions: either GdCoGa is not fully stoichiometric or there is a degree of disorder on the Co and Ga sites. If the compound is not stoichiometric and slightly Ga-rich, this would introduce Ga–Ga homoatomic interactions which can shorten the *c* parameter. Having a degree of disorder on the Co and Ga sites can also introduce Co–Co and Ga–Ga homoatomic interactions. Further details of these assessments will be reported in a subsequent paper.

5.4.3.3 Hexagonal AlB_2-type $GdGa_2$

The electronic DOS and COHP curves for AlB_2-type $GdGa_2$ calculated using LSDA are shown in **Fig. 5.4.6**. The optimized lattice parameters are very close to the experimental ones (**see Table S3 of Supporting Information**). The Fermi level of $GdGa_2$ with 9 e^-/f.u. resides on the shoulder of a peak, which is the lower energy limit of a weakly bonding (nearly nonbonding) set of states. The COHP analysis presented in **Table 5.4.4** indicates that the Gd–Ga interactions have the largest contribution, due in part to their frequency, followed by the Ga–Ga bonds, and then by the Gd-Gd interactions. The Ga atoms form the graphene-like sheets, and each Ga has 3 bonds to other Ga in these sheets. There is a pseudogap in the DOS corresponding to 9.9 e^-/f.u., and the center of this pseudogap coincides with transitions from bonding to antibonding interactions in the COHP plots for all (Ga–Ga, Gd–Ga, and Gd–Gd) interactions. Above 9.9 electrons, the Ga-Ga anti-bonding states are being filled, as a result,

the graphene-like sheets should become disrupted and be no longer planar as they distort to handle a higher electron count. Even though the overall bonding contribution of these sheets is less than the contribution of the Gd-Ga bonding, the graphene-like sheets will be disrupted first at the VEC above 9.9 e^-/f.u.

Table 5.4.4. COHP Analysis of $GdGa_2$

Compound	Bonds	Distance	#/Gd	–ICOHP (eV)	% ICOHP
$GdGa_2$	Ga-Ga	2.452	3	2.508	38.40
	Gd-Ga	3.210	12	0.919	56.28
	Gd-Gd	4.142-4.248	4	0.225-0.296	5.32

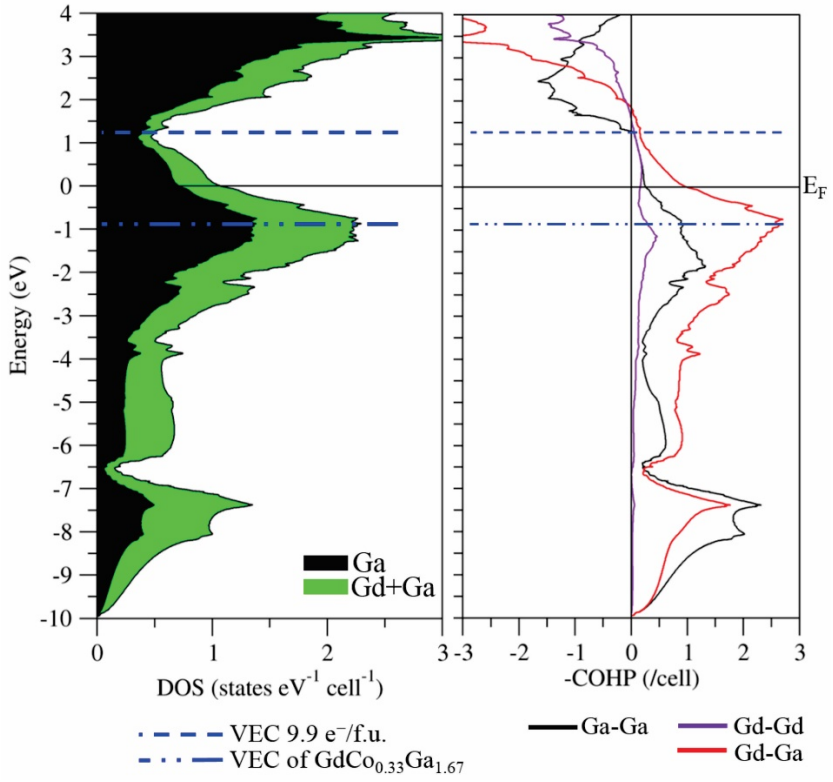

Fig. 5.4.6. DOS and COHP calculated with LSDA for $GdGa_2$.

Ternary $GdCo_{0.33}Ga_{1.67}$ is isostructural to $GdGa_2$, but replacing Ga with Co will lower the Fermi level of the DOS according to the rigid band model. To count valence electrons in $GdCo_{0.33}Ga_{1.67}$ and estimate its Fermi level in the DOS of $GdGa_2$, Co is given a –1 valence electron because Ga sites were not assigned valence 3*d* orbitals for the calculation. As a result, the valence electron count for $GdCo_{0.33}Ga_{1.67}$ is 7.68 e^-/f.u., and its Fermi level falls at ca. –1

eV in the DOS. As the COHP curves show, reducing the valence electron count of $GdGa_2$ by Co substitution depletes significant interatomic bonding states. The Fermi level estimated for $GdCo_{0.33}Ga_{1.67}$ by the rigid band model falls on a large peak in the DOS, which would suggest an electronic instability. Since Co atoms will introduce valence 3*d* orbitals to energy regions near the Fermi level, a rigid bond model applied to the DOS of $GdGa_2$ is inappropriate.

5.5 Conclusions

$Gd(Co_{1-x}Ga_x)_2$ (x = 0, 1/6, 1/3, 1/2, 2/3, 5/6, and 1) phases adopt five structures as a function of x value. The structures change from a "condensed cluster-based" → "3D Network" → "2D Network" with an increasing Ga content. In terms of coordination numbers (CN), the CN of Co or Ga is 6 in the cubic $GdCo_2$, then reduces to 4 in the 3D network, and finally to 3 in the 2D network. Electronic factors appear to be the reason for the structural transformations in the $Gd(Co_{1-x}Ga_x)_2$ system. Spin polarization appears necessary for the TB-LMTO-ASA calculations in this work, therefore, DOS and COHP were calculated using the LSDA. $GdCo_2$ adopts a cubic $MgCu_2$-type structure, which could be sustained to the VEC = 23 e^-/f.u. Therefore, $GdCo_{1.67}Ga_{0.33}$ (22.32 e^-/f.u.) adopts the same $MgCu_2$-type structure, while a structural transition occurs for $GdCo_{1.33}Ga_{0.67}$ with VEC = 23.68 e^-/f.u. Although Co-Ga bonds are fewer compared with Gd-Co and Gd-Ga ones, they dominate the total bonding in the unit cell of orthorhombic GdCoGa. The VASP optimization of the GdCoGa structure generates a unit cell with a smaller *c* lattice parameter, suggesting that GdCoGa may not fully stoichiometric or has disorder on the Co and Ga sites. The total energy calculation suggests that the optimized structure is favored by 0.08352 eV/Gd. $GdGa_2$ has a VEC of 9 e^-/f.u. and a pseudogap at 9.9 e^-/f.u. Although COHP data indicates that Gd-Ga bonds contribute the most to the overall bonding, Ga-Ga bonds, which form graphene-like sheets, are fist to break above

the VEC of 9.9 e^-/f.u. Ga substitution reduces the strength of the long-range magnetic interactions, which causes T_C to decrease with an increasing Ga content. The observed sharp magnetic transitions suggest that $Gd(Co_{1-x}Ga_x)_2$ are potential magnetocaloric materials.

5.6 Acknowledements

This work was supported by the Natural Science and Engineering Research Council of Canada through the Discovery Grant Program. Computations were performed on the CRUNCH cluster supported by Iowa State University Computation Advisory Committee under Project No. 202-17-10-08-0005.

5.7 Supporting Information

Supporting information for this chapter can be found in APPENDIX C.

5.8 References

[1] V.K. Pecharsky, K.. Gschneidner Jr., Giant Magnetocaloric Effect in $Gd_5(Si_2Ge_2)$, Phys. Rev. Lett. 78 (1997) 4494–4497.

[2] I. Harris, R. Mansey, G. Raynor, Rare earth intermediate phases III, J. Less Common Met. 9 (1965) 270–280. doi:10.1016/0022-5088(65)90020-2.

[3] S. Khmelevskyi, P. Mohn, The order of the magnetic phase transitions in RCo_2 (R = rare earth) intermetallic compounds, J. Phys. Condens. Matter. 12 (2000) 9453–9464. doi:10.1088/0953-8984/12/45/308.

[4] N.H. Duc, D.T. Kim Anh, P.E. Brommer, Metamagnetism, giant magnetoresistance and magnetocaloric effects in RCo_2-based compounds in the vicinity of the Curie temperature, Phys. B. 319 (2002) 1–8.

[5] N.H. Duc, D.T.K. Anh, Magnetocaloric effects in RCo2 compounds, J. Magn. Magn. Mater. 242–245 (2002) 873–875. doi:10.1016/S0304-8853(01)01328-2.

[6] Z.W. Ouyang, G.H. Rao, H.F. Yang, W.F. Liu, G.Y. Liu, X.M. Feng, J.K. Liang, Structure and magnetic phase transition in $R(Co_{1-x}Ga_x)_2$ (R = Nd, Gd, Tb, Dy) compounds, Phys. B. 344 (2004) 436–442.

[7] F. Yuan, J.E. Greedan, Y. Mozharivskyj, Structural and Magnetic Studies on the New Laves Phases $RE(Co_{0.667}Ga_{0.333})_2$ (RE = Gd, Tb, Dy, Ho, and Er). Magnetocaloric

Effect of $Gd(Co0_{.667}Ga_{0.333})_2$, J. Magn. Magn. Mater. In press (2017) 0–25. doi:10.1016/j.jmmm.2017.06.030.

[8] O.M. Sichevich, R.E. Gladyshevskii, Y.N. Hrin', Y.P. YarMolyuk, The crystal structure of *R*GaCo (*R* = Pr, Nd, Sm, Gd, Tb, Dy, Ho, Er, Y), Dopovidi Akad. Nauk Ukr. RSR, Seriya B Geol. Khimichni Ta Biol. Nauk. 11 (1982) 57–59.

[9] L. Liang, L. Zeng, S. Liu, W. He, Crystal structure, thermal expansion and electrical properties of $GdCo_{0.67}Ga_{1.33}$, Phys. B. 426 (2013) 35–39. doi:10.1016/j.matchemphys.2008.07.008.

[10] E. Talik, J. Heimann, A. Chelkowski, Magnetic, structural and electrical properties of $Gd(Al_{1-x}Ga_x)_2$ compounds, J. Less-Common Met. 124 (1986) L13–L16.

[11] L.C. Pauling, The Nature of the Chemical Bond and the Structure of Molecules and Crystals: An Introduction to Modern Structural Chemistry, 3rd ed., Cornell University Press, Ithaca, NY, 1960.

[12] H. Oesterreicher, W.E. Wallance, Studies of pseudo-binary laves-phase systems containing lanthanides: I. Constitution and magnetic properties of the $GdAl_2$-$GdFe_2$, $GdAl_2$-$GdCo_2$ and $ErCo_2$-$ErAl_2$ systems, J. Less Common Met. 13 (1967) 91–102.

[13] B.A. Hunter, C.J. Howard, Australian Nuclear Science and Technology a Computer Program for Rietveld Analysis of X-Ray and Neutron, (2000) 27.

[14] G.M. Sheldrick, SHELXS-97 - Program for the Solution of Crystal Structures, University of Gottingen, Germany, 1997.

[15] O.K. Andersen, Z. Pawlowska, O. Jepsen, Illustration of the linear-muffin-tin-orbital tight-binding representation: Compact orbitals and charge density in Si, Phys. Rev. B. 34 (1986) 5253–5269.

[16] O.K. Andersen, O. Jepsen, Explicit, First-Principles Tight-Binding Theory, Phys. Rev. Lett. 53 (1984) 2571–2574.

[17] 0. Gunnarsson, B.I. Lundqvist, Exchange and correlation in atoms, molecules, and solids by the spin-density-functional formalism, Phys. Rev. B. 13 (1976) 4274–4298.

[18] D.D. Koelling, B.N. Harmon, A technique for relativistic spin-polarised calculations, J. Phys. C Solid State Phys. 10 (1977) 3107–3114.

[19] R. Dronskowski, P.E. Blöchl, Crystal orbital Hamilton populations (COHP): energy-resolved visualization of chemical bonding in solids based on density-functional calculations, J. Phys. Chem. 97 (1993) 8617–8624. doi:10.1021/j100135a014.

[20] G. Kresse, J. Furthmüller, Efficient iterative schemes for ab initio total-energy calculations using a plane-wave basis set, Phys. Rev. B. 54 (1996) 11169–11186. doi:10.1103/PhysRevB.54.11169.

[21] G. Kresse, J. Furthmüller, Efficiency of ab-initio total energy calculations for metals and semiconductors using a plane-wave basis set, Comput. Mater. Sci. 6 (1996) 15–50. doi:10.1016/0927-0256(96)00008-0.

[22] P.E. Blöchl, Projector augmented-wave method, Phys. Rev. B. 50 (1994) 17953–17979.

[23] J.P. Perdew, K. Burke, Y. Wang, Generalized gradient approximation for the exchange-correlation hole of a many-electron system, Phys. Rev. B. 54 (1996) 533–539.

[24] H.J. Monkhorst, J.D. Pack, Special points for Brillouin-zone integrations, Phys. Rev. B. 13 (1976) 5188–5192. doi:10.1103/PhysRevB.16.1748.

[25] P.E. Blöchl, O. Jepsen, O.K. Andersen, Improved tetrahedron method for Brillouin-zone integrations, Phys. Rev. B. 49 (1994) 16223.

[26] J.M. Barandiaran, D. Gignoux, J. Rodriguez-Fernandez, Magnetic properties and magnetic structure of hexagonal $GdGa_2$ and $GdCu_5$ compounds, Phys. B Phys. Condens. Matter. 154 (1989) 293–299. doi:10.1016/0921-4526(89)90162-2.

[27] M.A. Ruderman, C. Kittel, Indirect exchange coupling of nuclear magnetic moments by conduction electrons, Phys. Rev. 96 (1954) 99–102.

[28] T. Kasuya, A theory of metallic ferro- and antiferromagnetism on Zener's model, Prog. Theor. Phys. 16 (1956) 45–57.

[29] K. Yosida, Magnetic properties of Cu-Mn alloys, Phys. Rev. 106 (1957) 893–898. doi:10.1103/PhysRev.106.893.

[30] V.L. Deringer, A.L. Tchougréeff, R. Dronskowski, Crystal orbital Hamilton population (COHP) analysis as projected from plane-wave basis sets, J. Phys. Chem. A. 115 (2011) 5461–5466. doi:10.1021/jp202489s.

[31] B. Zegaou, N. Benkhettou, D. Rached, A.H. Reshak, S. Benalia, Electronic structure of GdX_2 (X = Fe, Co and Ni) intermetallic compounds studied by the GGA + U method, Comput. Mater. Sci. 87 (2014) 172–177. doi:10.1016/j.commatsci.2014.02.005.

[32] S.M. Saini, N. Singh, T. Nautiyal, S. Auluck, Comparative study of optical and magneto-optical properties of $GdFe_2$ and $GdCo_2$, J. Phys. Condens. Matter. 19 (2007) 176203. doi:10.1088/0953-8984/19/17/176203.

[33] C.M. Bonilla, D. Paudyal, J. Herrero-Albillos, V.K. Pecharsky, K.A. Gschneidner, L.M. Garcia, F. Bartolome, Formation of co moment in the paramagnetic phase of RCo_2, IEEE Trans. Magn. 50 (2014) 1700204/1-1700204/4. doi:10.1109/TMAG.2014.2330815.

[34] J. Yao, Y. Zhang, P.L. Wang, L. Lutz, G.J. Miller, Y. Mozharivskyj, Electronically induced ferromagnetic transitions in Sm_5Ge_4-type magnetoresponsive phases, Phys. Rev. Lett. 110 (2013) 1–5. doi:10.1103/PhysRevLett.110.077204.

[35] F. Liu, W. Ao, L. Wu, J. Li, Crystal structures of the compounds formed in $DyCo_2$-$DyGa_2$ pseudo-binary system at 773 K, Intermetallics. 17 (2009) 738–743. doi:10.1016/j.intermet.2009.02.014.

[36] K. Dascoulidou-Gritner, Schuster, H.U., Dascoulidou-Gritner,K. Schuster, H. U., Zeitschrift Fuer Anorg. Und Allg. Chemie. 620 (1994) 1151–1156.

CHAPTER 6. FROM LAVES TO ZINTL: BONDING ISSUES INFLUENCING THE STRUCTURAL VARIATION IN $GdCo_{2-x}Ga_x$

Asa Toombs[a], Fang Yuan[b], Yurij Mozharivskyj[b], Gordon J. Miller[a*]

[a]*Department of Chemistry, Iowa State Unviersity, Ames Iowa 50011-311 and Ames Laboratory, U.S. Department of Energy, Ames, IA 50011-311, USA.*

[b]*Department of Chemistry and Chemical Biology, Brockhouse Institute of Materials Research, McMaster University, 1280 Main Street West, Hamilton, Ontario L8S 4M1, Canada*

6.1 Abstract

Electronic structure calculations on $GdCo_{2-x}Ga_x$ (x = 0, 0.33, 0.67, 1.0, 1.33, 1.67 and 2) compounds were performed and analyzed to shed light on the driving force behind the structure changes between x = 0.33-0.67 (cubic to hexagonal), 0.67-1.0 (hexagonal to orthorhombic), 1.0-1.33 (Imma to Pnma), and finally 1.33-1.67 (orthorhombic to hexagonal). Multiple coloring models were created for the mixed site ternary compounds and total energies, density of states (DOS) and crystal orbital Hamilton population (COHP) curves were calculated for the different models. Integrated COHP values, which can give insights into the strength of individual interactions, were studied in each model to determine the effect of different geometric colorings on the overall contribution of individual types of interactions to the total COHP. Results indicate that the number of Ga–Ga homoatomic interactions has a large impact on the crystal structures and is a main driving force in causing the structures to change.

6.2 Introduction

A series of compounds with varying structures were found in the series of $GdCo_{2-x}Ga_x$ (x=0, 0.33, 0.67, 1.33, 1.67 and 2). This series of compounds is similar to those that Liu et.al found in the $DyCo_{2-x}Ga_x$.[1] The $RECo_2$ (RE = rare earth) compounds have been well studied, especially in regard to magnetic properties for possible applications such as magnetic

refrigeration.[2-5] The addition of Ga has been shown to increase the Curie temperature, which is beneficial for magnetic refrigeration applications, of $RECo_2$ compounds[6-8] and the Curie temperature of $RECo_2$ compounds peaks at 400 K for RE = Gd. This makes $GdCo_2$ a promising compound to substitute varying amounts of Ga into the structure to determine the effect on the Curie temperature.[5]

The volume of the GdX_2 (X=Mn, Fe, Co, Ni) binary compounds follows the trend of getting smaller with increased atomic number; $GdMn_2$ a=7.758 Å[9], $GdFe_2$ a= 7.390 Å[10], $GdCo_2$ a=7.252 Å, and $GdNi_2$ a= 7.205 Å.[11] The change in lattice parameter in moving from $GdMn_2$ to $GdFe_2$ is over twice as large as the changes going from $GdFe_2$ to $GdCo_2$ and $GdCo_2$ to $GdNi_2$. There are also many Gd-3d transition metal ternary compounds that form this same $MgCu_2$-type structure including: $GdFe_{0.2}Mn_{1.8}$[12], $GdFe_{1.6}Mn_{0.4}$[13], GdFeCo, GdNiCo[14], $GdFe_{0.15}Ni_{1.85}$[15], GdCoMn[16], and GdFeCu[17]. GdFeCu is the only ternary that includes a 3d-transition metal, Cu, that does not form the cubic Laves phase with Gd. The lattice parameters for these ternary compounds follow the trend of smaller unit cell volume when substituting a later transition metal into the binary compounds except with GdNiCo, a= 7.286, which is larger than the lattice parameter for either $GdCo_2$ or $GdNi_2$. This trend is not observed in the $GdCo_{2-x}Ga_x$ system: as the Ga content increases the volume/Gd atom increases even when there is no structure change, as in moving from $GdCo_2$ (a=7.256 Å) to $GdCo_{1.67}Ga_{0.33}$(a=7.331 Å).

The crystal structures and preliminary electronic structure calculations, focusing on the fully stoichiometric compounds, were presented in a previous paper.[18] This work takes a deeper look into the mixed site ternary compounds to shed light on the driving force behind the structure changes and to supplement the X-Ray diffraction studies in determining the correct coloring of the atoms in the structure. This is addressed by creating supercells of each

compound that take into consideration the mixed site occupancies and creates a large unit cell that is fully stoichiometric. Calculating the total energy, density of states (DOS), and crystal orbital Hamilton population (COHP) curves can give insights into which geometric coloring is the most electronically stable.[19] The scattering intensity of Co and Ga are similar (Z=27 and Z=31) and this can lead to difficulty in experimentally determining the correct site occupancies. Total energy, DOS and COHP curves are presented for several coloring models for each mixed site ternary to address these questions.

6.3 Electronic Structure Calculations

Electronic structure calculations to obtain total energies were performed using the *Vienna ab Initio Simulation Package* (VASP)[20-21] VASP uses projector augmented- wave (PAW)[22] pseudopotentials treated by the Perdew-Burke-Ernzerhof generalized gradient approximation (PBE-GGA).[23] Integrations of reciprocal space were performed over a 13x13x13 Monkhorst-Pack *k*-point mesh[24] using the linear tetrahedron method.[25] The energy cutoff was set at 500.00 eV for the plane-wave calculations.

Due to the size of the supercells and the length of wall time it would have required to run VASP in order to use the Local Orbital Basis Suite Towards Electronic-Structure Reconstruction (LOBSTER)[26-27] the Stuttgart *Tight-Binding, Linear-Muffin-Tin Orbital* program using the *Atomic Sphere Approximation* (TB-LMTO-ASA)[28] was used to calculate DOS and COHP curves as well as to calculate integrated crystal orbital Hamilton population (ICOHP) values. The *Atomic Sphere Approximation* uses overlapping Wigner-Seitz (WS) spheres around each atom so that the atomic orbital (AO)-like wavefunctions, used as spherical basis functions fill all space. The WS sphere radii used for the various atoms are: Gd 3.259-4.124 Å, Co 2.543-2.717 Å, Ga 2.539-2.725 Å. No empty spheres needed to be added to attain

100% space filling of the unit cells. The exchange-correlation potential was treated with the von Barth-Hedin formulation within the local density approximation (LDA) and the local spin density approximation (LSDA).[29] The basis sets included 6s/(6p)/5d/[5f] for Gd, 4s/4p/4d for Co, and 4s/4p/(4d) for Ga (down-folded orbitals are shown in parentheses and orbitals thrown out of the calculation are shown in brackets). Reciprocal space integrations were performed using *k*-point meshes ranging from 145-793 points, depending on the structure, in the corresponding irreducible wedges of the Brillouin zones.

6.4 Results

The different structures found in the series $GdCo_{2-x}Ga_x$ resemble the structures that are found in the GdX_2 binary compounds (X = Co, Ni, Cu, Zn, Ga). The exceptions are: the hexagonal $MgZn_2$-type Laves phase $GdCo_{1.33}Ga_{0.67}$ crystallizes in and the Pnma structure GdCoGa crystallizes in. As the amount of Ga increases the volume/Gd atom in each structure also increases (see **Figure 6.4.1).** This trend again resembles that of the GdX_2 binary compounds, with an increase in *vec* the structures have an increase in volume/Gd atom, except for the slight decrease in volume/Gd atom moving from the cubic $GdCo_2$ to the cubic $GdNi_2$ compound. These two trends show that the *vec* is playing an essential role in the structure changes as the Ga content increases. **Table 6.4.1** shows the structure type that each value of x crystallizes in along with the interatomic distances seen in each structure.

Table 6.4.1. Structure types and interatomic distances in the series of $GdCo_{2-x}Ga_x$.

	Compound	$GdCo_2$	$GdCo_{1.67}Ga_{0.33}$	$GdCo_{1.33}Ga_{0.67}$	GdCoGa	$GdCo_{0.67}Ga_{1.33}$	$GdCo_{0.33}Ga_{1.67}$	$GdGa_2$
	Structure Type	*Cubic $MgCu_2$-type*	*Cubic $MgCu_2$-type*	*Hexagonal $MgZn_2$-type*	*Orthorhombic SrMgSi-type*	*Orthorhombic $CeCu_2$-type*	*Hexagonal AlB_2-type*	*Hexagonal AlB_2-type*
Bond Distances (Å)	Ga−Ga	–	–	–	–	–	–	2.440
	Co−Ga	–	–	–	2.459-2.549	–	–	–
	Co−Co	2.552	–	–	3.201	–	–	–
	Co/Ga−Co/Ga	–	2.592	2.548	–	2.530-2.758	2.524	–
	Co/Ga−Co	–	–	2.501	–	–	–	
	Co−Gd	2.992	–	2.997	2.807-3.641	–	–	–
	Ga−Gd	–	–	–	3.047-3.179	–	–	3.198
	Co/Ga−Gd	–	3.039	2.910-2.975	–	3.027-3.205	3.113	–
	Gd−Gd	3.125	3.174	3.033-3.118	3.464-3.666	3.614	3.644-4.372	4.134-4.226

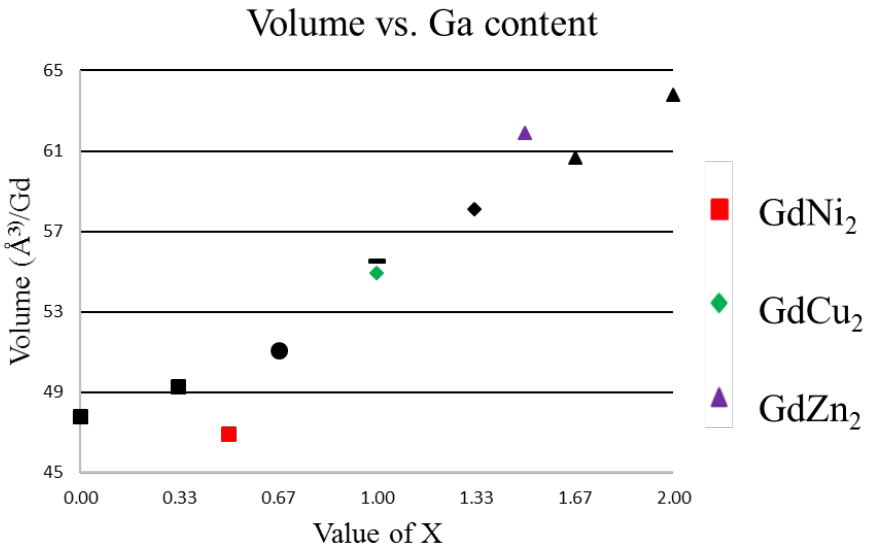

Figure 6.4.1. Volume vs Ga content in the series $GdCo_{2-x}Ga_x$ and the volume of the binary GdX_2 compounds (X = Ni, Cu, Zn). Squares, circle, rectangle, diamonds, and triangles represent the $MgCu_2$, $MgZn_2$, SrMgSi, $CeCu_2$ and AlB_2 structures types, respectively.

6.4.1 $GdCo_{1.67}Ga_{0.33}$

$GdCo_{1.67}Ga_{0.33}$ crystalizes in the $MgCu_2$-type structure. The 16d site is mixed between Co and Ga with Co occupying the site 83.3% of the time. The DOS for calculated for $GdCo_2$ can be informative when trying to understand the electronic stability of this mixed site ternary compound. The spin polarized DOS indicates that $GdCo_2$ crystallizing in the cubic $MgCu_2$-type structure is electronically stable. The Fermi level falls in a pseudogap opened by spin polarization in the DOS and also falls in an area of optimized non-bonding Co−Co interactions in the COHP curve. The Co−Co interactions dominate the total percent of the integrated COHP with 49.39% with only 6 bonds/f.u. compared with the Gd−Co interactions at 45.78% and 12 bonds/f.u. and Gd−Gd interactions at 4.83% and 2 bonds/f.u. Zegaou et. al[30] have previously shown that the magnetic moments of Co are oriented oppositely to that of the Gd magnetic moments therefore all calculations were performed in a ferrimagnetic ordering.

Since both compounds crystalize in the same structure and are close in valence electron count (VEC), the rigid band approximation can be used to shed light on the electronic stability of the mixed site ternary. The electron count for $GdCo_{1.67}Ga_{0.33}$ is calculated as 22.32 eV/f.u. and resides in a pseudogap of the DOS for $GdCo_2$ and a pseudogap of Co-Co anti-bond interactions found in the COHP for $GdCo_2$. This indicates that the mixed site ternary compound is stable in the $MgCu_2$-type structure. While using the rigid band model Ga is counted as 13 electrons as Ga is replacing Co. In the calculation Co brings 3*d* electrons and to be consistent with the basis functions Ga is counted including the filled 3*d* electrons thus counting as 13. The VEC for the Compound $GdCo_{1.67}Ga_{0.33}$ is also shown on the DOS and is at an energy of ~ 1 eV. This falls on a large population of states and is an indicator that this VEC is not

electronically stable in the cubic Laves phase structure. However, there are limits to the rigid band approximation and moving 1 eV in energy is a large comparison to be made.

The electron count of $GdCo_{1.33}Ga_{0.67}$ is 23.68 eV/f.u. which is above the electron count of $GdNi_2$ at 23. Binary compounds with Gd and late 3d transition metals change structures from the cubic Laves phase to orthorhombic in $GdCu_2$. This structure change happens between the VEC of 23 and 25 which gives an indication that the cubic Laves phase structure might not be stable above 23 VEC. This is evidenced by the structure change between $GdCo_{1.67}Ga_{0.33}$ and $GdCo_{1.33}Ga_{0.67}$. The DOS and COHP for $GdCo_2$ are shown in **Figure 6.4.2.** In the $MgCu_2$-type structure all T sites are equivalent and any Ga−Ga contacts can be avoided for x less than 0.50. When moving to higher Ga content than x = 0.50 there is no way to avoid Ga−Ga interactions in the cubic structure which can be another electronic factor driving the structure change between x = 0.33 and x = 0.67.

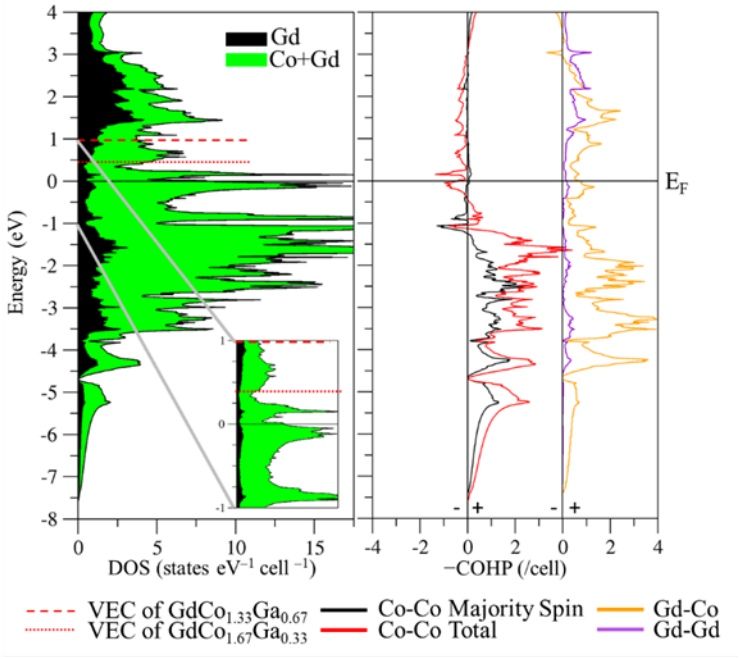

Figure 6.4.2. DOS for $GdCo_2$ showing electron counts of $GdCo_{1.67}Ga_{0.33}$ and $GdCo_{1.33}Ga_{0.67}$.

6.4.2. $GdCo_{1.33}Ga_{0.67}$

$GdCo_{1.33}Ga_{0.67}$ crystalizes in the $MgZn_2$-type structure. Gd sits in the 4f Wycoff position and Co sits in the 2a position. The 6h position is mixed between Co and Ga with 55.5 and 44.4% occupancies respectively. Experimentally the structure was refined by only letting the 6h site mix. This was done do to the similar scattering factors of Co and Ga and because mixing only on the 6h site has been reported for the GdCoAl system.[31] The Gd coordination environment is a distorted Frank-Kasper sphere as seen in many of the Laves phases.[32] The Co in the 2a site have a coordination environment of 6 to the mixed Co/Ga atoms while the Co/Ga mixed site also has a coordination of 6, 4 to other mixed site atoms and two to Co. To determine if the assumption that mixing only occurs at the 6h site is valid, four different "coloring" models were made by tripling the unit cell in the c direction. Two of these models only have mixing on the 6h site while two of them have mixing on both the 2a and 6h positions. The models are shown in **Figure 6.4.3.**

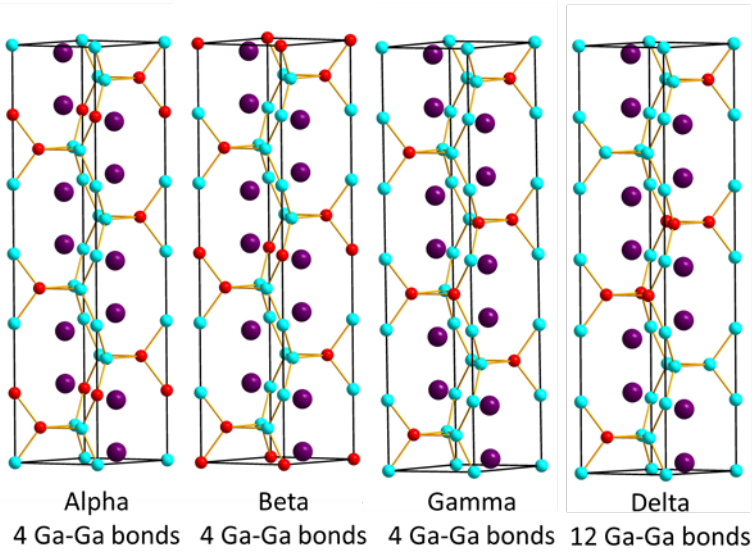

Figure 6.4.3. Coloring models for $GdCo_{1.33}Ga_{0.67}$.

Three of the models have the same number of Ga-Ga interactions however, the last model, named delta, contains three times as many as the other models. The model delta is made by placing the Ga atoms in the Kagomé nets that are present in the Laves phases in a way that retains the vertical mirror plane. **Table 6.4.2** shows the total energies calculated for each model. The highest energy model contains the Ga in the Kagomé nets while retaining the vertical mirror plane. The first three models are very close in energy while the last model is ~10 meV/f.u. higher in energy compared to the other three.

Table 6.4.2. Total energy for $GdCo_{1.33}Ga_{0.67}$ coloring models.

Model	Energy meV/f.u.
Alpha	0
Beta	+1.00
Gamma	+11.0
Delta	+108

Experimentally the two higher energy models are favored if there is no mixing on the 2a site. However, in a neutron diffraction study performed on $HoCo_{1.33}Ga_{0.67}$ indicated that the Ga mixes on both the 2a and 6h sites. The Ga and Co prefer the 2a and 6h sites, respectively. In the Ho and isostructural Er compound the occupancies were refined as 0.46/0.54(2) Co/Ga for the 2a site and 0.74/0.26(2) Co/Ga for the 6h site.[2] This might be explained by looking at the DOS for the alpha and delta models which are shown in **Figure 6.4.4.** The Fermi level for the lowest energy model resides on the base of a large sharp peak in the DOS while the Fermi level for the highest model still occurs on an area of the DOS that has a lot of states however, now it falls in between two larger peaks. However, no models created thus far have the same mixing as that found in the Ho and Er compounds thus more calculations should be performed in order to achieve the most accurate coloring model.

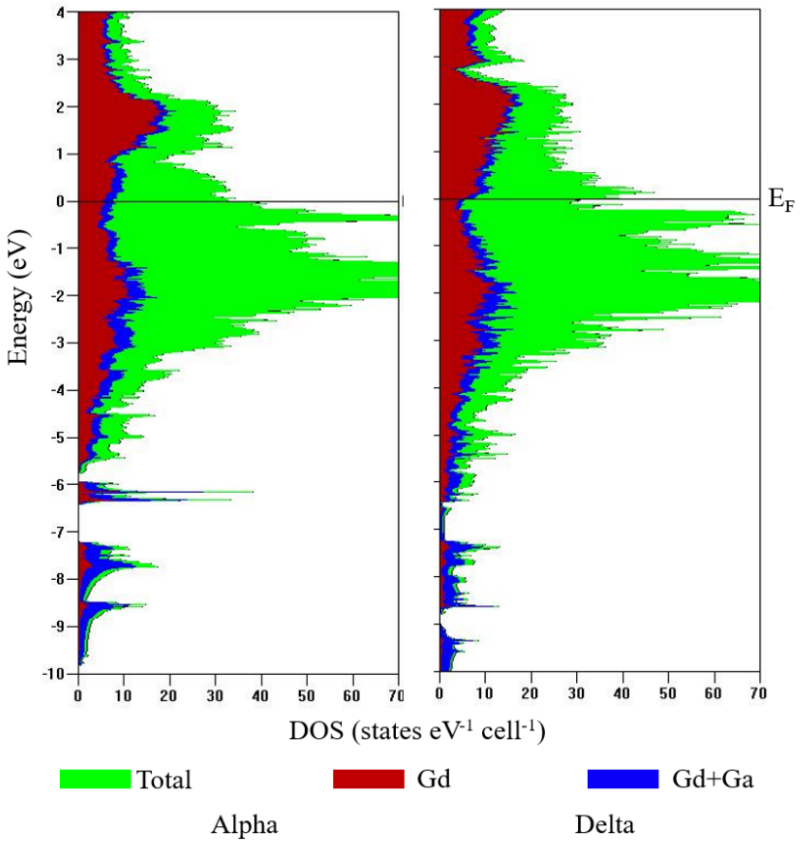

Figure 6.4.4. DOS of the lowest (left) and highest (right) energy coloring model for $GdCo_{1.33}Ga_{0.67}$.

6.4.3. GdCoGa

GdCoGa crystalizes in the SrMgSi-type structure in space group Pnma that contains no nearest neighbor Co−Co or Ga−Ga interactions. The Co−Ga interactions dominate the % total ICOHP at 42.16% with Gd−Co and Gd−Ga contributing essentially equally at 27.39% and 26.54% respectively. The VASP optimization, letting all parameters relax, of the GdCoGa experimental compound resulted in a shorter by ~3.7% *c* lattice parameter compared to experimental results. This could indicate disorder at the Co and Ga sites or a slight Ga rich non-stoichiometric experimental compound with Ga−Ga homoatomic interactions that are increasing the *c* lattice parameter compared to the computationally optimized value.

6.4.4. $GdCo_{0.67}Ga_{1.33}$

$GdCo_{0.67}Ga_{1.33}$ crystalizes in the $CeCu_2$-type structure in space group Imma. Gd sits in the 4e Wycoff position with the 8h position being mixed between Co and Ga, Ga occupying the site 2/3 of the time while Co occupies it 1/3 of the time. In this structure, there are zig-zag chains of 4 membered mixed Co/Ga rings along the *a* direction. The Co/Ga mixed site has a coordination of 4 to other Co/Ga atoms and a coordination of 6 to Gd.

Pnma is a maximal *klassengleiche* subgroup of the *Imma* space group that takes the 8-fold (h) Wycoff site and splits it into 2 4(c) sites. To change from the 8(h) site to 2 4(c) sites the lattice parameters a and b and the positional parameters x and y must be interchanged along with a shift of the origin. Specifically the SrMgSi-type structure that GdCoGa crystallizes in is considered an ordered ternary variant of the $CeCu_2$-type structure that $GdCo_{0.67}Ga_{1.33}$ crystallizes in.[33] The four-connected Gd−Co net has lower symmetry in *Pnma* due to the splitting of the 8(h) site and there are two different $CoGa_4$ and Co_4Ga distorted tetrahedra in the SrMgSi structure type compared to only one type of tetrahedra present in the $CeCu_2$-type structure.[33] The restraint that two of the bond angles present in the tetrahedra must be 90° is also lost due to the lowering in symmetry moving from *Imma* to *Pnma*.

To account for the mixed position a supercell was created by expanding the unit cell to 3 x *c*. Three different "coloring" models were made by switching the Ga and Co positions and are shown in **Figure 6.4.5** along with the arbitrary names of the Greek alphabet given to them.

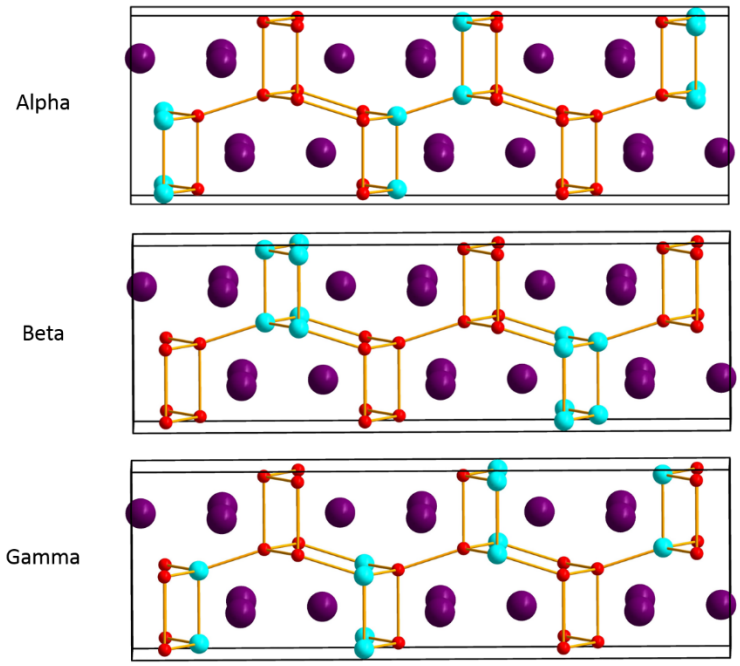

Figure 6.4.5. Three coloring models made to account for mixed site occupancy in $GdCo_{0.67}Ga_{1.33}$.

The alpha model also has two rows of chains made up of only Ga however, the way that the alternating Co/Ga chains are laid out introduces more Co-Co interactions into the structure. Beta, has only chains that are made up of all Ga or all Co. The last model, gamma, has two "rows" of zig-zag chains that are entirely made of Ga and four chains that are alternating Ga and Co. **Table 6.4.3** show the total energy for each model and the number of each type of bond present. The contribution of each type of interaction to the overall COHP for each model can be seen in **Table 6.4.4**. Gamma, the lowest energy model, has the lowest contribution of Co-Co and Ga-Ga interactions while maximizing the Co-Ga interactions.

Table 6.4.3. Total energy and number of interactions in each of the three supercell models.

Model	Total Energy meV/f.u.	# Co-Co Interactions	# Co-Ga Interactions	# Ga-Ga Interactions
Alpha	+142	8	16	24
Beta	+250	12	8	28
Gamma	0	4	24	20

Table 6.4.4. Contributions of individual interactions to the overall ICOHP for the $GdCo_{0.67}Ga_{1.33}$ coloring models.

	% Total ICOHP		
	Alpha	Beta	Gamma
Gd-Gd	4.17	4.31	3.93
Gd-Ga	36.62	37.26	36.00
Gd-Co	17.67	16.87	18.58
Co-Co	5.60	8.49	2.34
Co-Ga	14.69	7.12	22.44
Ga-Ga	21.25	25.95	16.71

The model Gamma, which contains the fewest homoatomic interactions has the lowest energy. A comparison of the total energy of all three models shows the energy goes down as the number of homoatomic interactions goes down. The DOS for the models are shown in **Figure 6.4.6**. In the DOS for gamma the Fermi level resides on the side of a large peak consisting mostly of Co d states. The DOS for the beta model shows a deep pseudogap at ~ -0.5 eV, seeming to split the Co d band into two sections with 2/3 below the pseudogap and 1/3 above. The Fermi level falls on a large peak of Co d states for the beta model, which is the highest in energy.

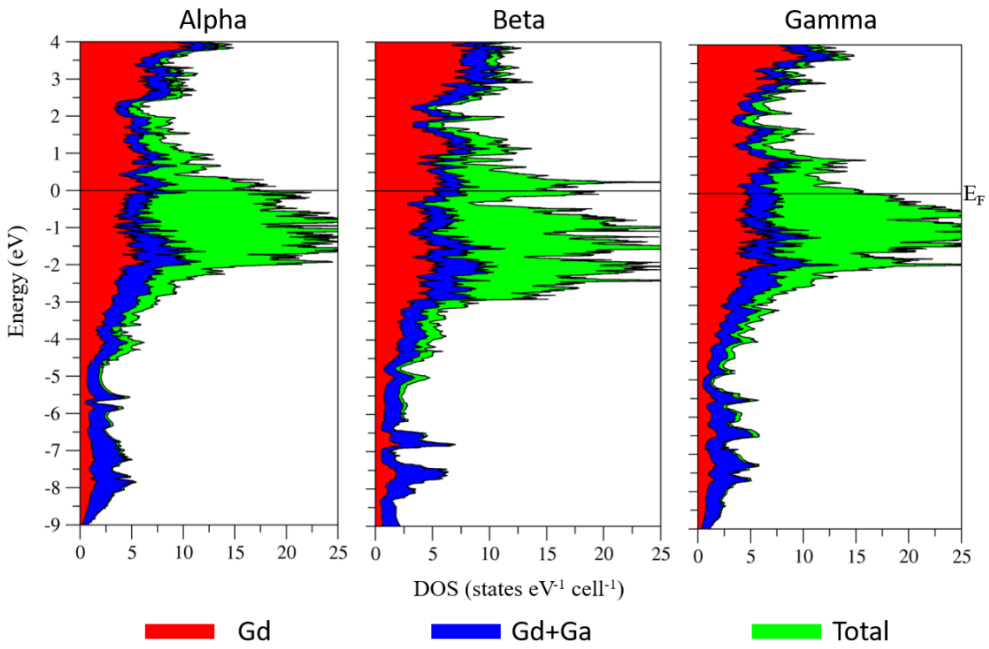

Figure 6.4.6. DOS curves for the coloring models labeled as alpha (left), beta (middle), and gamma (right).

The COHP curves for each model are displayed in **Figure 6.4.7** and give some insights into why the beta model is the highest in energy. There is a large peak of anti-bonding states coming from the Co-Co interactions near the Fermi level in the curve. The COHP curves for the alpha and gamma model differ mainly in the Gd-Gd interactions. In the gamma model the Gd-Gd inactions are optimized as almost nonbonding at the Fermi level whereas the Gd-Gd interactions in the alpha model show strong bonding character at the Fermi level.

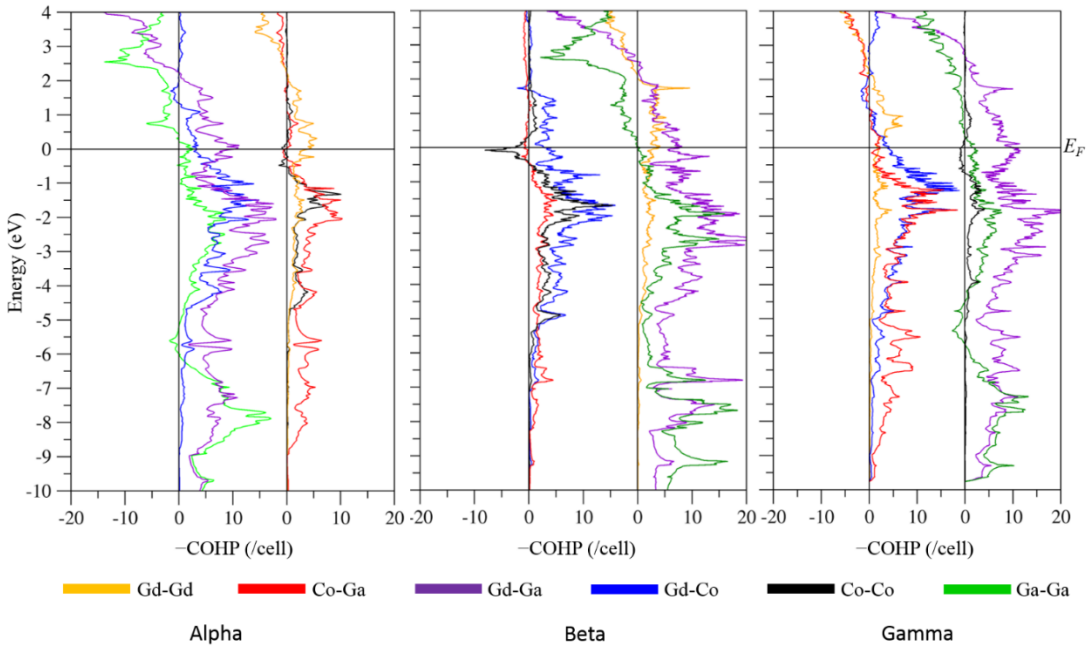

Figure 6.4.7. −COHP curves for the three coloring models of $GdCo_{0.67}Ga_{1.33}$. +/- indicate bonding/anti-bonding values of COHP curves.

6.4.5. $GdCo_{0.33}Ga_{1.67}$

$GdCo_{0.33}Ga_{1.67}$ adopts the AlB_2 structure type and is isostructural to $GdGa_2$. $GdGa_2$ crystallizes in the AlB_2-type structure with graphene-like sheets of Ga. The DOS of $GdGa_2$ shows a local minimum at ~ 9.9 e^-/f.u. which also corresponds to the electron count that all interactions in $GdGa_2$ switch from bonding to anti-bonding, especially the Ga−Ga interactions, thus indicating that above this electron count the sheets of Ga are no longer stable. The Gd−Ga interactions dominate the total contribution from the ICOHP at 56.28%, partially due to having 12 bonds/f.u. The Ga−Ga interactions contribute 38.40% however, there are only 3 bonds/f.u and lastly the Gd−Gd only contribute 5.32% with 4 bonds/f.u. As discussed previously using a rigid band model for this compound is not appropriate due to the Co atoms introducing valence 3*d* orbitals to the energy region near the Fermi level.[18]

A better approach to performing electronic structure calculations on $GdCo_{0.33}Ga_{1.6}$ is to create a supercell with the approximate formula Gd_3CoGa_5. The AlB_2 structure type has graphene-like sheets of Ga atoms and with this formula one in every six Ga atoms are being substituted by Co. By replacing one in every six Ga an ordered model of each layer of Ga/Co atoms can be made. A new expanded unit cell can be made from these layers. There are two possible models that can be made using these new Ga/Co sheets. The sheets can be stacked so that the Co atoms are directly on top of each other, thus requiring only two sheets to make a unit cell. The second option is to have the sheets be offset, which is achieved by having three sheets with the top and bottom layers directly on top of each other but the middle shifted. **Figure 6.4.8** shows the making of these two new unit cells and **Figure 6.4.9** shows the DOS and COHP curves calculated for the two models. The stacking to decrease Co−Co interactions was motivated by the results seen in $GdCo_{0.67}Ga_{1.33}$ calculations that indicated the structure with the most heteo-atomic interactions had the lowest energy. The model with only 4 Co−Co interactions was lower in energy by 142 meV/f.u. compared to the model with 8 Co−Co interactions and lower in energy by 250 meV/f.u. compared to the model with 12 Co−Co interactions.

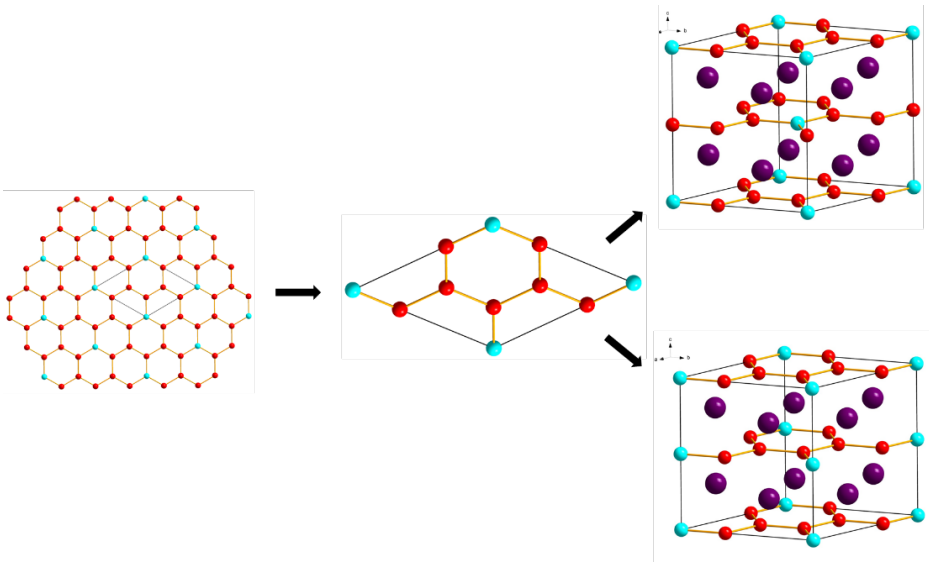

Figure 6.4.8. Creation of two $Gd_6Co_2Ga_{10}$ models with stacking sequence aba (top) and aaa (bottom).

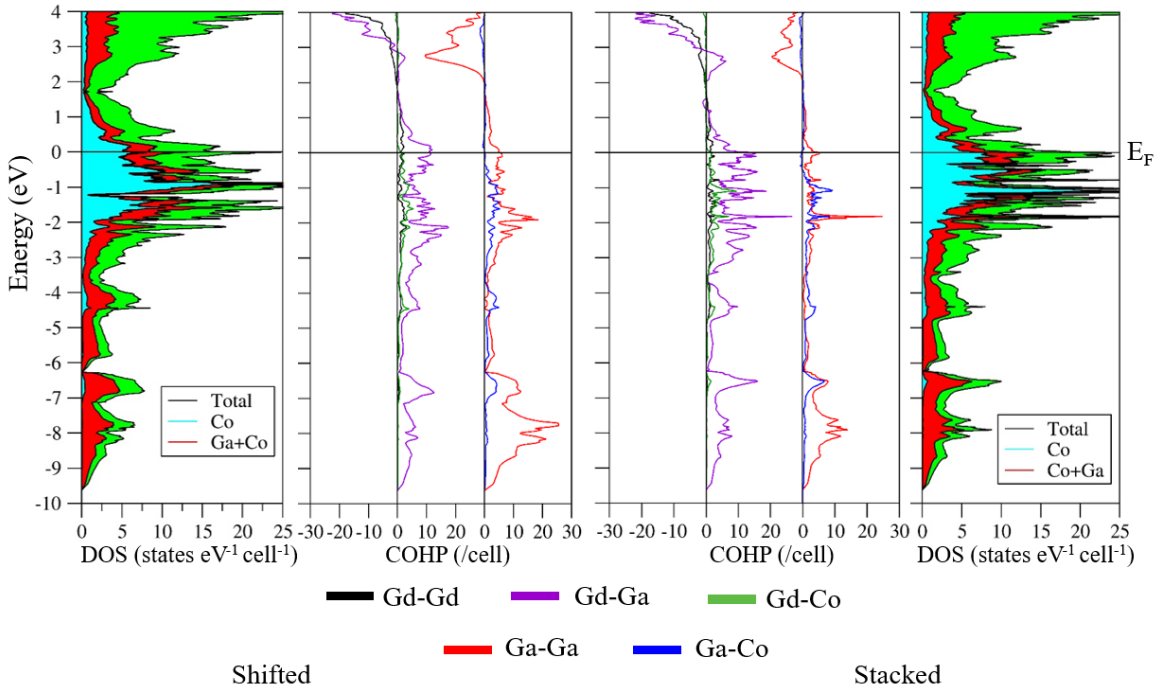

Figure 6.4.9. DOS and COHP for Shifted (left) and Stacked (right) coloring models.

Total energy calculations show the model with aba stacking is lower in energy by 598 meV/f.u. compared to the model with aaa stacking. The aba stacking has the nearest neighbor Co-Co distance of 4.801Å while the aaa stacking has a shorter distance of 4.134 Å. The DOS

for the shifted model shows the Fermi level resides at the very edge of a sharp peak whereas the Fermi level for the stacked model resides on the tip of a broad peak. The DOS for the shifted model has a deep pseudogap, almost going to 0 states, at -1.226 eV which corresponds to 22 e^-/f.u., two-thirds of the total number of electrons at E_F. States arising from Co in the stacked model do not have this deep pseudogap but instead are "split," into three different sections by smaller pseudogaps at -0.902 and -0.328 eV. DOS curves for both models show the wide local minimum in the anti-bonding states that is present in the DOS for $GdGa_2$.[18] At the same energy as this local minimum the Ga-Ga interactions transition from non-bonding to significantly anti-bonding, with the interactions from the shifted model having a larger anti-bonding peak compared to the Ga-Ga interaction in the stacked model. The Ga-Co interactions in the stacked model however move from positive to negative at -0.501 eV while those interactions in the shifted model remain positive until above the Fermi level.

Table 6.4.5. ICOHP percentages for $GdGa_2$, shifted and stacked coloring models.

$GdGa_2$			Shifted			Stacked		
Ga-Ga	Gd-Ga	Gd-Gd	Ga-M	Gd-M	Gd-Gd	Ga-M	Gd-M	Gd-Gd
38.18%	56.09%	5.73%	37.815	56.72%	5.47%	37.76%	56.89%	5.34%

Calculated integrated crystal orbital Hamilton population values show that the overall percent of each type of interaction does not change significantly between $GdGa_2$, and the two different coloring models for Gd_2CoGa_5. The Ga-M (M=Ga, Co) interactions contribute a similar total percentage of the overall ICOHP and the Ga-Ga interactions do in $GdGa_2$. The total percentages of each type of bond for the models can be found in **Table 6.4.5.**

6.5 Conclusions

With increased Ga added into the $GdCo_2$-$GdGa_2$ system the structures change from cubic to hexagonal to orthorhombic and finally back to the hexagonal AlB_2 structure type. The compounds transition from cluster-based structures to 3D networks and finally to 2D networks

with increasing Ga content. A major driving force causing these structural changes is the increase of valence electron count. Adding increased amounts of Ga is a way to titrant more electrons into the system and due to this increase the structures change and shift from the closer packed Laves phase type $GdCo_2$ to the more open Zintl phase like $GdGa_2$. This driving force is evidenced by comparing the structure changes seen in the $GdCo_{2-x}Ga_x$ series with those of the GdX_2 (X= Co, Ni, Cu, Zn, Ga) binary compounds. As the valence electron count is increased in the $GdCo_{2-x}Ga_x$ system the structural procession resembles the same structural changes found in the binary compounds as the valence electron count is increased. Another subtle driving force for these structural changes is the avoidance of Ga−Ga near neighbor contacts for Co-rich compounds and possibly the avoidance of Co−Co near neighbor contacts for Ga-rich cases. The coloring models employed in this study indicate in all cases that the lowest calculated energy models contain the fewest Ga-Ga and Co-Co homoatomic interactions while optimizing the Co−Ga interactions. This series of compounds follow the same structural trend as evidenced in the $DyCo_{2-x}Ga_x$ system however, in the Dy system the compounds are all reported with phase widths.

6.6 Acknowledgements

This research was supported by the Office of the Basic Energy Sciences, Materials Sciences Division, U.S. Department of Energy (DOE). The Ames Laboratory is operated by Iowa State University under Contract No. DE-AC02-07C. Computations were performed on the CRUNCH cluster supported by Iowa State University Computation Advisory Committee under Project No. 202-17-10-08-0005.

6.7 References

1. Liu, F.; Ao, W.; Wu, L.; Li, J. Crystal Structures of the compounds formed in $DyCo_2$–$DyGa_2$ pseudo-binary system at 773K. *Intermetallics.* **2009**, *17*, 738-743.

2. Yuan, F.; Greedan, J.E.; Boyer, C.; Mozharivskyj, Y. A neutron diffraction study of the hexagonal Laves phases, $Ho(Co_{0.667}Ga_{0.333})_2$ and $Er(Co_{0.667}Ga_{0.333})_2$: Co/Ga site preferences and magnetic structure. *Journal of Solid State Chemistry.* **2018**, *257,* 1-8.

3. Harris, I.R.; Mansey, R.C.; Raynor G.V. Rare earth intermediate phases: III. The cubic laves phases formed with aluminium and cobalt. *Journal of the Less Common Metals*. **1965**, *9,* 270-280.

4. Duc, N.H.; Hien, T.D.; Brommer, P.E.; Franse, J.J.M. The magnetic behavior of rare-earth–transition metal compounds. *Journal of Magnetism and Magnetic Materials*. **1992**, 1252-1256.

5. Khmelevskyi, S.; Mohn, P. The order of the magnetic phase transitions in RCo_2 (R = rare earth) intermetallic compounds. *Journal of Physics: Condensed Matter*. **2000**, *12(45)*, 9453-9464.

6. Chelkowska G.; Debiec, I. Electronic structure and magnetic properties of $Gd(Co_{1-x}M_x)_2$ compounds, M = Ga, Si, Ge. *J. Alloys Compd*. **2002**, *337*, 39-43.

7. Ouyang Z.W.; Rao G.H.; Yang, H.F.; Liu, W.F.; Liu G.Y.; Feng, X.M. et al. Structure and magnetic phase transition in $R(Co_{1-x}Ga_x)_2$ (R = Nd, Gd, Tb, Dy) compounds. *Physica B*. **2004**, *344,* 436-42.

8. Ao, W.Q.; Li, J.Q.; Liu, F.S.; Jian, Y.X. Magnetocaloric properties of $DyCo_{2-x}Ga_x$ alloys. *Solid State Commun.* **2007**, *141,* 219-22.

9. Slebarski, A. Magnetic and structural investigations of $DyCo_2$ $DyAl_2$ and $GdMn_2$ – $GdAl_2$ compounds. *Journal of the Less-Common Metals* **1980**, *72*, 231-240.

10. Endter, F.; Klemm, W. Die Kristallstrukturen von Fe2Gd und Mn2Gd. *Zeitschrift fuer Anorganische und Allgemeine Chemie.* **1950**, *252*, 377.

11. Nassau, K.; Cherry, L.V.; Wallace, W.E. Intermetallic compounds between lanthanons and transition metals of the first long period I – preparation, existence and structural studies. *Journal of Physics and Chemistry of Solids.* **1960**, *16*, 123-130.

12. Nagai, H.; Oyama, N.; Ikami, Y.; Yoshie, H.; Tsujimura, A. The magnetic properties of pseudo-binary compound of $Gd(Fe_{1-x}Mn_x)_2$ and $Gd_6(Fe_{1-y}Mn_y)_{23}$. *Journal of the Physical Society of Japan.* **1986**, *55(1),* 177-183.

13. Ilyushin, A.S.; Wallace, W.E. Magnetic and structural studies of rare earth-iron-manganese Laves phase ternaries II. *Journal of Solid State Chemistry*. **1966**, *17,* 373-376.

14. Sobczak, R. Magnetische Messungen in den Mischphasen (M1, M2) (Si, Ge); (M1, M2 = Fe, Co, Ni). *Monatshefte fuer Chemie.* **1975**, *106*, 1389-1395.

15. Kotur, B.; Myakush, O.; Zavaliy, I. Hydrogen sorption properties of some R M(2-x) M'(x) and R M(2-x) Al(x) (R = Y, Gd, Tb, Er, Ho; M = Mn, Fe, Co, Ni) laves phase ternary compounds. *Croatica Chemica Acta*, **2009**, *82(2),* 469-476.

16. Mikihara, Y.; Fujii, H.; Kiraoka, K.; Nagata, H.; Hihara, T. Magnetic phase transitions in the Gd $(Mn_{1-x}Co_x)_2$ system. *Journal of Magnetism and Magnetic Materials*, **1991**, *96,* 305-314.

17. Tsvyashchenko, A.V.; Fomicheva, L.N. High pressure synthesis of the rare earth compounds R Fe Cu with the Laves phase structure. *Journal of the Less-Common Metals,* **1985**, *105,* 1-3.

18. Yuan, F.; Toombs, A.; Miller, G.J.; Mozharivskyj, Y. $Gd(Co_{1-x}Ga_x)_2$: Synthesis, crystal structures, and investigation of structural transformations and magnetic properties. *Journal of Solid State Chemistry,* **2018**, *264*, 68-76.

19. Burdett, J.K.; Canadell, E.; Hughbanks, T. Symmetry control of the coloring problem: The electronic structure of MB2C2 (M = Ca, La, …). *J. Am. Chem. Soc.* **1986**, *108,* 3971-3976.

20. Kresse, G.; Hafner, *Ab initio* molecular dynamics for liquid metals. *Phys. Rev. B,* **1993**, *47*, 558.

21. Kresse, G.; Furthmüller, J. Efficient iterative schemes for *ab initio* total-energy calculations using a plane-wave basis set. *Phys. Rev. B.* **1996**, *54(23),* 16533-16539.

22. Blöchl, P.E.; Projector augmented-wave method. *Phys. Rev. B* **1994**, *50(24),* 17953-17979.

23. Perdew, J.P.; Burke, K.; Wang, Y. Gerneralized gradient approximation for the exchange-correlation hole of a many-electron system. Phys. Rev. B 1996, 54(23), 16533-16539.

24. Monkhorst, H. J.; Pack, J. D. Special points for Brillouin-zone integrations. Phys. Rev. B 1976, 13, 5188.

25. Blöchl, P. E.; Jepsen, O.; Andersen, O. K. Improved tetrahedron method for Brillouin-zone integrations. Phys. Rev. B 1994, 49(23), 16223-33.

26. Dronskowski, R.; Blöchl, P.E. Crystal orbital Hamilton populations (COHP): energy-resolved visualization of chemical bonding in solids based on density-functional calculations, J. Phys. Chem. 1993, 97, 8617–8624.

27. Deringer, V.L.; Tchougréeff, A.L.; Dronskowski, R. Crystal orbital Hamilton population (COHP) analysis as projected from plane-wave basis sets, J. Phys. Chem. A. 2011, 115.

28. Jepsen, O.; Andersen, O.K. TB-LMTO, version 47; Max-Planck-Institut für Festkörperforshcung: Stuttgart, Germany, 2000.

29. Von Barth, U.; Hedin, L. Local exchange-correlation potential for the spin-polarized case. J. Phys. C 1972, 5, 1629

30. Zegaou, B.; Benkhettou, N.; Rahed, D.; Reshak, A.H.; Benalia, S. Electronic structure of GdX2 (X = Fe, Co, Ni) intermetallic compounds studied by the GA+U method, Comput. Mater. Sci. 2014, 87, 172-177.

31. Oesterreicher, H.; Wallace, W.E. Studies of pseudo-binary Laves phase systems containing lanthanides. I. Constitution and magnetic properties of the GdAl2-GdFe2, GdAl2-GdCo2 and ErCo2-ErAl2 systems. Journal of the Less-Common Metals, 1967, 13, 91-102.

32. Doverbratt, I.; Ponou, S.; Lidin, S. Ca2Pd3Ge, A new fully ordered ternary Laves phases structure. Journal of Solid State Chem. 2013, 197, 312-316.

33. Nuspl, G.; Polborn, K.; Evers, J.; Landrum, G.A.; Hoffmann, R. The Four-Connected Net in the CeCu2 Structure and Its Ternary Derivatives. Its Electronic and Structural Properties, Inorg. Chem. 1996, 35, 6922-6932.

CHAPTER 7. CONCLUSIONS

The work presented in this thesis focuses on the synthesis, characterization, and electronic structure calculations of Ga containing polar intermetallic compounds. Initial work focused on compounds containing the transition metal Pt, which has the second most relativistic contraction of the 6s orbital, second only to Au. Pt also has a large electronegativity compared to other transition metals second again only to Au. Previous work in the Miller group has focused on Au containing compounds and the goal of this work was to investigate if the structure versatility seen previously with Au is present with Pt. Ga has a larger metallic radius than Pt but a lower Mulliken electronegativity, which can affect the amount of charge transfer in Pt polar intermetallics. Different alkaline earth (Mg, Ca, Sr) cations were used to determine the effect of cation size on crystal structures of Pt−Ga compounds.

Substitution of Ga for Pt into the cubic Laves phase $CaPt_2$ shows that with the addition of Ga the cubic structure is rhombohedrally distorted by expansion along a single body diagonal. Comparable results had been previously reported in the Ca−Pd system with the substitution of Ge into the structure. To investigate the versatility in *vec* of this rhombohedral structure the compound Ca_2Pd_3Ga was targeted and successfully synthesized. Powder patterns showed that the Pd compound formed as a pure phase while the Pt compound formed only as a triphasic mixture. Energy calculations showed that the substitution of Ga for Pt, with no structure distortion, was energetically unfavorable whereas the same substitution of Ga for Pd was energetically favorable. This difference is a major contributor to the difference in stabilities between these two compounds. Electronic structure calculations showed that the cubic structure distorts rhombohedrally to optimize the number of hetero-atomic interactions present. The rhombohedral structure, compared to other coloring models proposed, contains

no Ga−Ga nearest neighbor interactions and has the largest second nearest neighbor distance between Ga atoms.

During the process to synthesize the Ca_2Pd_3Ga compound an additional compound Ca_2Pd_2Ga was discovered. Previously reported as a monoclinic structure the as synthesized Ca_2Pd_2Ga crystallized in an orthorhombic space group (Cmca) that contains the monoclinic space group (C2/c) as a subgroup. Electronic structure calculations show that the monoclinic structure is favored thus indicating that the orthorhombic variant might be a metastable structure obtained via faster cooling compared to previous methods use to obtain the monoclinic Ca_2Pd_2Ga compound.

A theoretical investigation of the $GdCo_{2-x}Ga_x$ (x = 0, 0.33, 0.67, 1, 1.33, 1.67, 2) was undertaken as a collaboration with Fang Yuan and Yurij Mozharivskyj at McMaster University. Fang synthesized and characterized the compounds and wanted an in-depth computational analysis of the driving forces causing the structure changes. Initial calculations on the fully stoichiometric beginning, middle, and end points (x = 0, 1, 2) showed the relative stability of the ternary compound compared with the constituent elements and binary compounds. However, the computationally optimized GdCoGa structure showed a significant shrinkage of the *c* lattice parameter compared to the experimental results. This shrinking of the theoretical model compared to the experimentally determined structure can be an indicator that the experimentally synthesized compound possibly has disorder on the Co and Ga sites or is a non-stoichiometric compound that is slightly Ga rich. Disorder or being Ga rich would introduce Ga−Ga homoatomic interactions in the experimental structure that could lengthen the *c* parameter compared to the calculated value. Analysis by way of the rigid-band model was successful for the x=0.33 compound but failed in the case of x=1.67. If the rigid-band

approximation is used the basis set for the original calculation must be considered, which can lead to counting valence electrons in an unconventional way. In the case of x=1.67 the calculation to provide the DOS and COHP curves for $GdGa_2$ do not include the Ga 3*d* orbitals and thus to be consistent Co is counted as -1 e^- in the rigid-band approximation. Co is counted as -1 as the nearly filled 3*d* band in Co will want to take one electron to be filled. Thus, a more in-depth approach of creating super-cells with different atomic colorings that contain no mixed sites must be taken for the other mixed site ternary compounds.

Total energy, DOS, and COHP for several coloring models proposed for the mixed site ternaries were analyzed and yielded comparable results in each case. The lowest energy models generally had the fewest Ga−Ga interactions and optimized the hetero-atomic Co−Ga interactions. The structure changes coincide very closely with the structures observed in the series of GdX_2 (X = Co, Ni, Cu, Zn, Ga) binary compounds. The only exception is the hexagonal $MgZn_2$-type structure that $GdCo_{1.33}Ga_{0.67}$ crystallizes in is not found in the binary series. This demonstrates the large effect the valence electron count plays in this series of structures.

A major driving force for any structural changes with Ga containing polar intermetallics is the number and distances of Ga−Ga homoatomic interactions. Structures containing Ga are optimized when the number of hetero-atomic interactions are optimized and when the Ga atoms have the largest distance between them within the crystal structure. If Ga is being substituted into another structure, as in the case of Ca_2Pt_3Ga or $GdCo_{2-x}Ga_x$, the structures can maintain shape and connectivities until the number of Ga−Ga interactions becomes too high and then the structure will distort or change in order to lower the number of Ga−Ga homoatomic interactions. The cubic Laves phases Ca_2Pt_3Ga and Ca_2Pd_3Ga distort

rhombohedrally in an effort to spread the Ga atoms further apart. The series of compounds found in $GdCo_{2-x}Ga_x$ shift from the cluster based structure when x=0 to the 3D network based structure of x=1 and finally to the 2D network in the Zintl-like x=2 compound. These structure transitions are driven both by the change in valence electron count and the number of Ga−Ga homoatomic interactions, an effect frequently observed in intermetallic compounds.

The work presented in this thesis focused on the effects of substituting Ga in Pt, Pd, and Co containing polar intermetallics. This substitution was performed to study how structures react to the change in valence electron count and the changing electronegativities of the anionic lattice. Future work can study the effect of changing the size of the cations involved without changing the valence electron counts. This work could focus on studying the effects that substituting the smaller more electronegative and polarizing Mg with the larger less electronegative polarizable Sr can have on structures. This substitution would shed light on any subtle structural effects that changing the size of the cation within a structure can have and a way to tune the charge transfer within the polar intermetallic compound due to the differences in Mulliken electronegativities of Mg, Ca, and Sr.

APPENDIX A. SUPPORTING INFROMATION FOR CHAPTER 3

Rhombohedral Distortion of the Cubic $MgCu_2$-Type Structure in Ca_2Pt_3Ga and Ca_2Pd_3Ga

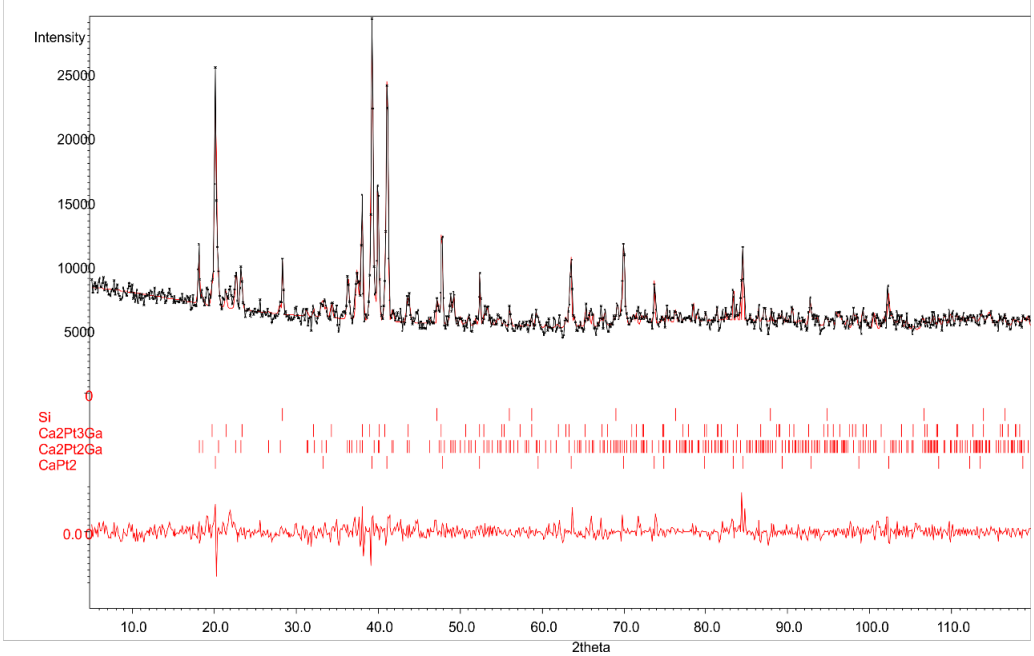

Figure S1. Peak fitting performed with Jana. Relative percentages of compounds are $CaPt_2$ (50%), Ca_2Pt_2Ga (30%), Ca_2Pt_3Ga (15%), and Si (5%).

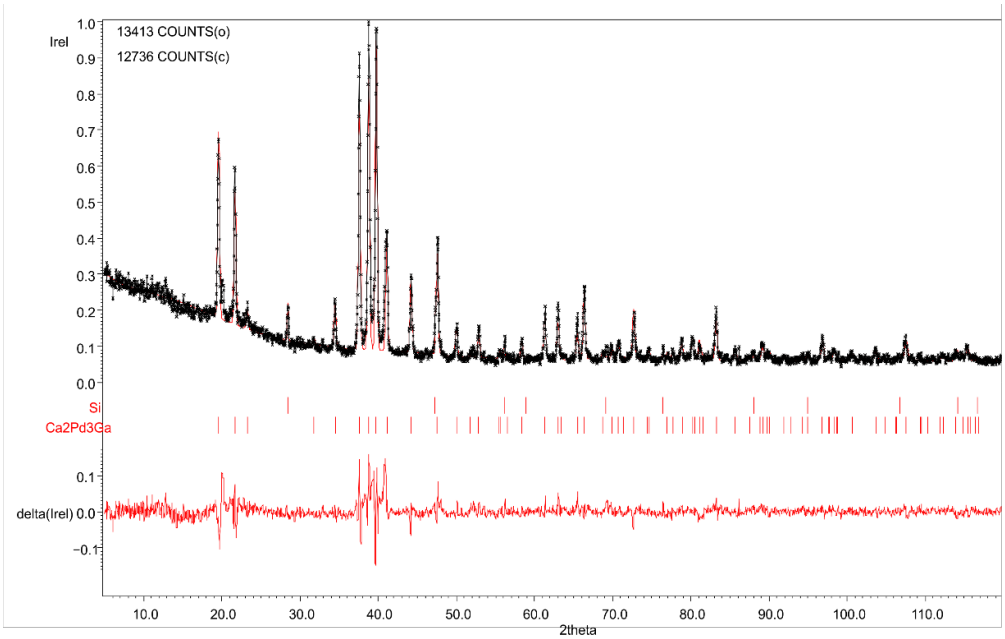

Figure S2. Rietveld refinement of Ca_2Pd_3Ga.

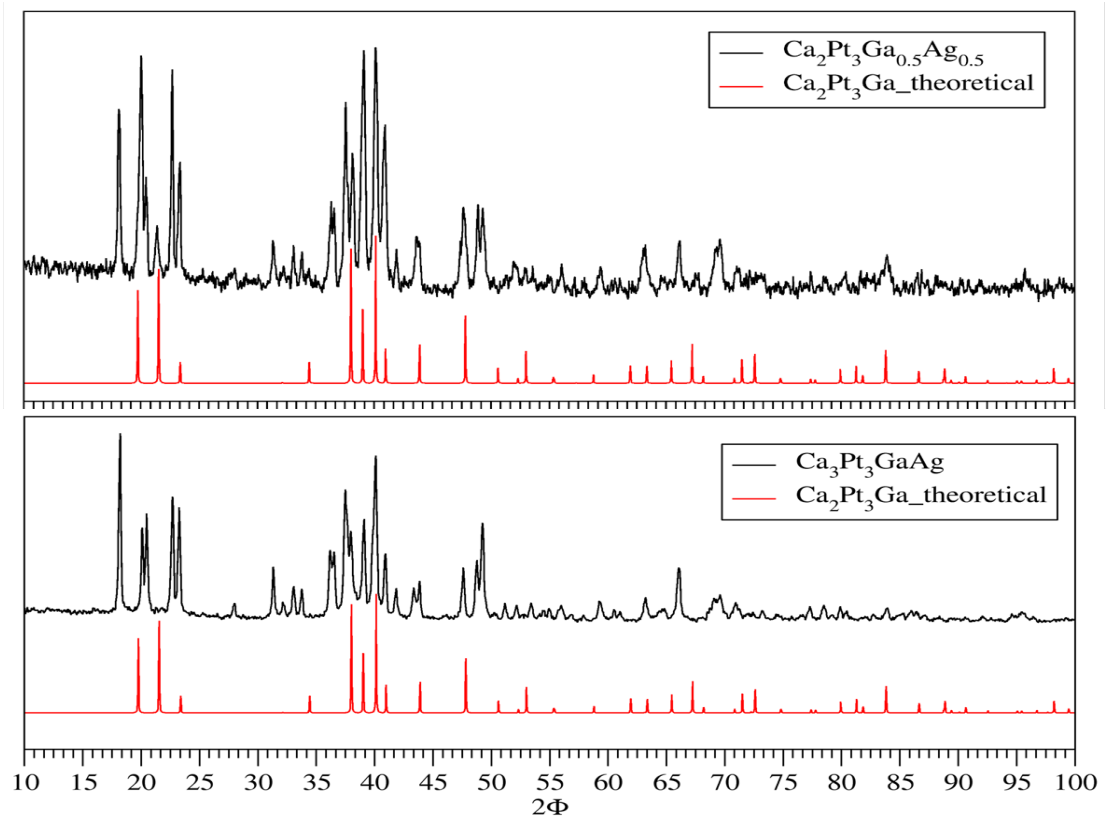

Figure S3. Powder patterns with loadings of $Ca_2Pt_3Ga_{0.5}Ag_{0.5}$ (upper) and Ca_3Pt_3GaAg (lower).

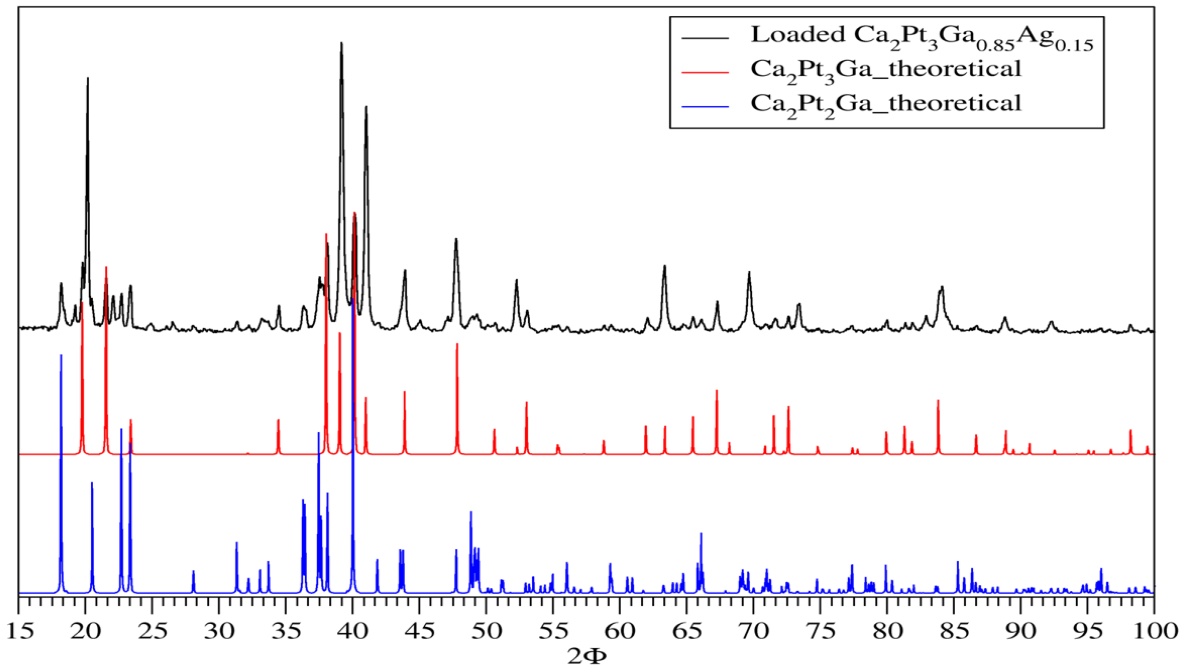

Figure S4. Powder pattern of another loaded sample of $Ca_2Pt_3Ga_{0.85}Ag_{0.15}$.

Table S1. Atomic coordinates and anisotropic displacement parameters ($Å^2$x10) for Ca_2Pd_3Ga.

	x	y	z	U^{11}	U^{22}	U^{33}
Ca	0	0	0.3722(1)	0.012(1)	0.012(1)	0.012(1)
Pd	½	0	½	0.010(1)	0.007(1)	0.010(1)
Ga	0	0	0	0.009(1)	0.009(1)	0.008(1)

Table S2. Atomic coordinates and anisotropic displacement parameters ($Å^2$x10) for Ca_2Pt_3Ga.

	x	y	z	U^{11}	U^{22}	U^{33}
Ca	0	0	0.3750(2)	0.007(1)	0.007(1)	0.008(1)
Pt	½	0	½	0.008(1)	0.006(1)	0.006(1)
Ga	0	0	0	0.007(1)	0.007(1)	0.005(1)

Table S3. X-ray diffraction data on additions crystals for Ca_2Pt_3Ga and Ca_2Pd_3Ga.

Sample	Ca_2Pt_3Ga	Ca_2Pt_3Ga	Ca_2Pd_3Ga	Ca_2Pd_3Ga
Space Group	*R*-3*m*	*R*-3*m*	*R*-3*m*	*R*-3*m*
Unit Cell Dim.	*a* = 5.571(7) Å	*a* = 5.565(4) Å	*a* = 5.666(8) Å	*a* = 5.62(2) Å
	c = 12.38(2) Å	*c* = 12.367(8) Å	*c* = 12.39(2) Å	*c* = 12.27(4) Å
Volume	332.7(9) $Å^3$	331.7(1) $Å^3$	344.3(1) $Å^3$	336.(3) $Å^3$
Z	3	3	3	3
Theta range for data collection	4.534 to 28.837°	4.539 to 31.202°	4.495 to 28.878°	4.505 to 31.033°
Index ranges	–7<=*h*<=7,	–8<=*h*<=7,	–7<=*h*<=7,	–8<=*h*<=8,
	–7<=*k*<=7,	–7<=*k*<=7,	–7<=*k*<=7,	–8<=*k*<=8,
	–16<=*l*<=16	–17<=*l*<=17	–17<=*l*<=17	–17<=*l*<=17
Reflections Collected	1548	1305	2654	1741
Independent Reflections	125[R(int)=0.0348]	153[R(int)=0.0322]	147[R(int)=0.0224]	154[R(int)=0.0585]
Data/restraints/parameters	125 / 0 / 11	153 / 0 / 11	147 / 0 / 1	154 / 0 / 11
Goodness-of-fit	1.204	1.179	1.282	1.236
Final R indices	R1 = 0.0138,	R1 = 0.0196,	R1 = 0.0171,	R1 = 0.0157,
[I>2sigma(l)]	wR2 = 0.0318	wR2 = 0.0463	wR2 = 0.0416	wR2 = 0.0320
R indices (all data)	R1 = 0.0138,	R1 = 0.0200,	R1 = 0.0173,	R1 = 0.0174,
	wR2 = 0.0318	wR2 = 0.0466	wR2 = 0.0417	wR2 = 0.0331
Extinction Coefficient	0.0037(2)	n/a	n/a	0.0030(3)
Largest diff. peak and hole	1.617 and	1.942 and	1.582 and	2.348 and
	–1.288 e·$Å^{-3}$	–4.014 e·$Å^{-3}$	–3.261 e·$Å^{-3}$	–1.470 e·$Å^{-3}$

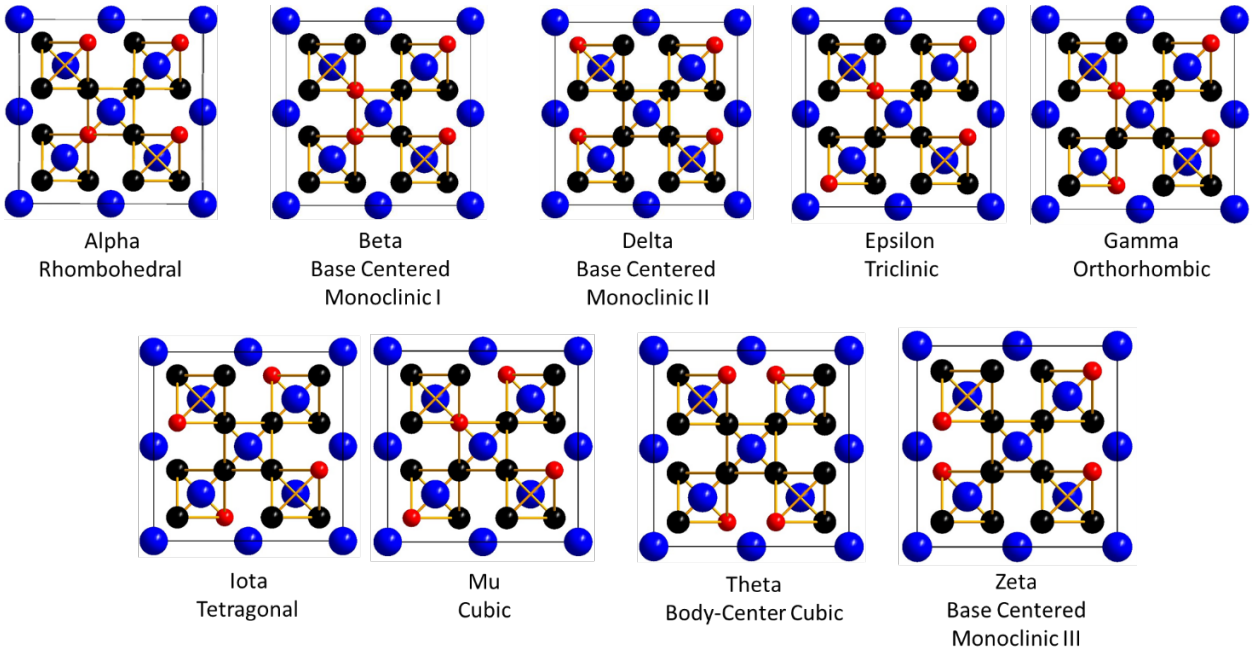

Figure S5. Coloring Models and respective symmetries.

Table S4. Total energies and nearest Ge-Ge contact for theoretical models of Ca_2Pd_3Ge.

	Ca_2Pd_3Ge		
Model	**Ge-Ge distance (Å)**	**meV non-optimized**	**meV optimized**
Alpha	5.280	0	+0.0
Beta	2.810	+29.8	+66.6
Delta	2.846	+55.1	+110.1
Epsilon	2.881	+36.7	+74.1
Gamma	4.785	+84.2	+31.7
Iota	3.137	+66.9	+102.0
Mu	4.723	+21.6	+43.9
Theta	3.091	+180.9	+217.4
Zeta	2.937	+88.8	+137.1

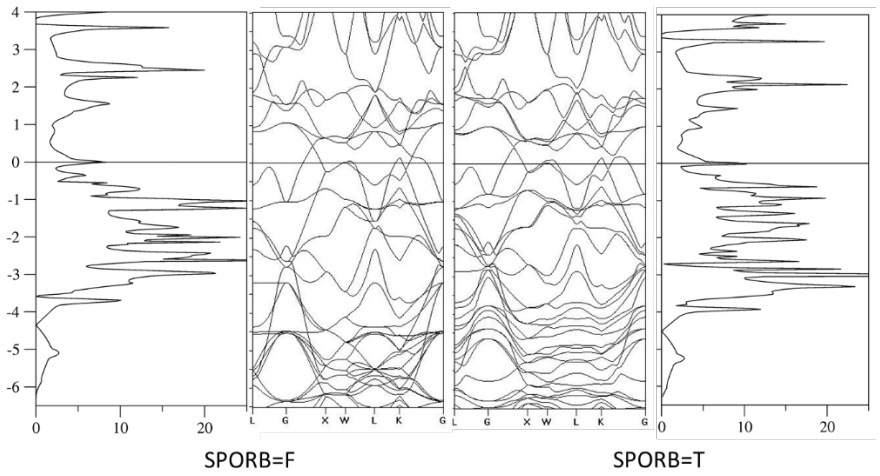

Figure S6. DOS and Band structures for $CaPt_2$ without (left) and with (right) spin-orbit coupling. Degeneracies in the band structure at Gamma are lifted at -4.5, -3, -2.5, and -1 eV along with degeneracies at L at -5.5 and 4.5 eV by spin-orbit coupling

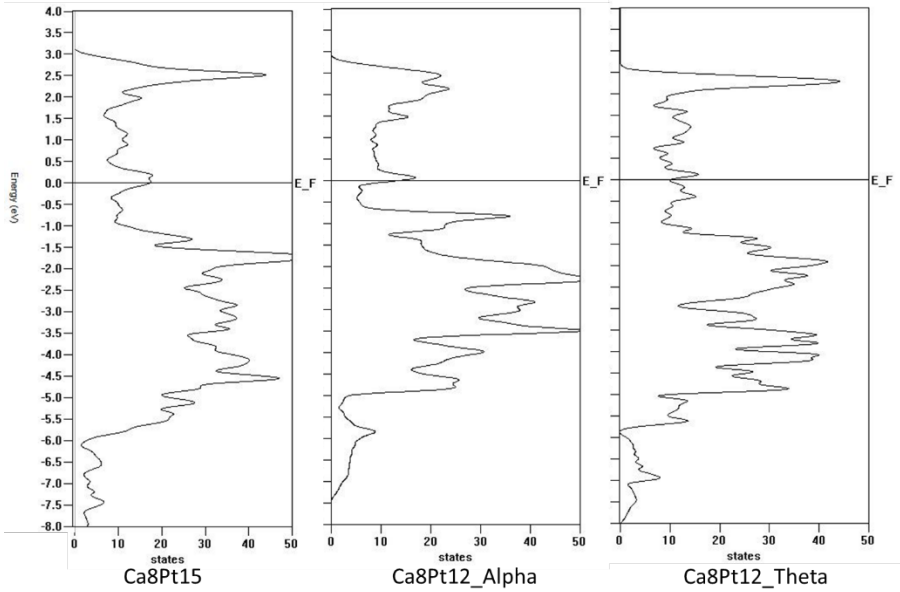

Figure S7. VASP calculated DOS for Ca_8Pt_{15} and two models of Ca_8Pt_{12}. Alpha has the vacancies as far apart in the structure as possible while theta has the vacancies as close together which removes one of the tetrahedra from the structure.

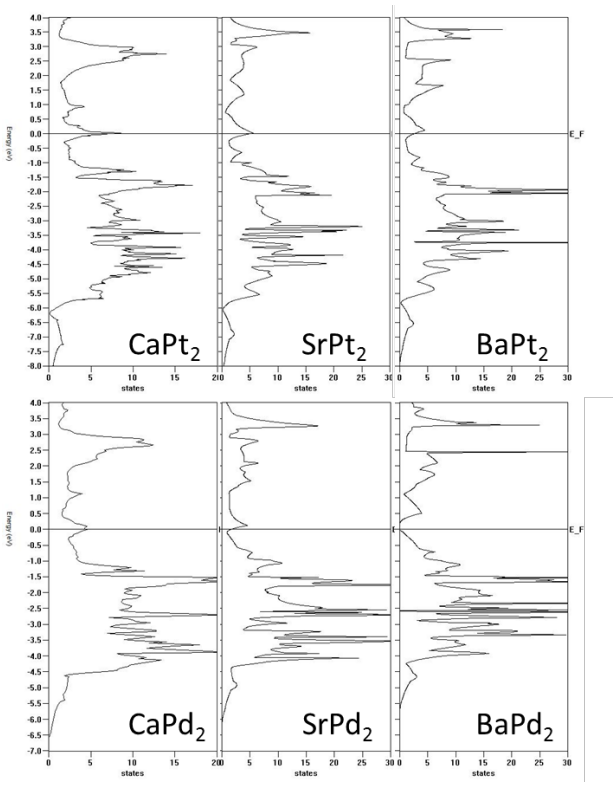

Figure S8. DOS calculated for AEM_2 (AE=Ca, Sr, Ba M=Pt, Pd). As the alkaline-earth metal gets larger and heavier the DOS starts to shift away from the Fermi level.

Table S5. Optimized Alpha structure with lattice constants and interatomic distances.

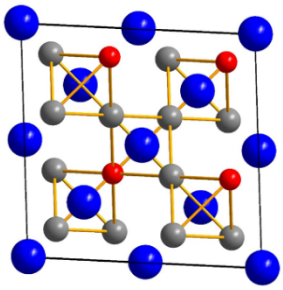

Bond	Distance		#/unit cell		Unit Cell Parameters	
	Ca_2Pd_3Ga	Ca_2Pt_3Ga			Ca_2Pd_3Ga	Ca_2Pt_3Ga
M-M	2.837	2.810	24	a (Å)	7.7511	7.7077
M-Ga	2.641	2.638	24	b (Å)	7.7511	7.7077
Ga-Ga	n/a	n/a	0	c (Å)	7.7511	7.7077
Ca-Ca	3.175 3.415	3.119 3.407	4 12	α (°)	94.0958	93.6062
Ca-Ga	3.311	3.286	24	β (°)	85.9042	86.3938
Ca-M	3.035 3.251	3.066 3.213	24 48	γ (°)	85.9042	86.3938

Table S6. Optimized Beta structure with lattice constants and interatomic distances.

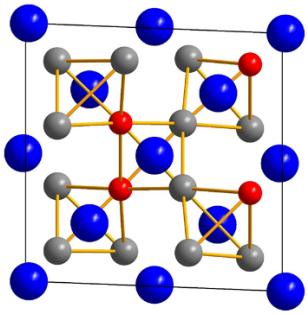

Bond	Distance		#/unit cell	Unit Cell Parameters		
	Ca_2Pd_3Ga	Ca_2Pt_3Ga			Ca_2Pd_3Ga	Ca_2Pt_3Ga
M-M	2.757-2.905	2.736-2.876	25	a (Å)	7.7657	7.7411
M-Ga	2.572-2.717	2.569-2.695	22	b (Å)	7.7657	7.7411
Ga-Ga	2.731	2.755	1	c (Å)	7.7031	7.6391
Ca-Ca	3.140-3.542	3.091-3.419	16	α (°)	92.1501	91.956
Ca-Ga	3.173-3.368	3.160-3.357	24	β (°)	87.8499	88.044
Ca-M	2.983-3.340	3.020-3.319	72	γ (°)	86.5066	87.097

Table S7. Optimized Delta structure with lattice constants and interatomic distances.

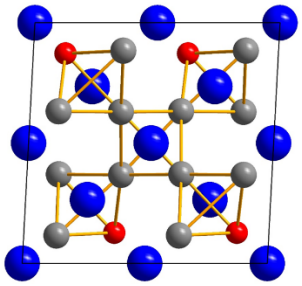

Bond	Distance		#/unit cell	Unit Cell Parameters		
	Ca_2Pd_3Ga	Ca_2Pt_3Ga			Ca_2Pd_3Ga	Ca_2Pt_3Ga
M-M	2.728-2.866	2.710-2.852	26	a (Å)	7.8794	7.8819
M-Ga	2.582-2.787	2.579-2.777	20	b (Å)	7.6739	7.6101
Ga-Ga	2.775	2.811	2	c (Å)	7.6959	7.6526
Ca-Ca	3.285-3.545	3.262-3.285	16	α (°)	90	90
Ca-Ga	3.223-3.375	3.205-3.397	24	β (°)	86.9465	87.5532
Ca-M	3.079-3.336	3.086-3.337	72	γ (°)	90	90

Table S8. Optimized Epsilon structure with lattice constants and interatomic distances.

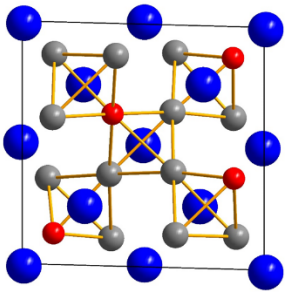

Bond	Distance		#/unit cell	Unit Cell Parameters		
	Ca_2Pd_3Ga	Ca_2Pt_3Ga			Ca_2Pd_3Ga	Ca_2Pt_3Ga
M-M	2.761-2.910	2.734-2.869	25	a (Å)	7.6727	7.6312
M-Ga	2.578-2.722	2.589-2.705	22	b (Å)	7.7939	7.7799
Ga-Ga	2.800	2.808	1	c (Å)	7.7508	7.6972
Ca-Ca	3.161-3.584	3.134-3.431	16	α (°)	91.5298	91.3602
Ca-Ga	3.209-3.369	3.194-3.361	24	β (°)	89.9967	89.8574
Ca-M	3.054-3.340	3.050-3.313	72	γ (°)	87.9109	88.3982

Table S9. Optimized Gamma structure with lattice constants and interatomic distances.

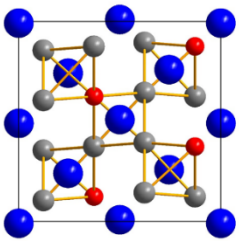

Bond	Distance		#/unit cell		Unit Cell Parameters	
	Ca_2Pd_3Ga	Ca_2Pt_3Ga			Ca_2Pd_3Ga	Ca_2Pt_3Ga
M-M	2.823-2.840	2.802-2.816	24	a (Å)	7.7343	7.7243
M-Ga	2.639-2.643	2.625-2.658	24	b (Å)	7.7343	7.7243
Ga-Ga	n/a	n/a	0	c (Å)	7.7343	7.6371
Ca-Ca	3.150-3.455	3.119-3.427	16	α (°)	90	89.9998
Ca-Ga	3.205-3.314	3.196-3.287	24	β (°)	90	90.0002
Ca-M	3.046-3.264	3.069-3.238	72	γ (°)	86.1127	86.9369

Table S10 Optimized Iota structure with lattice constants and interatomic distances.

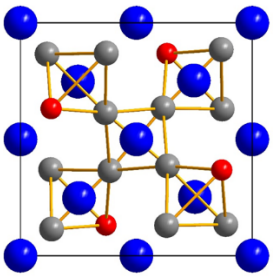

Bond	Distance		#/unit cell		Unit Cell Parameters	
	Ca_2Pd_3Ga	Ca_2Pt_3Ga			Ca_2Pd_3Ga	Ca_2Pt_3Ga
M-M	2.765-2.884	2.750-2.883	26	a (Å)	7.5721	7.5281
M-Ga	2.596-2.650	2.604-2.630	20	b (Å)	7.8370	7.8003
Ga-Ga	2.922	2.931	2	c (Å)	7.8370	7.8003
Ca-Ca	3.186-3.431	3.156-3.408	16	α (°)	90	90
Ca-Ga	3.211-3.330	3.185-3.337	24	β (°)	90	90
Ca-M	3.054-3.365	3.028-3.341	72	γ (°)	90	90

Table S11. Optimized Mu structure with lattice constants and interatomic distances.

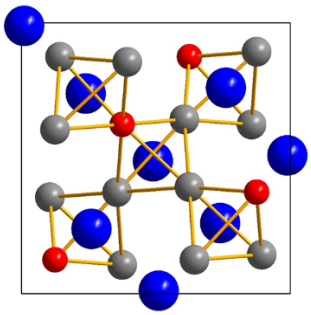

Bond	Distance		#/unit cell		Unit Cell Parameters	
	Ca_2Pd_3Ga	Ca_2Pt_3Ga			Ca_2Pd_3Ga	Ca_2Pt_3Ga
M-M	2.793	2.8154	24	a (Å)	7.7740	7.6900
M-Ga	2.591	2.632	24	b (Å)	7.7740	7.6900
Ga-Ga	n/a	n/a	0	c (Å)	7.7740	7.6900
Ca-Ca	3.199-3.572	3.246-3.590	16	α (°)	90	90
Ca-Ga	3.226	3.258	24	β (°)	90	90
Ca-M	3.059-3.202	3.106-3.234	72	γ (°)	90	90

Table S12. Optimized Theta structure with lattice constants and interatomic distances.

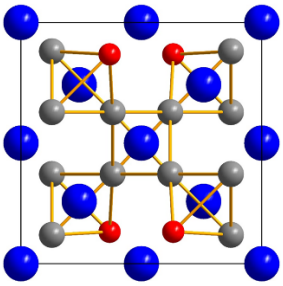

Bond	Distance		#/unit cell	Unit Cell Parameters		
	Ca_2Pd_3Ga	Ca_2Pt_3Ga			Ca_2Pd_3Ga	Ca_2Pt_3Ga
M-M	2.727-2.832	2.707-2.809	30	a (Å)	7.5980	7.7532
M-Ga	2.633	2.606	12	b (Å)	7.5980	7.7532
Ga-Ga	2.909	2.950	6	c (Å)	7.5980	7.7532
Ca-Ca	3.254-3.405	3.224-3.404	16	α (°)	90	90
Ca-Ga	3.207-3.338	3.195-3.353	24	β (°)	90	90
Ca-M	3.190-3.277	3.179-3.274	72	γ (°)	90	90

Table S13. Optimized Zeta structure with lattice constants and interatomic distances.

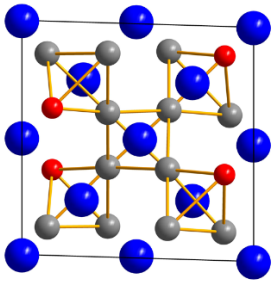

Bond	Distance		#/unit cell	Unit Cell Parameters		
	Ca_2Pd_3Ga	Ca_2Pt_3Ga			Ca_2Pd_3Ga	Ca_2Pt_3Ga
M-M	2.722-2.931	2.706-2.929	27	a (Å)	7.7868	7.7557
M-Ga	2.588-2.786	2.583-2.782	18	b (Å)	7.7868	7.7557
Ga-Ga	2.798-2.913	2.824-2.922	3	c (Å)	7.6855	7.6535
Ca-Ca	3.211-3.537	3.180-3.538	16	α (°)	91.7224	91.3708
Ca-Ga	3.177-3.353	3.182-3.369	24	β (°)	88.2776	88.6292
Ca-M	3.052-3.311	3.075-3.281	72	γ (°)	89.5669	89.6874

Table S14. COHP interactions in $CaPt_2$

Bond	Distance	#/formula unit	ICOHP Ry	ICOHP eV	Total	%
Ca-Ca	3.29	2	-0.01003	-0.13646	-0.27292	1.468672
Ca-Pt	3.15	12	-0.0405	-0.551	-6.61203	35.58198
Pt-Pt	2.686	6	-0.1433	-1.9496	-11.6976	62.94935

Table S15. COHP interactions in $CaPd_2$

Bond	Distance	#/formula unit	ICOHP Ry	ICOHP eV	Total	%
Ca-Ca	3.313	2	-0.01089	-0.14816	-0.29632	2.121318
Ca-Pd	3.172	12	-0.03377	-0.45944	-5.51329	39.46938
Pd-Pd	2.705	6	-0.09995	-1.35982	-8.15892	58.4093

Table S16. COHP interactions in Ca_2Pt_3Ga

Bond	Distance	#/formula unit	ICOHP Ry	ICOHP eV	ICOHP/f.u.	%	% by Type
Ca-Ca	3.092	1	-0.01265	-0.1721	-0.1721	0.504105	1.82
	3.374	3	-0.01103	-0.15006	-0.45019	1.318642	
Ca-Ga	3.254	6	-0.0243	-0.3306	-1.98361	5.810154	5.81
Ca-Pt	3.036	6	-0.04967	-0.67576	-4.05456	11.87615	30.68
	3.183	12	-0.03933	-0.53508	-6.42102	18.80768	
Pt-Ga	2.613	6	-0.1327	-1.80538	-10.8323	31.7287	31.73
Pt-Pt	2.782	6	-0.12528	-1.70443	-10.2266	29.95457	29.95

Table S17. COHP interactions in Ca_2Pd_3Ga

Bond	Distance	#/formula unit	ICOHP Ry	ICOHP eV	ICOHP/f.u.	%	% by Type
Ca-Ca	3.145	1	-0.01444	-0.19646	-0.196456	0.68512	2.42
	3.389	3	-0.01216	-0.16544	-0.496310	1.730829	
Ca-Ga	3.287	6	-0.02772	-0.37713	-2.262783	7.891216	7.89
Ca-Pd	3.005	6	-0.04405	-0.5993	-3.595801	12.53997	31.56
	3.225	12	-0.03341	-0.45454	-5.454516	19.02204	
Pd-Pd	2.816	6	-0.08572	-1.16622	-6.997323	24.40242	24.40
Pd-Ga	2.617	6	-0.11848	-1.61192	-9.671522	33.7284	33.73

Table S18. Specific total energies (eV/formula unit) for each component used to calculate ΔEs presented in **Table 4.**

$CaPt_2$	–16.8947 eV
Pt	–6.0954 eV
Ca_2Pt_3Ga*	–30.4912 eV
Ca_2Pt_3Ga**	–30.5797 eV
Ca_2Pt_3Ga	–30.9045 eV
$CaPd_2$	–14.4409 eV
Ca_2Pd_3Ga*	–26.8363 eV
Ca_2Pd_3Ga**	–26.8787 eV
Ca_2Pd_3Ga	–27.1779 eV
Pd	–5.2156 eV
Ga	–2.9122 eV

APPENDIX B. SUPPORTNG INFORMATION FOR CHAPTER 4

An orthorhombic variant of Ca_2Pd_2Ga

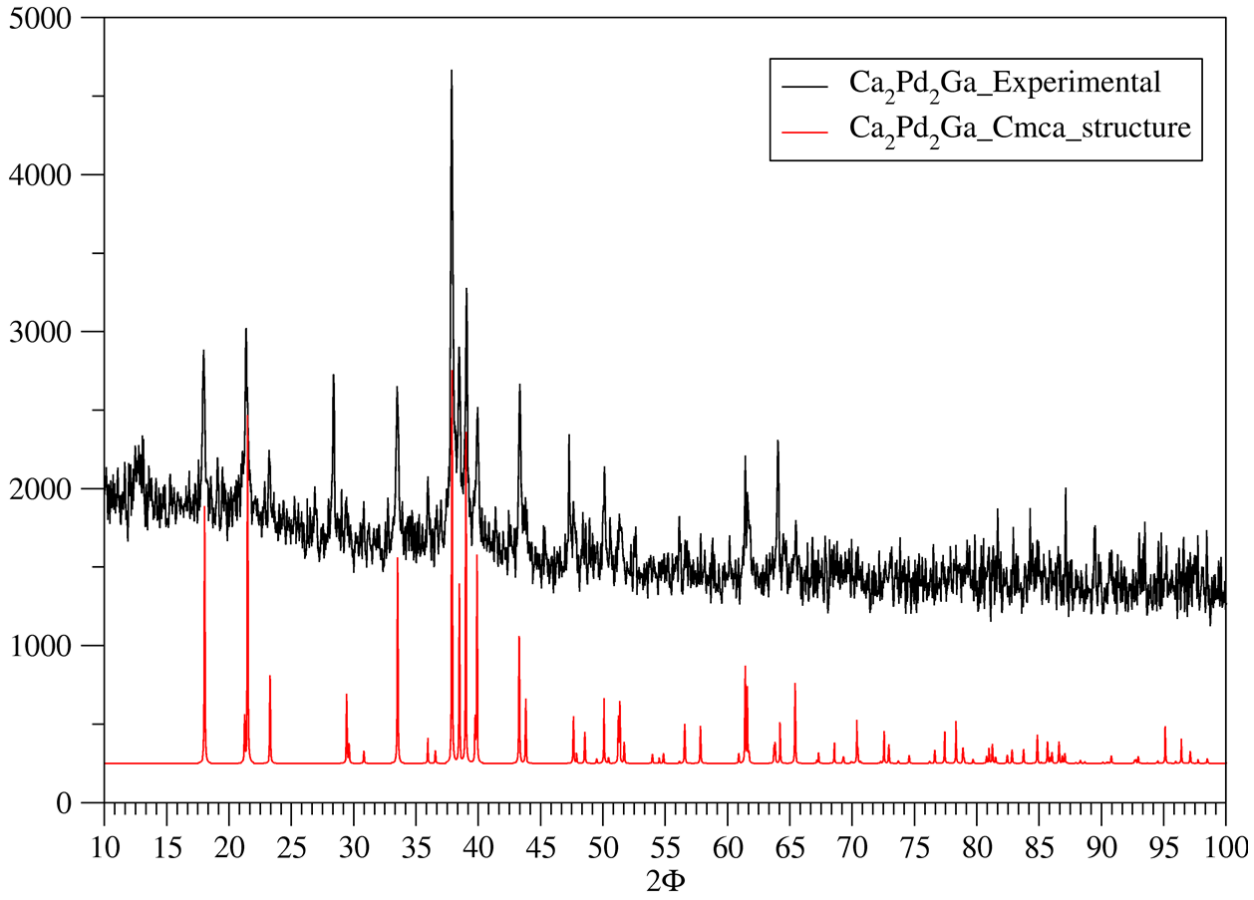

Figure S1. Powder X-Ray pattern of a second synthesized sample of orthorhombic Ca_2Pd_2Ga. The non-indexed peaks are not as prevalent in this pattern however, the relative intensities do not match exactly, again showing that the Cmca Ca_2Pd_2Ga is a major phase but not pure.

Table S1. X-ray diffraction data on additional crystals for Ca_2Pd_2Ga.

Sample	Ca_2Pd_2Ga	Ca_2Pd_2Ga	Ca_2Pd_2Ga
Space Group	Cmca	Cmca	Cmca
Unit Cell	a=5.803(4) b=9.834(6) c=7.638(5)	a=5.794(3) b=9.824(5) c=7.638(4)	a=5.7984(9) b=9.829(2) c=7.637(1)
Volume		434.7(4)	435.3(1)
Z	4	4	4
Absorption Coefficient		16.470 mm^{-1}	8.225 mm^{-1}
Index Ranges	-8<=h<=8, -14<=k<=13, -10<=l<=10	-8<=h<=8, -14<=k<=13, -11<=l<=10	-7<=h<=7, -13<=k<=13, -9<=l<=10
Reflection Collected	3039	2291	3455
Independent Reflections	365 [R(int) = 0.0199]	368 [R(int) = 0.0173]	305 [R(int) = 0.0180]
Theta range for data collection	4.144 to 31.165°	4.149 to 31.113□	4.146 to 28.883°
Refinement method	Full-matrix least-squares on F^2	Full-matrix least-squares on F^2	Full-matrix least-squares on F^2
Data/restraints/parameters	365 / 0 / 16	368 / 0 / 16	305 / 0 / 16
Goodness-of-fit on F^2	1.349	1.188	1.294
Final R indices [I>2sigma(I)]	R1 = 0.0207 wR2 = 0.0473	R1 = 0.0180 wR2 = 0.0408	R1 = 0.0164 wR2 = 0.0385
R indices (all data)	R1 = 0.0217 wR2 = 0.0478	R1 = 0.0200 wR2 = 0.0426	R1 = 0.0173 wR2 = 0.0391
Largest diff. peak and hole	0.436 and -0.960 e.$Å^{-3}$	0.691 and -0.982 e.$Å^{-3}$	0.409 and -0.699 e.$Å^{-3}$

Table S2. Atomic coordinates and anisotropic displacement parameters ($Å^2$x10) for Ca_2Pd_2Ga.

Atom	x	y	z	U^{11}	U^{22}	U^{33}
Pd	¼	0.0822(1)	¼	0.009(1)	0.012(1)	0.012(1)
Ga	0	0	0	0.010(1)	0.018(1)	0.010(1)
Ca	0	0.3354(1)	0.0958(1)	0.012(1)	0.011(1)	0.013(1)

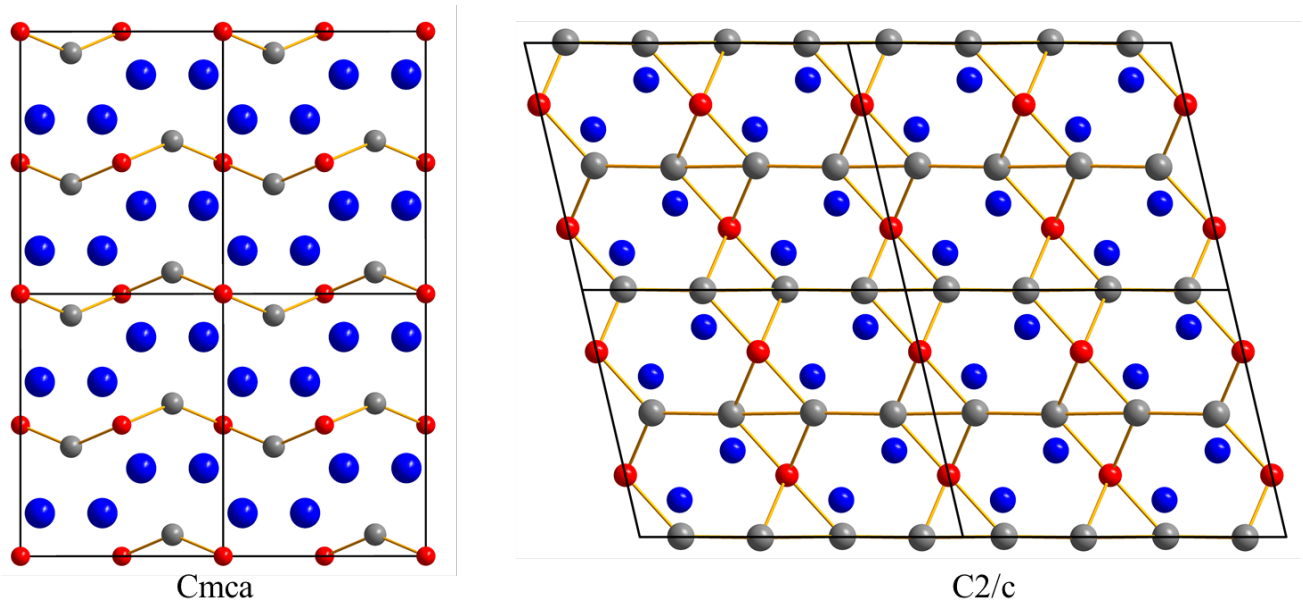

Figure S2. Cross section of 4x4 unit cells of Cmca (left) and C2/c (right) structures looking down the a direction. Distinct "layering" can be observed in the Cmca structure. Blue, grey, and red atoms are Ca, Pd, and Ga respectively.

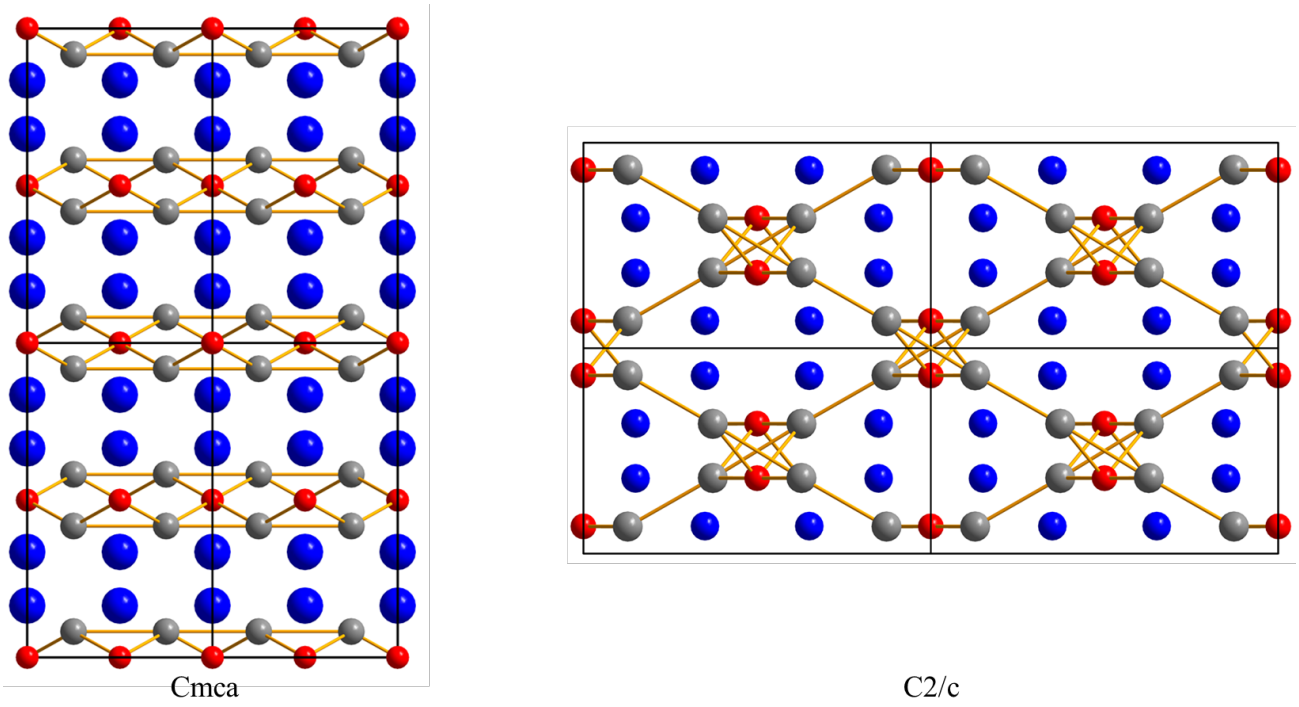

Figure S3. Cross section of 4x4 unit cells of Cmca (left) and C2/c (right) structures looking down the c direction. Layering can be seen in the Cmca structure whereas linear chains surrounded by Ca can be seen in the C2/c structure. Blue, grey, and red atoms are Ca, Pd, and Ga respectively.

APPENDIX C. SUPPORTING INFORMATION FOR CHAPTER 5

$Gd(Co_{1-x}Ga_x)_2$: Synthesis, Crystal Structures, and Investigation of Structural Transformations and Magnetic Properties

Table S1. Comparison of experimental and optimized lattice parameters and bond lengths of $GdCo_2$.

Sample	*a* (Å)	Co-Co Bond Length (Å)	Gd-Co Bond Length (Å)
$GdCo_2$_single crystal	7.2518(8)	2.5639(3)	3.0064(3)
LDA Optimized	6.9781	2.4671	2.8930
LSDA Optimized	7.2167	2.5515	2.9919

Table S2. Experimental and optimized results for GdCoGa, DyCoGa, and CaPtGa.

		GdCoGa (Powder)	GdCoGa (Single crystal)	GdCoGa Sichevich et al	DyCoGa	CaPtGa
Exp	*a*	7.1522	7.1139	7.1506	7.052	7.184
	b	4.4339	4.4017	4.4312	4.393	4.429
	c	7.0003	7.0252	7.0030	6.958	7.595
	a/b	1.613	1.616	1.614	1.605	1.622
	a/c	1.022	1.013	1.021	1.014	0.946
	eV/Gd	–25.2205	–25.3951	–25.4399	–17.8170	–13.6993
Opt	*a*	7.1737 (+0.023)	7.1708 (+0.057)	7.1711 (+0.0205)	7.069 (+0.017)	7.143 (–0.041)
	b	4.4725 (+0.039)	4.4806 (+0.079)	4.4737 (+0.0425)	4.396 (+0.003)	4.430 (+0.001)
	c	6.8086 (–0.191)	6.7720 (–0.2532)	6.8053 (–0.1977)	6.702 (–0.256)	7.685 (+0.090)
	a/b	1.604 (–0.009)	1.600 (–0.016)	1.603 (–0.011)	1.608 (+0.003)	1.612 (–0.010)
	a/c	1.048 (+0.026)	1.059 (+0.046)	1.054 (+0.033)	1.055 (+0.041)	0.929 (–0.017)
	eV/Gd	–25.2423	–25.4754	–25.2422	–17.8605	–13.7067

Table S3. Comparison of experimental and optimized lattice parameters of $GdGa_2$.

Sample	*a* (Å)	*b* (Å)
$GdGa_2$_powder refined	4.22011(6)	4.13423(9)
LSDA optimized	4.2477	4.1420

Figures S1-3 are the DOS and COHP curves calculated using LOBSTER and the output files from VASP. The DOS curves of the two methods are similar between except for the presence of the Gd 4*f* orbitals that occur as a very narrow band ~8 eV below E_F and a dominating wider band starting around 3 eV above E_F. These 4*f* orbitals, other than the spike at ~ −8 eV, contribute less than 1% to the overall occupied DOS. The pseudopotential for Gd uses a Xe core. Evaluation of COHP curves for all three compounds reveals some unanticipated and counterintuitive impacts from the explicit inclusion of 4*f* orbitals of Gd. Tables S4-6 show the ICOHP values calculated using TB-LMTO-ASA and LOBSTER. The numerical results yield significantly different outcomes for the differing methods. To the best of our knowledge, COHP analyses of rare-earth intermetallics using VASP/LOBSTER have been limited to La- and Y-containing compounds; one such analysis of Tb-doped $BiFeO_3$ did include Tb [Iyyappa, R.P.; Mahalakshmi, S.; Sharat, C. The structural, electronic, magnetic and optical properties of the new promising spintronic material $Bi_{0.92}Tb_{0.08}FeO_3$: A first-principles approach. *Computational Materials Science*, **2018**, *145*, 244-251]. Nevertheless, for completeness, the results from VASP/LOBSTER calculations for $GdCo_2$, GdCoGa, and $GdGa_2$ are presented in this section.

Tables S7-8 show the ICOHP values calculated with TB-LMTO-ASA for the experimental and VASP optimized structures. The difference of the values for the optimized and experimental structures for each compound is shown to be minimal. Thus, for various reasons discussed herein, the TB-LMTO-ASA approach was employed to calculate the DOS and COHP curves for the optimized structures of $GdCo_2$, GdCoGa, and $GdGa_2$.

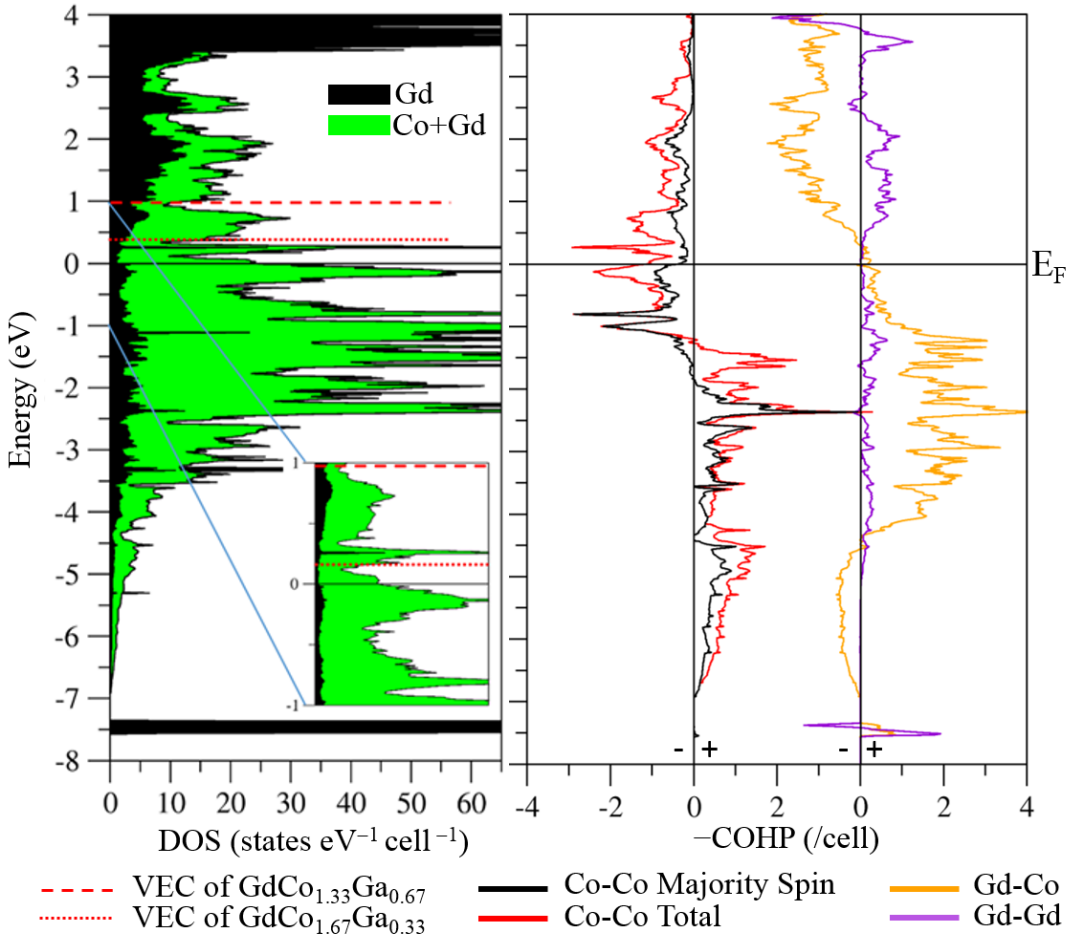

Figure S1. LOBSTER calculated DOS (left) and −COHP (right). The DOS is similar to that calculated by TB-LMTO-ASA except for the pseudogap opening at ~1 eV above E_F. The Co–Co interactions cross from bonding to antibonding at a lower energy relative to E_F compared to the results of TB-LMTO-ASA. The intensity of the Gd–Gd interactions, as indicated by the percentage of the total ICOHP value, is increased in the VASP/LOBSTER result than in TB-LMTO-ASA.

Table S4. Comparison of LOBSTER and TB-LMTO-ASA %ICOHP for $GdCo_2$.

Bonds in $GdCo_2$	% ICOHP LOBSTER	% ICOHP TB-LMTO-ASA
Co-Co	22.08	49.39
Gd-Co	59.71	45.78
Gd-Gd	18.21	4.83

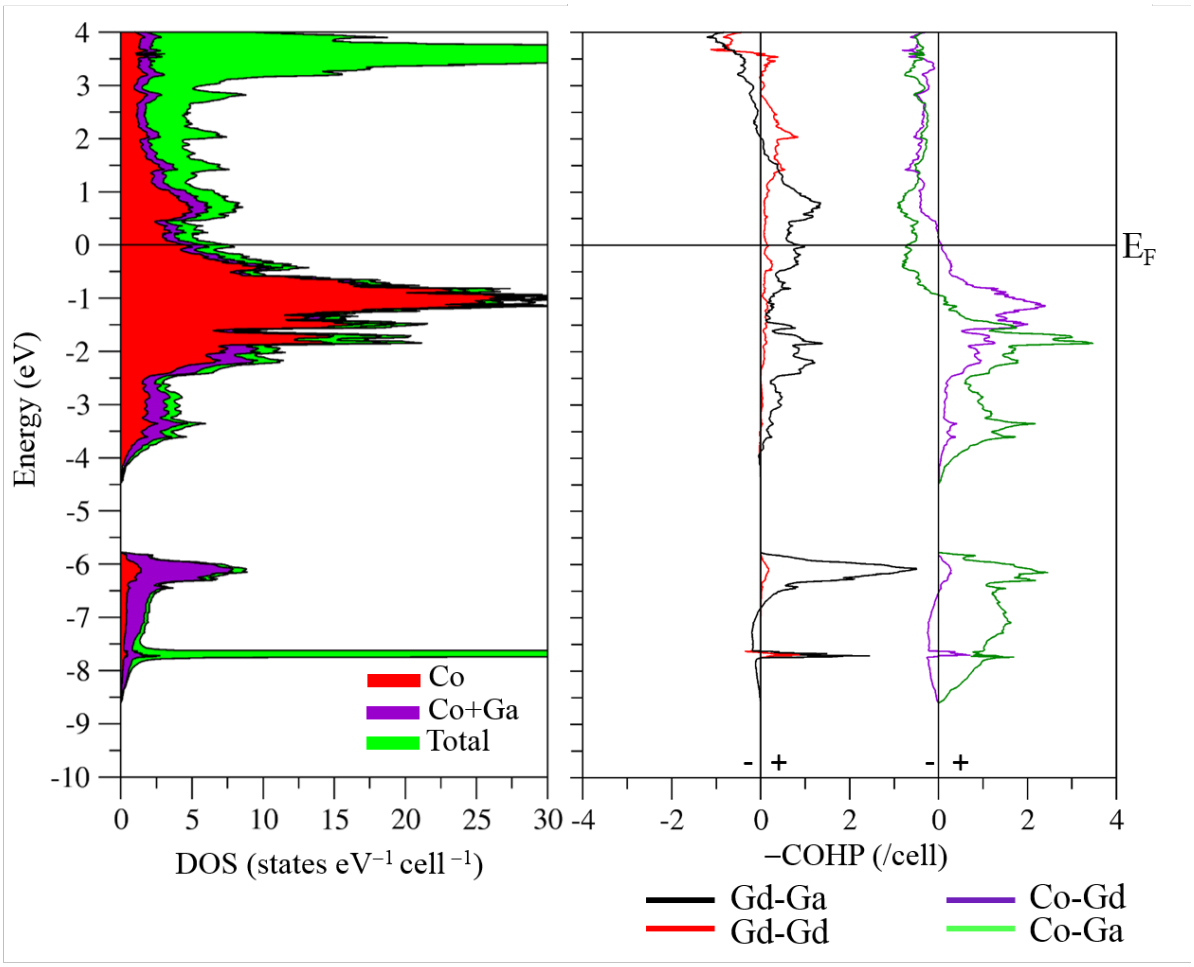

Figure S2. LOBSTER calculated DOS (left) and –COHP (right) for GdCoGa. LOBSTER calculates all interactions to be nonbonding at E_F except for the antibonding Co–Ga and the bonding Gd–Ga interaction.

Table S5. Comparison of LOBSTER and TB-LMTO-ASA %ICOHP for GdCoGa.

Bonds in GdCoGa	% ICOHP LOBSTER	% ICOHP TB-LMTO-ASA
Gd-Gd	7.97	4.26
Gd-Co	18.47	25.47
Gd-Ga	38.65	25.00
Co-Ga	34.00	43.11
Co-Co	0.91	2.16

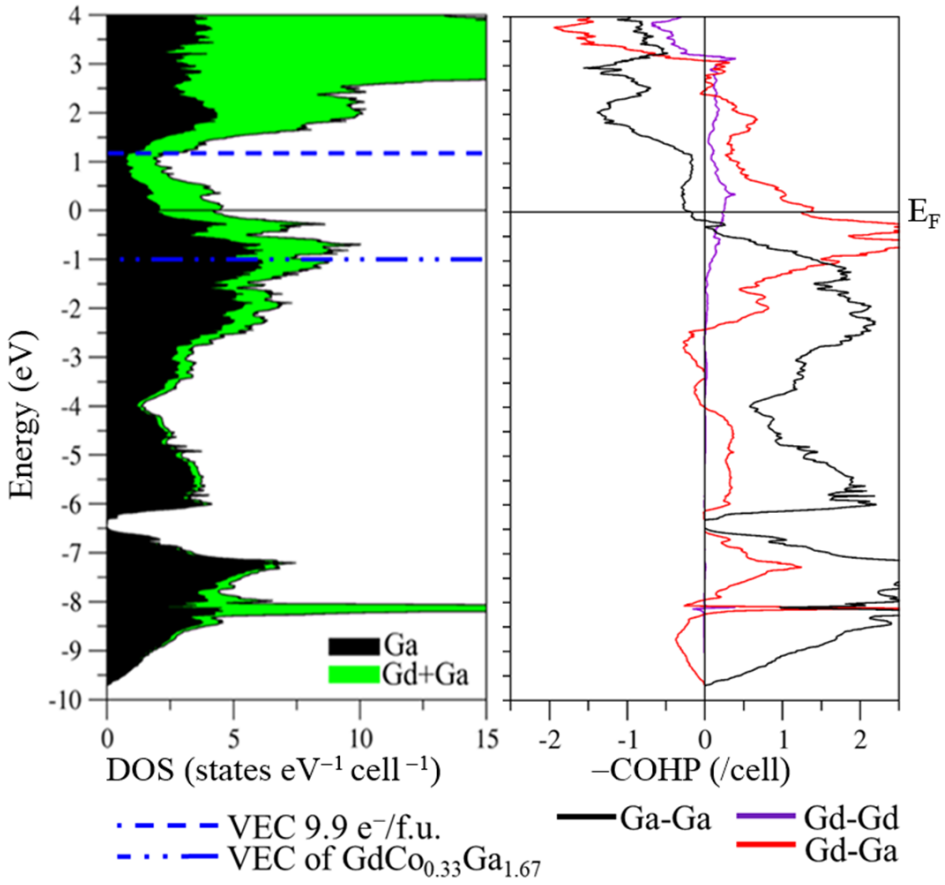

Figure S3. LOBSTER calculated DOS (left) and –COHP (right) for $GdGa_2$. The Gd–Ga interactions as calculated by LOBSTER cross from bonding to antibonding above E_F at ~ 2.5 eV. The Ga–Ga interactions are antibonding at E_F which differs from the TB-LMTO-ASA COHP as all interactions cross from bonding to antibonding at ~ 1Ev relative to E_F.

Table S6. Comparison of LOBSTER and TB-LMTO-ASA %ICOHP for $GdGa_2$.

Bonds in $GdGa_2$	% ICOHP LOBSTER	% ICOHP TB-LMTO-ASA
Ga-Ga	57.93	38.40
Gd-Ga	40.84	56.28
Gd-Gd	1.23	5.32

Table S7. Comparing %ICOHP for experimental and optimized structures of $GdCo_2$ calculated with TB-LMTO-ASA.

Bonds	% ICOHP Experimental Structure	% ICOHP VASP Optimized Structure	% Difference
Gd-Gd	4.81	4.83	+ 0.41
Gd-Co	46.42	45.78	– 1.39
Co-Co	48.77	49.39	+ 1.26

Table S8. Comparing %ICOHP for experimental and optimized structures of $GdGa_2$ calculated with TB-LMTO-ASA.

Bonds	% ICOHP Experimental Structure	% ICOHP VASP Optimized Structure	% Difference
Ga-Ga	38.43	38.40	– 0.08
Gd-Ga	56.22	56.28	+ 0.11
Gd-Gd	5.34	5.32	– 0.38